Study on the Structures and Magnetic Properties of Ground High-Spin 3d Homonuclear and 3d-4f Heteronuclear Complexes

Yumi Ida

The University of Electro-Communications

March 2016

Study on the Structures and Magnetic Properties of Ground High-Spin 3d Homonuclear and 3d-4f Heteronuclear Complexes Yumi Ida 2016

Study on the Structures and Magnetic Properties of Ground High-Spin 3d Homonuclear and 3d-4f Heteronuclear Complexes

A DISSERTATION SUBMITTED TO

THE GRADUATE SCHOOL OF INFORMATICS AND ENGINEERING

THE UNIVERSITY OF ELECTRO-COMMUNICATIONS

IN CANDIDACY FOR THE DEGREE OF DOCTOR OF PHILOSOPHY

OF SCIENCE

DEPARTMENT OF ENGINEERING SCIENCE

Yumi Ida

March 2016

Study on the Structures and Magnetic Properties of Ground High-Spin 3d Homonuclear and 3d-4f Heteronuclear Complexes

Approved by Supervisory Committee:

Chairperson: Prof. Takayuki Ishida

Member: Prof. Yoshio Kobayashi

Member: Assoc. Prof. Jin Nakamura

Member: Prof. Hiroyuki Nojiri (Tohoku University)

Member: Prof. Takashi Hirano

底高スピンとなる 3d ホモ金属および

3d-4f ヘテロ金属錯体の構造と磁性の研究

井田由美

概要

本論文は、単分子磁石材料に関する 2 つの化合物群、基底高スピンとなる 3d ホモ金属錯体および 3d-4f ヘテロ金属錯体の構造と磁性の研究を述べている。本論文は 4 章で構成されている。

第 1 章では、分子磁性体についての特徴を簡単に紹介した。中でも近年盛んに研究が行われている単分子磁石について、従来の永久磁石との比較を交えて説明した。続いて、現在の単分子磁石の研究情勢を簡単に概観して、この研究分野における本研究の位置付けと研究意義について述べた。また、本研究の磁気測定において物理的な背景・理論の焦点を絞り、重要な点をまとめた。

第 2 章では、3d ホモ金属錯体として 3 つのニッケル(II)イオンを用いた正三角形配置の三核錯体を取り上げ、その構造と磁性について詳述している。

題材とする物質群の特徴は、$Ni_3O_2X_3$ クラスターを中心に持つ錯陰イオン構造に 3 回軸対称を与えた点である。先行研究と比べると、磁化反転に関わるエネルギー障壁を高められ、磁性の解析を容易にし、合成手法が簡略化されたこと等が改善されている。三角形配置されたニッケルイオンのなす平面の周りをベルトのようにハロゲン化物イオンが二座架橋している。対象とする物質は 3 種あり、この中で構造上異なる点は、ニッケル三角平面に対して上下から三座架橋キャップするイオンの種類である。題材の 1 種は新規化合物である。

既知化合物の 2 種を含めて、これらのニッケル三角錯イオン系の磁性はまだ調査されていなかった。本磁気測定により、基底高スピン状態 $S = 3$ を有すること、すなわち、ニッケル(II)イオン ($3d^8$) の有する $S = 1$ が分子内で強磁性的にカップルしていることが分かった。また、$S = 3$ 化学種として磁気異方性定数 D が負となること、すなわち一軸異方性を有することがわかった。単分子磁石の開発においては、磁化反転の活性化エネルギーが $\Delta = |D|S^2$ で表されるため、この結果から、本物質群は単分子磁石の性能を有することが期待される。実際に、交流磁化率の測定において、磁化の反転に伴うダイナミクスが観測され、アレニウス挙動が認められた。

本物質群が当初の分子設計通りに潜在的な単分子磁石となっていることは示されたが、分子間のハロゲン接触により、この接触を介して弱い反強磁性的カップリングが生じているこ

とも明らかとなった。特に、低温で一次元的反強磁性的鎖が発達したり、反強磁性磁気転移を示すものが見出された。この分子間の相互作用が、低温領域では相対的に顕在化するので、単分子磁石としての振る舞いは隠されてしまう。基底状態でスピンを多くを失っているのでゼロ磁場近傍では自発磁化もヒステリシスも見られなかった。しかし、磁場を印加して現れるメタ磁性的挙動には磁気ヒステリシスが見出された。

以上のことから、本系は、潜在的な単分子磁石を反強磁性的分子間相互作用で連結した特異な材料群であることが分かった。一般的に、単分子磁石の研究では分子間相互作用のない状況が望まれるので、このように分子間の相互作用が導入された系を詳細に調べた研究例は珍しい。

第 3 章では、3d-4f ヘテロ金属錯体として、2 つの銅(II)と 1 つのジスプロシウム(III)イオンを含む三核錯体を取り上げた。類似のテルビウム(III)錯体は構造も磁気的性質も既知ではあったが、クラマースイオン性に着目して合成されたジスプロシウム錯体は新規化合物である。対象物質には、3d-4f イオンの間に酸素原子で二重架橋した構造が含まれる。この構造を共通とした 2 種の単量体的物質および 1 種のポリマー的物質の計 3 種の物質を対象として、構造と磁性を精密に調査した。

磁気測定から、これらの化合物は基底高スピン状態を示し、3d-4f ヘテロスピン系としては比較的強い強磁性的相互作用を示すことがわかった。交流磁化率測定から、ゼロ磁場において緩やかな磁気緩和が観測され、いずれも単分子磁石の性能を有することが分った。

高周波高磁場電子スピン共鳴（HF-EPR）による交換パラメータ J の精密測定は筆者の所属する研究グループの独自な手法である。したがって、3d-4f ヘテロスピン系でその交換相互作用の測定自体が新規性の高いものであり、さらに、特定の構造のシリーズを用いて交換相互作用を厳密に決定して比較する研究は、全く類例を見ず、非常に独創性の高いものである。本研究で用いた 3 種の対象化合物について、J/k_B = 2.25±0.05〜1.79±0.04 K と決定することができた。

構造磁性相関図を描くにあたり、類似の Dy–Cu 構造を持つ 2 つの既知化合物の結果を合わせて計 5 種の化合物について考察した。いくつかの構造パラメータと交換相互作用との相関を調べた結果、相関を見出したのは、Dy–O–Cu の結合角と Dy–O…O–Cu の「バタフライ角」を用いた場合であった。結合角は角度が小さくなるにつれて、強磁性的相互作用が大きくなり、バタフライ角については、角度が大きくなる（4 原子の平面性が高くなる）につれて交換相互作用が小さくなる傾向が見出された。

第 4 章では、全体のまとめと今後の展望について述べた。本研究成果により相互作用のメカニズムの理解が前進し、新規磁性材料の開発設計指針を提案することができると期待される。

Study on the Structures and Magnetic Properties of Ground High-Spin 3d Homonuclear and 3d-4f Heteronuclear Complexes

Yumi Ida

Abstract

This doctor thesis is written about the structural and magnetic study on the complexes related to single-molecule magnets (SMMs). SMMs have been attractive molecules due to their potential applications for information storage and quantum computing at the molecular level. Large magnetic moment and strong uniaxial magnetic anisotropy are required for SMMs. The author succeeded to prepare some novel compounds and precisely determined the magnetic parameters by means of magnetizations, magnetic susceptibilities, and electron paramagnetic resonance (EPR) techniques.

The author studied the structure and magnetic properties of a novel nickel(II) trinuclear complex as well as two known related compounds. They possess the ground high-spin state and a uniaxial magnetic anisotropy, which are favorable for SMMs. However, they also showed intermolecular antiferromagnetic couplings through the weak halogen···halogen contacts. One of these complexes was characterized as a pseudo one-dimensional antiferromagnetic chain, and another as a ground antiferromagnet. The magnetic hysteresis was observed at the metamagnetic-like magnetization jump and not at zero field. The author concluded that the compounds were potential SMMs with considerable intermolecular antiferromagnetic interaction.

For a heterospin 4f-3d system, the author et al. synthesized three new complexes involving one dysprosium(III) and two copper(II) ion as a magnetically interacting unit. The structural analysis of them clarified double oxygen bridges between the Dy and Cu ions. The magnetic study revealed the presence of Dy–Cu ferromagnetic interactions together with the SMM behavior.

From the high-frequency EPR study the author found that the copper signal was biased owing to the exchange interaction from the dysprosium ion. The exchange coupling parameters were precisely determined from these exchange biases. To investigate magneto-structure relation, two additional data were taken from the literature, and the author attempted to draw a few plots of the exchange parameter as a function of geometrical parameters. Meaningful correlations were found when the Dy–O–Cu angle and Dy–O⋯O–Cu dihedral angle were applied. Though it is only empirical, such a magneto-structure relation has been proposed in Dy–Cu systems for the first time.

In conclusion, the magnetic properties of the Ni_3 and $DyCu_2$ complexes were studied in detail in connection with the crystal structures. The present results would assist comprehension of SMMs and accelerate development of novel SMMs.

Contents

Figures

Schemes

Tables

1 Introduction

1.1 Preface

This thesis is written about a study on the structures and magnetic properties of ground high-spin 3d homonuclear and 3d-4f heteronuclear complexes.

The author explains "molecular magnets". Molecular magnets are magnetic materials consisting of molecular components, and utilize the electron spins delocalized in molecular orbitals and/or those on radicals.[1] In contrast to inorganic magnetic materials, molecular magnets have some advantages. First, diverse chemical design and modification are possible. Second, low-dimensional magnetic materials can be easily constructed because, in a molecular magnet, the strength of intermolecular interaction can be reduced. Such intermolecular interactions are regulated by the molecular shape and stacking of molecules in crystals. As the components of molecular magnetic materials, there are organic radicals, metal-ion coordination compounds (e.g. complexes), and their combinations. The interaction among these compounds determines spin configuration in each molecule.[1] The author used 3d homonuclear and 3d-4f hetronuclear complexes. It is because the spins in 3d and 4f ions are usually larger than that of an organic radical, and 4f ions have strong magnetic anisotropy.[2] These characters are important for development of single-molecule magnets (SMMs)[2e,3,4] and other related magnetic materials. SMMs are similar to the fine magnetic particles with single magnetic domain structures.[5] The problem of utilizing these particles as nano magnetic materials may reside in a control of a particle size and the size distribution of particles. Since the SMM is made up of homologous molecules, the above problem can be avoided.

A ground high-spin state in a discrete molecule needs the ferromagnetic intramolecular interaction. Molecules of a ground high-spin state are important ingredients for a development of new SMMs. The development of SMMs is a basis for next-generation functional magnetic

materials, because they will be potentially applied for information storage media at the level of a single molecule or a few.[3] The ground high-spin molecules have also attracted much attention for adiabatic demagnetization refrigerants.[6] In the next section, the author will explain the outline of SMMs.

1.2 Origin of SMMs and Bulk Magnets

Bulk magnets are well known as typical ferromagnets with Fe, Ni, and Co. Ions of the transition metals (3d) involving Fe, Ni, and Co have some unpaired electrons which results in localized magnetic moments at each magnetic element.

Discrete magnetic moments do not cause a bulk to be a ferromagnetic state. To show the properties of the ferromagnetic state requires that each magnetic moment is aligned parallel each other pointing at the same direction. The behavior is regarded as a large macroscopic magnetic moment. This function arraying two moments in parallel is called as ferromagnetic exchange interaction.

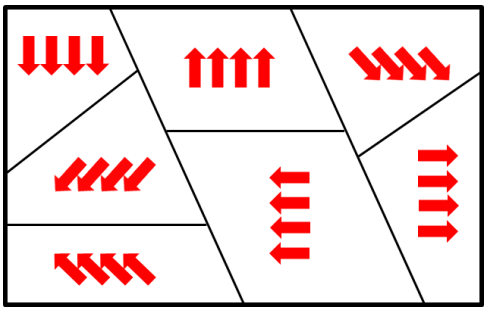

Figure 1.1. Schematic view of a magnetic domain. A red arrow denotes a magnetic moment. The partitioned region shows a magnetic domain.

A bulk ferromagnetic material contains a number of magnetic domains.[7] The magnetic domain is a region where the magnetic moment is arrayed in a uniform direction (Figure 1.1).

However, magnetic domains within the bulk magnetic material are rarely arranged in a uniform direction, because such a condition creates a higher magnetostatic energy and is unstable.[7c] In order to reduce the magnetostatic energy, each magnetic moment should take different magnetization directions in neighboring magnetic domains.

Magnetization curves with a hysteresis can be described in terms of a magnetic domain structure[7c] (Figure 1.2). In the initial zero magnetic field, the magnetic domain structure holds a low magnetostatic energy with zero magnetic moment (region I – II). By applying the magnetic field H_{ext}, magnetic domains with a near direction along the applied field grow while other domains diminish, which results in the major magnetic domain (region II – III). The uniformly magnetized region becomes large, and finally the single domain occupies the entire magnetic domain (around region III). This process is caused by the motion of the wall separating domains. When the magnetic field is increased further, the rotation of magnetization occurs in a domain, and the direction of magnetization corresponds to that of the applied field (region III – IV). The magnetization in the high magnetic field limit is saturation magnetization (M_s). Then, applying a magnetic field to the reverse direction of saturation magnetization, a residual magnetization appears at zero magnetic field, if magnetic anisotropy is included.

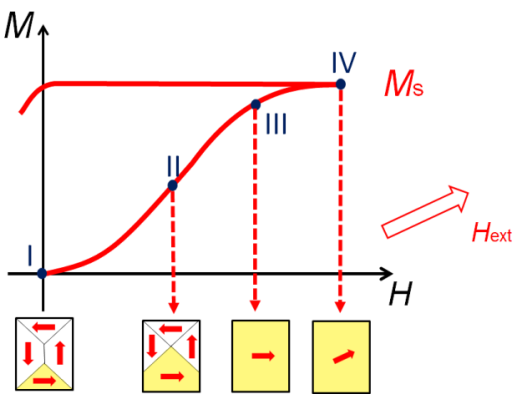

Figure 1.2. Typical hysteresis loop of ferromagnetic materials. In region I – III, the domain wall motion results in the growth of the yellow region. In region III – IV, the change of the arrow displays a rotation magnetization process to the H_{ext} direction.

The arrangement of magnetic moments in each domain can be determined by the energy balance between exchange interaction and the magnetic anisotropy. The small magnetic energy (magnetostatic energy) is likely to form a multi-magnetic domain structure.[7c] On the other hand, when the magnetic energy is large, a single magnetic domain is obtained. A single domain is composed with decreasing the minimum domain size.

A particle of a single magnetic domain can be regarded as a magnet. A coercivity of assembly of the particle is equal to an anisotropy field H_a. Without a domain wall motion in the particle, a magnetization process originates only in the rotation magnetization. This logic can be applied to SMMs systems, and details are described in Chapter 2 especially about the anisotropy as an origin of the activation energy in the Arrhenius behavior of the magnetization reversal.

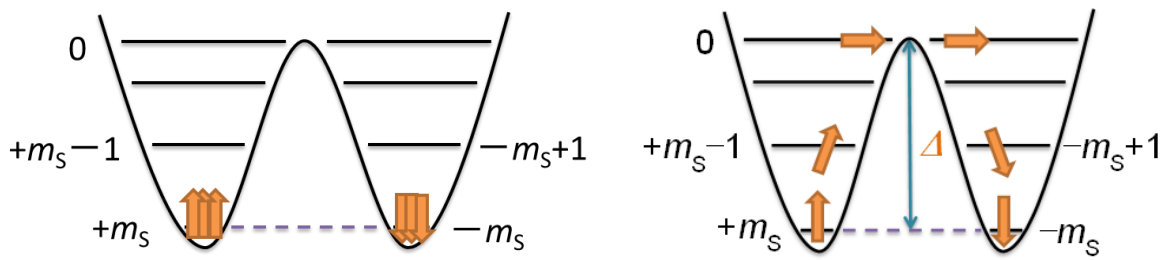

Figure 1.3. Slow relaxation of magnetization in SMMs with an easy axis.[2h,3b] (Left) Schematic representation of the splitting by ZFS and the relaxation of the magnetization from the 'spin-up' to 'spin-down' state at zero magnetic field and low temperature. (Right) the energy barrier associated with the magnetization reversal.

In a semi-classical view, the necessary condition of the magnetization reversal for SMMs is that molecules have a high enough energy to surmount an activation energy barrier U (or Δ)[2h,3b] (Figure 1.3). In Figure 1.3 (right), a time required for an up spin turning to a down spin is called a relaxation time, and it holds the Arrhenius's law.[3b] The longer the relaxation time, the stiffer the magnetization held. In an SMM with a unique giant spin state S, the activation energy barrier Δ can be expressed as $\Delta = |D|S^2$ (for integer spin systems),[3a-3d] where D is the uniaxial zero-field

splitting (ZFS) parameter at the ground state of the molecule. The ZFS parameter D is related to an anisotropy parameter of a bulk magnet. To achieve the slow magnetization relaxation, D value should be large and negative, and the ground state spin S should be as large as possible.[3a-3d] The projection of the total spin generates $(2S + 1)$ m_S states. The $(2S + 1)$ m_S value separates ranging from S to $-S$ one by one. Each m_S state corresponds to a different direction of the spin projection, which the low-energy level of $m_S = S$ can be considered 'all spin up' and that of $m_S = -S$ "all spin down" [Figure 1.3 (left)]. If the ZFS effect is absent, all of the m_S sublevels are degenerate, while the presence of ZFS leads to separate this degeneracy.[3b] Note that such discrete energy levels partly represent the quantum mechanical feature of SMMs, yet the quantum mechanical spin reversal process is not included at this stage.

1.3 Examples of SMMs

In the early 1990s, the first SMM of $Mn_{12}O_{12}(CH_3COO)_{16}(H_2O)_4$ was discovered, called Mn12ac.[3f,8] The molecule is composed of 12 manganese ions and is characterized as a ground state $S = 10$.[9] The relaxation time of the magnetization (τ_0) and the thermally activated energy barrier (Δ) of Mn12ac has been found $\tau_0 = 2.1\times10^{-7}$ s and $\Delta/k_B = 62$ K, respectively.[8] The Mn12ac has shown that some steps in the hysteresis loop on the exact measurements used field aligned crystals or a single crystal. These results are the evidence of quantum tunneling of magnetization in the works by Friedman group[10a] and Thomas group.[10b]

The quantum tunneling of magnetization (QTM) appears as step-like changes of magnetization. It attracts much attention as the first example of a macroscopically observable quantum reversal of magnetization. As the application of these phenomena, it is expected that quantum manipulation of SMM is possible, and their use for information storage materials may be realized.

In order to increase an activation energy barrier, 4f-based SMMs have been developed.[2] The

4f-based SMMs are typically in the ground multiplet with large total angular momentum J, which is composed of strongly coupled spin S and unquenched orbital angular momentum L. When 4f-based SMMs are investigated, the double-well of $\pm m_S$ levels shown in Figure. 1.3 is modified. In most cases, the J-multiplets split by spin–orbit coupling is large in energy, and only the lowest lying J state is populated at room temperature. The J value of the ground state gives rise to $(2J + 1)$ sublevels (or 'Stark' levels),[11] each with a quantum number m_J, which are perturbed by a ligand field effect. The splitting of the m_J levels by the ligand field effect is typically of the order of ca. 10^2 cm^{-1} (1 cm^{-1} = 1. 44 K) which is much smaller than the order of ca. 10^4 cm^{-1} by the spin–orbit coupling effect.[2b,12]

An example of the compound with a very high activation energy barrier is $[Tb^{III}(P_C)(Pc')]$, which contains one bare Pc (phthalocyanine) ring and one octa(*tert*-butylphenoxy)-substituted Pc' ring, and the energy barrier value is 936 K.[13] However, this compound does not work as an SMM at room temperature. In fact, the blocking temperature T_B, namely the temperature at which the SMM records hysteresis, is in many cases below 2 K. After many efforts of improving characteristics of SMMs, the Tb^{III} dinuclear compound $[K(18\text{-crown-}6)(THF)_2][\{[(Me_3Si)_2N]_2\text{-}(THF)Tb\}_2(\mu\text{-}\eta^2\text{:}\eta^2\text{-}N_2)]$ has been clarified to show the hysteresis loop up to 14 K, and the relatively high T_B 13.9 K has been recorded.[14] Also, the Fe^I mononuclear compound $[Fe(C(SiMe_3)_3)_2]_2^-$ shows the hysteresis loop below 4.5 K.[15a] A coercive field was improved using the N_2^{3-} radical for the former case. Owing to the structure having a low-coordinate transition-metal center with an odd electron system, a uniaxial anisotropy becomes strong for the latter case.[15b]

Other than low T_B, there is a problem that the magnetization relaxes fast for the QTM at zero magnetic field. Even if the hysteresis loop is observed in the magnetization curve, the decay of the remanent magnetization at zero magnetic field results in the loss of magnetic information. In other words, it cannot be used as information storage media. Consequently, it is necessary to improve

the molecular design to reduce the QTM at zero magnetic field. There is a strategy to reduce the QTM by introducing intermolecular coupling, which produces an exchange bias within the molecule. For an example, the $[Mn_4]_2$ dimer is known to have less QTM than the corresponding monomer by intermolecular interactions via C–H···Cl and the Cl···Cl pathways.[16] Such examples are also found in 4f-3d heterometalic compound $[Dy^{III}_2Cu^{II}]$ where exchange bias field is generated.[4b] The internal magnetic field is regarded as the same as an external magnetic field to the molecule, despite zero magnetic field. These strategies help the improvement of the coercivity of the SMMs prohibiting QTM at zero magnetic field.

1.4 Superexchange Interaction

When magnetic ions with local magnetic moments are coordinated in a complex, an exchange interaction gives rise to the magnetic coupling among magnetic moments (an exposition of exchange interaction is written in Section 1.7.4). So called superexchange interaction usually dominates such magnetic coupling.[17] Mechanism of superexchange interaction was first proposed by Kramers,[17a] later it was refined by Anderson.[17b] Suppose that there is an anion linking between two metal ions. When the orbital of anions accommodating overlaps to the adjacent orbits of two metal ions, these spins prefer the antiparallel arrangement. It is called an antiferromagnetic superexchange interaction. On the other hand, if there is the orthogonality of these orbitals, a ferromagnetic superexchange interaction appears. Therefore, the overlap and the orthogonality of orbitals involve an electronic state of metal ion and bridging atoms is essential to determine the nature of the superexchange interaction.

Let us see the case of two paramagnetic metal ions with octahedral coordination is bridged by a diamagnetic anion. The sign of superexchange interaction in such a simple system is determined by Goodenough-Kanamori rule.[18] The orbitals contributing to the superexchange are primarily 3d-orbitals in the transition metal ions and 2p-orbitals in the anions. The superexchange

interactions are operative in two ways. The one is a 180º superexchange (the M–X–M angle is 180º), and the other is a 90º superexchange (the M–X–M angle is 90º). In the case of the 180º superexchange, when two metal ions are conspecific, the interaction is antiferromagnetic. This sign alternate, when two metal ions are heterologous. Namely, when one has more-than-half 3d electrons, the other has less-than-half, a ferromagnetic interaction appears. In the case of the 90º superexchange, when two metal ions are conspecific except for d^5 as a Mn^{2+} ion, a ferromagnetic interaction realizes. When two metal ions are heterologous, the interaction is antiferromagnetic. The study of 3d homonuclear complexes is introduced upon the 90° superexchange interaction showing ferromagnetic character. However, the nature of superexchange with M–X–M bond with much smaller angles than 90° and with 4f–O–3d bonding are not well known.

1.5 Idea of Molecular Design

The author explains why a nickel(II) ion is chosen in the study on 3d homonuclear compounds and copper(II) and dysprosium(III) ions are selected in the study on 3d-4f heteronuclear compounds.

First, it is because a “cubane”-type structure (Figure 1.4) with a Ni_4O_4 cube often shows ferromagnetic interaction.[19] The contribution of ferromagnetic interaction in the “cubane”-type structure results from superexchange through O atoms rather than from the direct orbital overlap of two Ni ions.

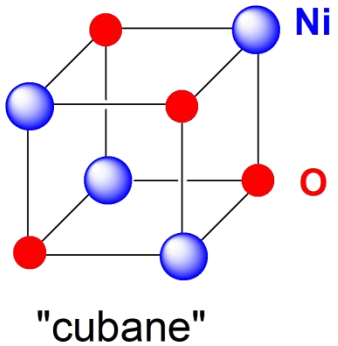

Figure 1.4. “Cubane”-type structure.

In general, the net magnitude of exchange interaction is given by the sum of contributions of ferromagnetic and antiferromagnetic interactions.[19a] It can be qualitatively described[19a] by the symmetry relationships between the e_g ($d_{x^2-y^2}$ and d_{z^2}) and t_{2g} (d_{xy}, d_{yz}, d_{zx}) orbitals of the four nickels and the s and p orbitals of the four O atoms. The ferromagnetically contributing pathways (Ni–O–Ni) are as follows. (1) $d_{x^2-y^2}$ (Ni)–p_y(O)–e_g (Ni). Because the p_y orbital is orthogonal both to the e_g orbitals, the interatomic interaction is ferromagnetic. (2) e_g (Ni)–s(O)– t_{2g} (Ni). Because the s orbital is orthogonal to the t_{2g} orbitals, similarly, the interatomic interaction is ferromagnetic. On the other hand, the antiferromagentically contributing pathway is e_g (Ni)–s(O)–e_g (Ni). Because the e_g orbitals all mutually overlap with the spherically symmetrical s orbital, the interatomic interaction is antiferromagnetic interaction. These pathway resultant contributions dominate ferromagnetic rather than antiferromagnetic interaction.

Second, development of SMM requires two conditions, large spin quantum number and strong uniaxial magnetic anisotropy. In order to acquire ground high spin and strong magnetic anisotropy, 3d-4f complexes attract considerable attention. For example, $[Cu^{II}LTb^{III}(hfac)_2]_2$ (H_3L = 1-(2-hydroxybenzamido)-2-(2-hydroxy-3-methoxybenzylideneamino)ethane and Hhfac = hexafluoroacetylacetone) exhibited slow magnetic relaxation in the ac magnetic susceptibility, and the activation energy barrier was Δ/k_B = 21 K.[4a] Osa and co-workers have obtained three findings: (1) 3d-4f complexes can be easily synthesized. (2) The ground high spin state is likely to accrue from a smaller number of metal ions than a polynuclear complex. (3) By using the 4f ions, it is possible to acquire strong magnetic anisotropy. While, $[\{Dy^{III}(hfac)_3\}_2\{Ni^{II}(bpca)_2\}]\cdot CHCl_3$ ($[Dy_2Ni]$) in which $bpca^-$ = bis(2-pyridylcarbonyl)amine anion, was studied to increase the blocking temperature T_B in SMMs.[4d] As before, the 4f ions generates strong magnetic anisotropy. To investigate the exchange interaction between a Ni^{2+} and two Dy^{3+} ions, $[\{Dy^{III}(hfac)_3\}_2\{Fe^{II}(bpca)_2\}]\cdot CHCl_3$ ($[Dy_2Fe]$) complex was also synthesized, where the Fe ion is diamagnetic.[4d] From the results of magnetic measurements, ferromagnetic interaction between the

Ni^{2+} and Dy^{3+} ions appeared in the difference of dc magnetic susceptibility between [Dy_2Ni] and [Dy_2Fe]. However, the activation energy barrier of [Dy_2Ni] was as low as Δ/k_B = 4.9± 0.3 K. The cause of the extremely small value is the orthogonal arrangement of the Dy^{3+} coordination polyhedrons. The structural conformation of these compounds can lead to the cancellation of a significant fraction of the Ising anisotropy of the two terminal Dy^{3+} ions.[4d] It is important to consider the structural conformation arranged in each parallel moment. In the two examples above, the exchange interaction between the 3d and 4f ions could not be determined. For example, $[Dy_2Cu_2]_n$ has been synthesized by Okazawa and co-workers, which the exact determination of exchange interaction on $[Dy_2Cu_2]_n$ has succeeded by means of HF-EPR measurements.[20a] The accurate determinations of exchange interaction have also succeeded as well as some other 4f-3d complexes.[20b,20c]

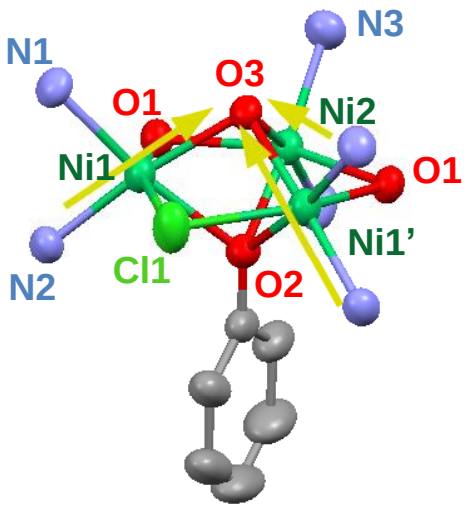

Figure 1.5. Each Ni^{2+} ion spin tiles to the direction of O3 atom.[21]

The author and co-workers attempted to enhance strong uniaxial anisotropy and to determine a magnetic anisotropy parameter quantitatively. In the previous work reported by Biswas, Ida, and co-workers[21] investigated the structure and magnetic properties of Ni^{II} trinuclear complexes $[Ni_3L_3(OH)(X)]\cdot(ClO_4)$ (L = 2-[(3-dimethylaminopropylimino)methyl]phenol; X = Cl^-, OCN^-,

N_3^-). These complexes possess μ_3-bridging oxygen atoms as a "cap" above and beneath the molecular plane. The each Ni^{2+} ion has a distorted octahedral structure (Figure 1.5). Ni–O distances in the octahedral structure are compressed, and each magnetic moment of Ni^{2+} tilts toward the Ni–O direction. Consequently, the total magnetic moment arises almost perpendicular from the Ni triangle plane. Based on this knowledge, the author obtained a strategy improving magnetic anisotropy, preparation accessibility, and facile analysis.

The knowledge of the exchange coupling mechanism would be useful for the development of bulk permanent magnets and refrigerants. In Gd–Cu systems, the ferromagnetic couplings between Gd^{3+} (S = 7/2) and Cu^{2+} (S = 1/2) are often observed.[22] It is noticed that a planar structure favors ferromagnetic coupling in the four-membered Cu–O–Gd–O moiety. The author and co-workers have developed a new microscopic method for the precise evaluation of exchange coupling in SMMs including heavy Ln ions,[20] and have established their usefulness in the studies of various 4f-3d-based SMMs.[23] In particular, Tb^{3+} and Dy^{3+} ions have magnetic anisotropy along the easy axis.[2b] The key is to use the high-frequency electron paramagnetic resonance (EPR) to observe the resonances of 3d transition metal ions biased by the exchange fields from Ln ions.

Recently, Ghosh, Ida, and co-workers[24] have shown that hinge-like coordination flexibility (*cisoid* and *transoid*; Scheme 1.1) can lead to the isolation of isomeric linear and bent structures for trinuclear $[[\{Cu^{II}(salpn)\}_2Ln^{III}(X)_n]$ (Ln^{3+} = Tb^{3+}, a non-Kramers ion), where the flexible nature of metallatecton led to an interesting structural diversity (H_2salpn = (*N,N′*-bis(salicylidene)-1,3-propanediamine)). They have evaluated the structures and the SMM properties of a long-known but less-investigated family of such a structure. The motivation of the present work is to investigate the SMM behavior and 4f-3d exchange coupling in derivatives involving Ln^{3+} = Dy^{3+} (a Kramers ion). They possess a DyO_2Cu structure in common. The ferromagnetic coupling by dc magnetic measurements and slow magnetization reorientation by ac magnetic susceptibility measurements for all complexes will be reported in Chapter 3.

Scheme 1.1. Hinge-like structures of $Tb(OCu)_2$ compounds.[24]

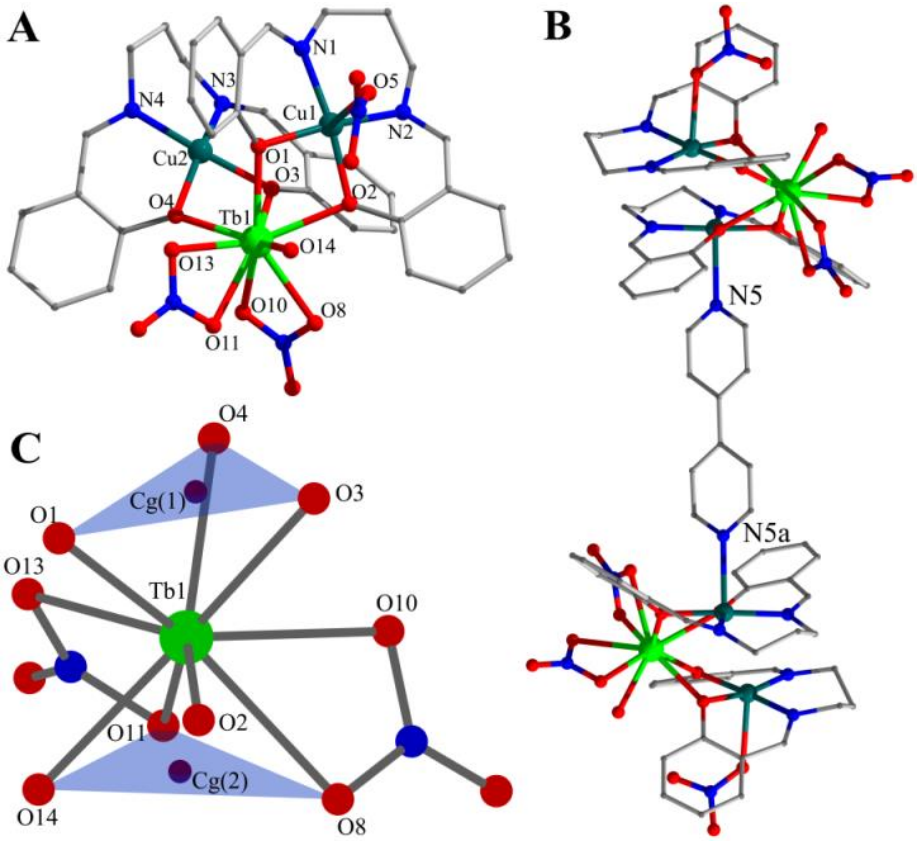

1.6 Outline

To promote a higher activation energy barrier is certainly important for development of SMMs. In order to comprehend the magnetic properties, the exchange coupling involved in homo- and heterometallic multinuclear complexes is one of the most essential magnetic parameters. The finding of exchange coupling mechanism would be very useful to create new bulk permanent magnets. Thus, the principal points in this thesis were devoted to the precise and reliable determination of magnetic parameters including exchange coupling parameters. The author establishes the purpose of this thesis as the following items: (1) To design easily accessible molecules with uniaxial magnetic anisotropy. (2) To find out relationship between the exchange

coupling parameter and structural parameters.

In Chapter 2, the author describes the study about the evaluation of magnetic parameters, uniaxial magnetic anisotropy, and intermolecular exchange coupling of the Ni triangle trinuclear complexes. Moreover, the presence or absence of performance of SMMs was investigated.

Chapter 3 deals with the study on the structures and magnetic properties of two trinuclear isomeric $DyCu_2$ compounds and one polymeric $DyCu_2$ compound. The exchange couplings of these compounds were evaluated by HF-EPR. Some relationship is found between these exchange couplings and geometrical parameters of each crystal structure.

In Chapter 4, the summary of the study and future perspectives are noted.

1.7 Theoretical Section

The following section cites general theories from the textbooks written by Olivier Kahn,[25] Dante Gatteschi,[8,26] and Robera Sessoli.[8,26]

1.7.1 Definitions and Units[25]

First, we consider a sample of 1 mol of compound within a direct current (dc) magnetic field H. The sample obtains a molar magnetization M related to H through

$$\frac{\partial M}{\partial H} = \chi \ , \tag{1.1}$$

where χ is the molar magnetic susceptibility. Reference axes always can be chosen due to being diagonal of χ with the χ_u ($u = x, y, z$) principal values. The magnetically isotropic sample becomes the χ to a scalar.

In the sufficiently weak magnetic field, χ is independent of H, and it can be expressed as

follows:

$$M = \chi H \,. \tag{1.2}$$

In general, magnetic parameters favor to use the cgsemu system in the field. Strictly speaking the unit of magnetic field is expressed in the Oersted (Oe). In the vacuum B is related to H through $B = \mu_0 H$, and the permeability μ_0 in the cgsemu system is equal to Eq. 1.1. Moreover, the molar magnetic susceptibility χ is expressed in $cm^3\ mol^{-1}$. The multiple of the molar magnetic susceptibility by the temperature χT is expressed in $cm^3\ K\ mol^{-1}$. The molar magnetization M is expressed in $N_A\mu_B$ units, where N_A is Avogadro's number and μ_B is the electronic Bohr magneton. The molar magnetization M of $N_A\mu_B$ is expressed, such as Eq. 1.3 in the cgsemu system.

$$1\ N_A\mu_B = 5585\ \mathrm{cm}^3\ \mathrm{G}\ \mathrm{mol}^{-1}. \tag{1.3}$$

1.7.2 Diamagnetic and Paramagnetic Susceptibilities[25]

In a principle χ_{obs}, the sum of two contributions correlated with:

$$\chi_{obs} = \chi^{D} + \chi^{P}\,, \tag{1.4}$$

where χ^D and χ^P represent the diamagnetic and paramagnetic susceptibility, respectively. The former is negative and the latter positive. When a χ^D dominates, the sample calls to be diamagnetic, which is repelled from the applied magnetic field. While, a χ^P dominates, the sample calls to be paramagnetic, which is attracted by the applied magnetic field.

Diamagnetism is inherent in a matter. The diamagnetism is due to the interaction that the electron makes a pair by the applied magnetic field. A χ^{D} qualifies that is independent of the temperature and the strong applied magnetic field. In the 1940s Pascal summarized data taking into account the application of these additive methods. Assuming the experimentally susceptibilities data considering corrected diamagnetic contribution χ^{D}, we will always use χ in the place of χ^{P} due to simplicity.

1.7.3 van Vleck Fomula[25]

In 1932 van Vleck suggested a simplification based on a few approximations for the molar paramagnetic susceptibility.[27] Firstly, the energies E_n are legitimately expanded according to the increasing power of H:

$$E_n = E_n^{(0)} + E_n^{(1)}H + E_n^{(2)}H^2 + \cdots, \tag{1.5}$$

where $E_n^{(0)}$ is the energy of level n in zero field. $E_n^{(1)}$ and $E_n^{(2)}$ are called first- and second-order Zeeman coefficients, respectively. A microscopic magnetization can be defined as $\mu_n = -\partial E_n/\partial H$. From Eq. 1.5, μ_n becomes

$$\mu_n = -E_n^{(1)} - 2E_n^{(2)}H + \cdots. \tag{1.6}$$

It is assumed that H is not too large and T not too low. From these approximations, we obtain

$$M = \frac{N_A \sum_n \mu_n \exp\left(-E_n / k_B T\right)}{\sum_n \exp\left(-E_n / k_B T\right)} = \frac{N_A \sum_n \left(-E_n^{(1)} - 2E_n^{(2)}H\right)\left(1 - E_n^{(1)}H / k_B T\right)\exp\left(-E_n^{(0)} / k_B T\right)}{\sum_n \left(1 - E_n^{(1)}Hk_B T\right)\exp\left(-E_n^{(0)} / k_B T\right)}. \tag{1.7}$$

In zero field, the energy states split the energy levels of vertical symmetry by the first-Zeeman effect because of the magnetization vanishing, such that $\Sigma_n E_n^{(1)}\exp(-E_n^{(0)}/k_B T) = 0$. Therefore, Eq. 1.7 and retaining only first-order term linear in H results in

$$M = \frac{N_A H \sum_n \left(E_n^{(1)2} / k_B T - 2E_n^{(2)}\right)\exp\left(-E_n^{(0)} / k_B T\right)}{\sum_n \exp\left(-E_n^{(0)} / k_B T\right)} \tag{1.8}$$

and finally

$$\chi = \frac{N_A \sum_n \left(E_n^{(1)2} / k_B T - 2E_n^{(2)}\right)\exp\left(-E_n^{(0)} / k_B T\right)}{\sum_n \exp\left(-E_n^{(0)} / k_B T\right)}, \tag{1.9}$$

which is called the van Vleck formula. The van Vleck equation gives the magnetic susceptibility only in the magnetic field range where the M vs. H plot is linear. If all energies E_n are linear in H, the second-order Zeeman coefficients $E_n^{(2)}$ vanish, and Eq. 1.9 becomes

$$\chi = \frac{N_A \sum_n E_n^{(1)2} \exp\left(-E_n^{(0)} / k_B T\right)}{k_B T \sum_n \exp\left(-E_n^{(0)} / k_B T\right)}. \tag{1.10}$$

1.7.4 Spin Hamiltonian[28]

In general, a spin vector coupling scheme can be expressed as a model the quantitative behavior of system with exchange-coupled spins of the whole molecule with the so called spin

Hamiltonian[29,30]

$$\hat{H} = -2\sum_{i,j} J_{ij}\hat{S}_i \cdot \hat{S}_j \ , \tag{1.11}$$

where the subscripts i and j correspond to the two different spins between nearest-neighbor sites. The J_{ij} is the exchange coupling constant, which the quantity implies the strength. When J is positive, the exchange interaction is ferromagnetic, while negative J denotes antiferromagnetic exchange interactions. The exchange interaction is often necessary to consider anisotropy. The magnetic interaction between two spins involving anisotropy can be described by the XYZ type spin Hamiltonian:

$$\hat{H} = -2\sum_{i,j} \left(J_x \hat{S}_{ix} \cdot \hat{S}_{jx} + J_y \hat{S}_{iy} \cdot \hat{S}_{jy} + J_z \hat{S}_{iz} \cdot \hat{S}_{jz} \right). \tag{1.12}$$

For $J_x = J_y = J_z \neq 0$, the isotropic Heisenberg case is applicable. If $J_z = 0$, $J_x = J_y \neq 0$ the interaction is named XY type. The case $J_x = J_y = 0$, $J_z \neq 0$ is applicable the Ising model, consists of only two states with up-spin and down-spin. Assuming Ising-type magnetic anisotropy, we can achieve a simplified description by taking account the lower energy states. The representation of Ising-type model is appropriate for systems with a large uniaxial anisotropy.

The Kambe vector coupling method[31] is very convenient, and an example of the triangular nickel(II) case is taken for a guidance of Chapter 2. If the three nickel(II) ions interact through the bridge, then the local spins $S_1 = S_2 = S_3 = 1$ are good quantum numbers. When exchange couplings $J_{12} = J_{23} = J_{31} = J$, the Heisenberg-Dirac-van Vleck spin Hamiltonian is written as

$$\hat{H} = -2J\left(\hat{S}_1 \cdot \hat{S}_2 + \hat{S}_2 \cdot \hat{S}_3 + \hat{S}_3 \cdot \hat{S}_1 \right). \tag{1.13}$$

Since $\hat{S}_T = \hat{S}_1 + \hat{S}_2 + \hat{S}_3$, hence $\hat{S}_T^2 = \hat{S}_1^2 + \hat{S}_2^2 + \hat{S}_3^2 + 2\hat{S}_1 \cdot \hat{S}_2 + 2\hat{S}_2 \cdot \hat{S}_3 + 2\hat{S}_3 \cdot \hat{S}_1$. The spin Hamiltonian is rewritten as

$$\hat{H} = -J(\hat{S}_T^2 - \hat{S}_1^2 - \hat{S}_2^2 - \hat{S}_3^2), \tag{1.14}$$

the eigenvalues of which are

$$E(S_T) = -JS_T(S_T + 1). \tag{1.15}$$

The obtained parameters are summarized in Table 1.1 and Figure 1.6, in the case of the energy of the spin interaction of the equilateral triangle.

Table 1.1. Energy level in an equilateral triangle model of $S = 1$.

S_T (total-spin degeneracy)	$E(S_T)$	$E(S_T)'$
3 (1)	$-12J$	0
2 (2)	$-6J$	$6J$
1 (3)	$-2J$	$10J$
0 (1)	0	$12J$

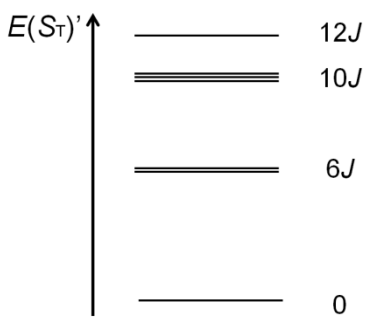

Figure 1.6. Diagram of the energy levels.

In Figure 1.6, $E(S_T)$' is $E(S_T)+12J$. In the case of an equilateral triangle model of $S = 1$ including the magnetic ions of the same species, the molar magnetic susceptibility is given by[32]

$$\chi = \frac{N_A g^2 \mu_B^2}{k_B T}\left[\frac{A}{B}\right] \tag{1.16}$$

with

$A = 28+20\exp(-6J/k_BT) +6\exp(-10J/k_BT)$

$B = 7+10\exp(-6J/k_BT) +9\exp(-10J/k_BT) +\exp(-12J/k_BT)$.

1.7.5 The Curie Law[25]

In general, we should consider the spin-orbit interaction in the case of the magnetic properties of lantanoid ions of 4f electron. Because lantanoid ions have closed-shells of $5s^2$ and $5p^6$ at the outside of the 4f orbital, shielding the influence of the ligand to the 4f electrons. As the electronic state of 4f electrons with smaller ligand interaction, the free electron state can be used, the contribution of spin-orbit interaction is large. Because 3d electrons of transition metal have no closed-shell, they are easily influenced by ligand interaction, and the orbital angular momentum of 3d electrons are fully or partially quenched.

The role of the orbital momentum cannot be ignored in the lantanoid ions of 4f electron. The magnitude of the spin-orbit coupling of 4f electron is much larger than that of 3d ions, which increases from the left to the right of the Periodic Table. This spin-orbit coupling partially removes the degeneracy of the $^{2S+1}\Gamma$ ground term. This gives $^{2S+1}\Gamma$ states, which a total angular momentum (J) defined as

$$J = L+S, \tag{1.17}$$

where L is an orbital quantum number, and S is a spin quantum number. The J varies by an integer value from $|L-S|$ to $L+S$.

When states have configurations $4f^1 - 4f^6$, the J is definable from $|L-S|$. In contrast, when states have configurations $4f^8 - 4f^{13}$, the J is definable from $L+S$. In the case of the configuration $4f^7$, there is no first-order angular momentum; namely, $L = 0$. The difference of energy levels between the state of lowest energy and the first excited state varies from $\sim 10^2$ to $\sim 10^3$ cm^{-1}. The energy state separation is plotted against ground electronic configuration, which is called the "Dieke diagram".[33] When this energy gap is small, the first excited state may be thermally populated. In contrast, when it is large, only the ground state is thermally populated. In general, the J value may be considered only for J^z of the ground state, which superscript of J^z represents the z-direction. The large energy gap is important to develop SMMs.

When the magnetism of a system is a well isolated ${}^{2S+1}\Gamma$ ground sate, J, L, and S are good quantum numbers. In applied magnetic field H, the ${}^{2S+1}\Gamma$ state is split into $2J+1$ components, the wavefunctions of which are noted $|J, m_J>$, with m_J varying by an integer value from $-J$ to $+J$. The energy $E(J, m_J)$ of the $|J, m_J>$ Zeeman component is

$$E(J, m_J) = \mu_B g_J m_J H \tag{1.18}$$

with

$$g_J = \frac{3}{2} + \frac{S(S+1) - L(L+1)}{2J(J+1)} \tag{1.19}$$

with varying by an integer value from $-J$ to $+J$. The molar magnetization M leads Eq. 1.10 to

$$M = N_{\mathrm{A}} g \mu_{\mathrm{B}} J B_J(x), \tag{1.20}$$

where $x = g\mu_B JB/k_B T$. $B_J(x)$ is the Brillouin function defined by

$$B_J(x) = \frac{2J+1}{2J}\coth\frac{2J+1}{2J}x - \frac{1}{2J}\coth\frac{1}{2J}x. \tag{1.21}$$

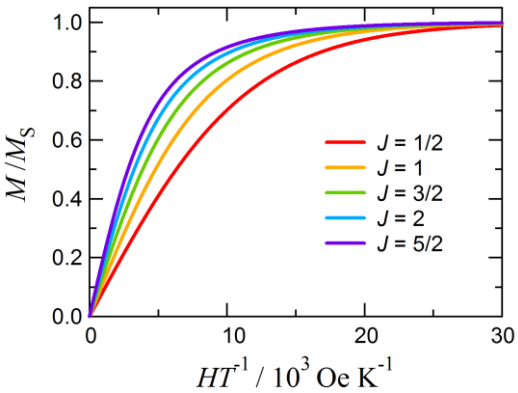

Figure 1.7. The Brillouin function shown as M/M_s vs. H/T plot.[25]

A plot of $B_J(x)$ for several values of J is illustrated in Figure 1.7. When x becomes very large; namely, at high field and low temperature, $B_J(x)$ is determined to one, and M achieves to the saturation magnetization M_S:

$$M_S = N_{\mathrm{A}} g_J \mu_{\mathrm{B}} J = 5585 \times g_J J \quad \mathrm{cm}^3 \ \mathrm{mol}^{-1}. \tag{1.22}$$

For $x << 1$, χ (= $\partial M/\partial H$) can be written as

$$\chi = \frac{N_A g_J{}^2 \mu_B{}^2 J(J+1)}{k_B T}. \tag{1.23}$$

Table 1.2. Theoretical Curie constants and g_J values of Gd^{3+}, Tb^{3+}, and Dy^{3+} ions.

	Gd	Tb	Dy
C / cm^3 K mol^{-1}	7.88	11.82	14.17
g_J	2	3/2	4/3

In this approximation the magnetic susceptibility obeys the Curie law. The values of g_J and χT calculated from (1.23) for the rare earth ions (Gd^{3+}, Tb^{3+}, and Dy^{3+}) are given in Table 1.2.

The molar magnetic susceptibility varies as

$$\chi = \frac{C}{T} \quad \left(C = \frac{N_A g_J{}^2 \mu_B^2 J(J+1)}{3k_B} \right). \tag{1.24}$$

The constant C depends on the spin multiplicity $2J+1$ of the ground state. This relation is called the Curie law where C is the Curie constant.

1.7.6 Ac Susceptibility[26,34]

Slow relaxation of magnetization is one of the interesting features of the magnetic behavior of a molecular cluster. This feature was first discovered in Mn12ac by ac susceptibility measurements.[8] The dynamic response of a specimen might be induced by applying oscillating magnetic field, which depends on the frequency ω of the field. In general, the response can be expressed as the sum of an in-phase component χ', and an out-of-phase component χ'', of the

susceptibility. If the change of the external oscillating magnetic field is slow compared with the relaxation time of the magnetization τ (i.e. $\omega << \tau^{-1}$), the magnetization is always in equilibrium over the time-scale of the experiment. The measured susceptibility corresponds to the static susceptibility, which called the isothermal susceptibility χ_T. If the frequency is much faster than the reorientation of the magnetization (i.e. $\omega >> \tau^{-1}$), the magnetic system is effectively isolated from the surrounding of the magnetization. Continuously, an adiabatic susceptibility χ_S is measured, which is smaller than χ_T. The dynamic susceptibility can be expressed as:

$$\chi(\omega) = \chi_S + \frac{\chi_T - \chi_S}{1 + (i\omega\tau)}. \tag{1.25}$$

Indeed, the susceptibility can be expressed by the real and imaginary parts as:

$$\chi = \chi' + i\chi'',$$

$$\chi' = \chi_S + \frac{\chi_T - \chi_S}{1 + (\omega\tau)^2},$$

and

$$\chi'' = \frac{(\chi_S - \chi_T)\omega\tau}{1 + (\omega\tau)^2}. \tag{1.26}$$

Eq. 1.25 represents the Debye-type relaxation,[35] which is the response of an ideal with one relaxation time. The real part of susceptibility χ' is in dispersion, and the imaginary part of susceptibility χ" is in absorption, as shown in Figure 1.8. When χ" is plotted against χ', it is called the Argand or Cole-Cole plot,[36,37] which a semicircle is drawn. The two parameters χ_S and χ_T can be extracted as the two zero-cross points of the semicircle against the χ" axis (see Figure 1.9), being constrained such that $\chi_T > \chi_S$. The experimental curve is fitting by the following expression:

$$\chi(\omega) = \chi_S + \frac{\chi_T - \chi_S}{1 + (i\omega\tau)^{1-\alpha}},$$

and

$$\chi'(\omega) = \chi_S + (\chi_T - \chi_S)\frac{1 + (\omega\tau)^{1-\alpha}\sin(\pi\alpha/2)}{1 + 2(\omega\tau)^{1-\alpha}\sin(\pi\alpha/2) + (\omega\tau)^{2-2\alpha}},$$

$$\chi''(\omega) = (\chi_S - \chi_T)\frac{(\omega\tau)^{1-\alpha}\cos(\pi\alpha/2)}{1 + 2(\omega\tau)^{1-\alpha}\sin(\pi\alpha/2) + (\omega\tau)^{2-2\alpha}}. \quad (1.27)$$

The experimental data in the Cole-Cole plot enable us to give α. The scalloped central angle of semicircle is given by $\pi(1-\alpha)$, as shown in Figure 1.9.

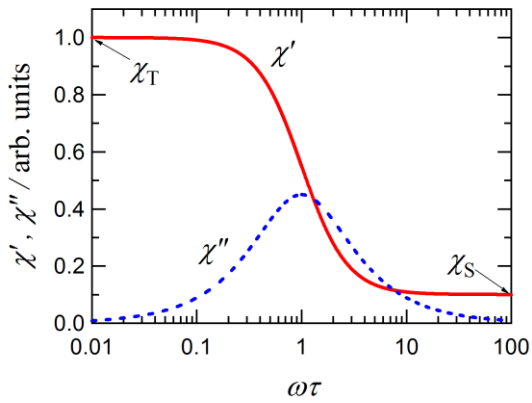

Figure 1.8. Theoretical frequency dependence of the real and imaginary component of the magnetic susceptibility in a semi-log scale. χ_T and χ_S are the isothermal and adiabatic limits of the susceptibility, respectively.[34]

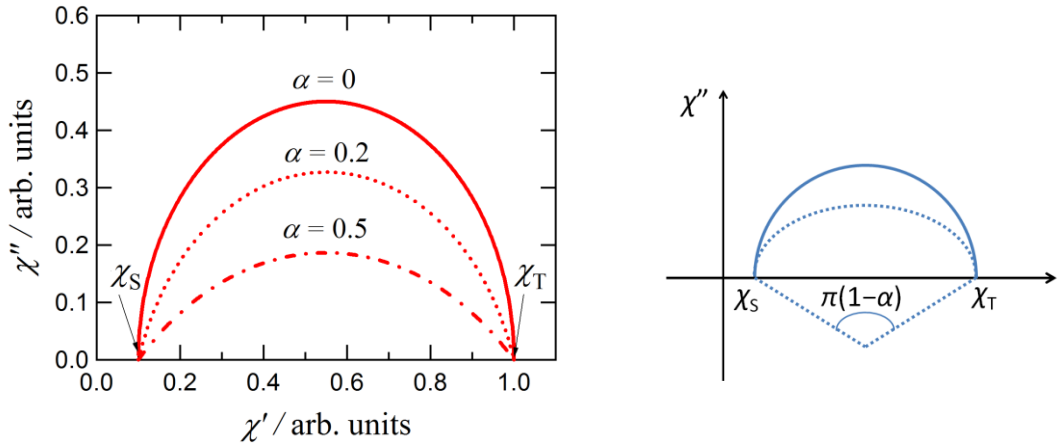

Figure 1.9. Cole-Cole plot where at a given temperature χ'' is plotted versus χ', for each frequency. Solid line: no distribution in relaxation time (e.g. $\alpha = 0$); broken line: a distribution in α according to Eq. 1.27 (e.g. $\alpha = 0.2$ and 0.5).[26]

1.8 Experimental Section

The measurement instruments and the common measurement conditions used in the following Chapters are described below. For details, see the relevant Chapters.

Dc and Ac Magnetic Measurements. The dc magnetic susceptibilities and magnetizations of polycrystalline and powder specimens were measured on a SQUID magnetometer (MPMS-XL7, Quantum Design, Inc.) at temperatures from 1.8 to 300 K. The magnetization was measured in the static external field from 0 to 7 T. Diamagnetic contribution arising from the sample holder was corrected by subtracting separately measured blank data. The diamagnetism of intrinsic in the sample was deduced by using Pascal's constants.[25b] Ac magnetic susceptibilities were measured on a PPMS ac/dc magnetometer (Quantum Design, Inc.) down to 1.9 K and up to 20 K at zero field and any dc bias field.

Low-temperature magnetization of compounds was measured by means of a conventional inductive probe in pulsed-magnetic fields. The temperature when used a ^{3}He cryostat was reached as low as 0.5 K.[38] A polycrystalline specimen was mounted in a capillary made of Kapton. The

sample was not held on the sample tube, which was allowed to align in the magnetic field direction. When several shots of the magnetic field, the orientation effect of magnetization was saturated. Therefore, the identification magnetization curves were recorded.

High-Frequency Electron Paramagnetic Resonance. HF-EPR spectra for polycrystalline and powder samples were measured from 95 to 450 GHz in temperatures range of 1.7 – 40 K by using the TESRA-P EPR spectrometer installed at Institute for Materials Research, Tohoku University.[39] The sample was packed in a case made of polyethylene. Gunn oscillators and backward traveling wave oscillators were utilized as radiation sources with an InSb applied as detector.[39]

The used measurement instruments and simulation software in Chapter 2 are as follows.

TG-DTA Measurements. Simultaneous thermogravimetry and differential thermal analysis was performed on a Rigaku Thermo Plus TG8120. The temperature scan rates were ranged from 2 to 15 deg/min.

Heat Capacity Measurements. A heat capacity of a single crystal specimen in zero magnetic field was measured on a Quantum Design PPMS model 6000 according to the relaxation method. The sample was glued onto a calorimetric platform with a small amount of Apiezon N grease. The temperature was scanned range of 2 – 300 K. The contribution of the addenda was subtracted from the gross data including experimental data.

Crystal Structure Analysis. X-ray diffraction data were collected on a Saturn70 CCD diffractometer using graphite monochromated MoKα radiation (λ = 0.71073 Å). The structure was directly solved by means of a heavy atom method and expanded using Fourier techniques in the CRYSTALSTRUCTURE 4.0 program package.[40] The thermal displacement factors of non-hydrogen atoms were anisotropically refined. After those of hydrogen atoms were placed at calculated positions, the hydrogen atoms were isotropically optimized by using a riding model. Full-matrix least-squares methods were applied using all the unique reflection data. The Miller indices of a

single crystal specimen were determined on a Rigaku R-axis RAPID IP diffractometer at room temperature using graphite-monochromated MoKα radiation.

Simulation Study. All of the simulation studies were carried out the MAGPACK software version 00.1[41] running on Windows and Macintosh PCs.

References

(1) (a) J. S. Miller, A. J. Epstein, *MRS Bull.* **2000**, *25*, 21; (b) J. S. Miller, *Adv. Mater.* **2002**, *14*, 1105.

(2) (a) N. Ishikawa, M. Sugita, T. Ishikawa, S.-y. Koshihara, Y. Kaizu, *J. Am. Chem. Soc.* **2003**, *125*, 8694; (b) J. D. Reinhart, J. R. Long, *Chem. Sci.* **2011**, *2*, 2078; (c) D. N. Woodruff, W. R. E. P. Winpenny, R. A. Layfield, *Chem. Rev.* **2013**, *113*, 5110; (d) R. Sessoli, A. K. Powell, *Coord. Chem. Rev.* **2009**, *253*, 2328; (e) M. Andruh, J. P. Costes, C. Diaz, S. Gao, *Inorg. Chem.* **2009**, *48*, 3342; (f) P. H. Lin, T. J. Burchell, L. Ungur, L. F. Chibotaru, W. Wernsdorfer, M. Murugesu, *Angew. Chem.*, *Int. Ed.* **2009**, *48*, 9489; (g) J. D. Rinehart, M. Fang, W. J. Evans, J. R. Long, *Nature Chem.* **2011**, *3*, 538; (h) H. L. C. Feltham, S. Brooker, *Coord. Chem. Rev.* **2014**, *276*, 1; (i) P. Zhang, L. Zhang, C. Wang, S. F. Xue, S. Y. Lin, J. K. Tang, *J. Am. Chem. Soc.* **2014**, *136*, 4484; (j) S. Yamauchi, T. Fujinami, N. Matsumoto, N. Mochida, T. Ishida, Y. Sunatsuki, M. Watanabe, M. Tsuchimoto, C. Coletti, N. Re, *Inorg. Chem.* **2014**, *53*, 5961.

(3) (a) D. Gatteschi, R. Sessoli, J. Villain, *Molecular Nanomagnets*, Oxford University Press, New York, **2006**; (b) D. Gatteschi, R. Sessoli, *Angew. Chem.*, *Int. Ed.* **2003**, *42*, 268; (c) *Single-Molecule Magnets and Related Phenomena*, ed. by R. Winpenny, Springer-Verlag Berlin, **2006**; (d) L. Bogani, W. Wersdorfer, *Nature Mat.* **2008**, *7*, 179; (e) P. D. W. Boyd, Q. Li, J. B. Vincent, K. Folting, H.-R. Chang, W. E. Streib, J. C. Huffman, G. Christou, D. N. Hendrickson, *J. Am. Chem. Soc.* **1988**, *110*, 8537; (f) A. Caneschi, D. Gatteschi, R. Sessoli, *J. Am. Chem. Soc.* **1991**, *113*, 5873; (g) R. Sessoli, H.-L. Tsai, A. R. Schake, S. Wang, J. B. Vincent, K. Folting, D. Gatteschi, G. Christou, D. N. Hendrickson, *J. Am. Chem. Soc.* **1993**, *115*, 1804; (h) J. R. Friedman, M. P. Sarachik, *Annu. Rev. Condens. Matter Phys.* **2010**, *1*, 109; (i) G. Christou, *Polyhedron* **2005**, *24*, 2065; (j) K. S. Pedersen, J. Bendix, R. Clérac, *Chem. Commun.* **2014**, *50*, 4396; (k) T. Glaser, *Chem. Commun.* **2011**, *47*, 116.

(4) (a) S. Osa, T. Kido, N. Matsumoto, N. Re, A. Pochaba, J. Mrozinski, *J. Am. Chem. Soc.* **2004**, *126*, 420; (b) F. Mori, T. Nyui, T. Ishida, T. Nogami, K.-Y. Choi, H. Nojiri, *J. Am. Chem. Soc*. **2006**, *128*, 1440; (c) S. Ueki, T. Ishida, T. Nogami, K.-Y. Choi, H. Nojiri, *Chem. Phys. Lett.* **2007**, *440*, 263; (d) F. Pointillart, K. Bernot, R. Sessoli, D. Gatteschi, *Chem. Eur. J.* **2007**, *13*, 1602; (e) R. Murakami, T. Ishida, S. Yoshii, H. Nojiri, *Dalton Trans.* **2013**, *42*, 13968; (f) T. Kanetomo, S. Yoshii, H. Nojiri, T. Ishida, *Inorg. Chem. Front.* **2015**, *2*, 860.

(5) (a) M. A. Novak, R. Sessoli, *Quantum Tunneling of magnetization−QTM'94*, ed. by L. Gunther, B. Barbara, Springer Netherlands, **1995**, pp. 171–188; (b) E. C. Stoner, E. P. Wohlfarth, *Philos. Trans. R. Soc., A* **1948**, *240*, 599.

(6) (a) E. Brück, *J. Phys. D Appl. Phys.* **2005**, *38*, R381; (b) Y.-Z. Zheng, M. Evangelisti, F. Tuna, R. E. P. Winpenny, *J. Am. Chem. Soc.* **2012**, *134*, 1057.

(7) (a) P. Weiss, *Comptes Rendus* **1906**, *143*, 1136; (b) B. D. Cullity, C. D. Graham *Introduction to Magnetic Materials,* 2nd ed., Wiley-IEEE Press, New York, **2008**, pp.116; (c) C. Kittel. *Rev. Mod. Phys.* **1949**, *21*, 541.

(8) R. Sessoli, D. Gatteschi, A. Caneschi, M. A. Novak, *Nature* **1993**, *365*, 141.

(9) T. Lis, *Acta Crystallogr.*, *Sect. B* **1980**, *36*, 2042.

(10) (a) J. R. Friedman, M. P. Sarachik, J. Tejada, R. Ziolo, *Phy. Rev. Let.* **1996**, *76*, 3830; (b) L. Thomas, F. Lionti, R. Ballou, D. Gatteschi, R. Sessoli, B. Barbara, *Nature* **1996**, *385*, 145.

(11) J. P. Sutter, M. L. Kahn, *Magnetism: Molecules to Materials*, Wiley-VCH, Weinheim, **2005**.

(12) J. D. Reinhart, J. R. Long, *Chem. Sci.* **2011**, *2*, 2078.

(13) C. R. Ganivet, B. Ballesteros, G. de la Torre, J. M. Clemente-Juan, E. Coronado, T. Torres, *Chem. Eur. J.* **2013**, *19*, 1457.

(14) J. D. Rinehart, M. Fang, W. J. Evans, J. R. Long, *J. Am. Chem. Soc.* **2011**, *133*, 14236.

(15) (a) J. M. Zadrozny, D. J. Xiao, M. Atanasov, G. J. Long, F. Grandjean, F. Neese, J. R. Long, *Nature Chem.* **2013**, *5*, 577; (b) A. K. Bar, C. Pichon, J.-P. Sutter, *Coord. Chem. Rev.* **2016**, *308*, 346.

(16) W. Wernsdorfer, N. Aliaga-Alcalde, D. N. Hendrickson, G. Christou, *Nature* **2002**, *416*, 406.

(17) (a) H. A. Kramers, *Physica* **1934**, *1*, 182; (b) P. W. Anderson, *Phys. Rev*. **1950**, *79*, 350.

(18) (a) P. W. Anderson, *Phys. Rev*. **1959**, *115*, 2; (b) J. Kanamori, *J. Phys. Chem. Solids* **1959**, *10*, 87; (c) J. B. Goodenough, *J. Phys. Chem. Solids* **1958**, *1*, 287; (d) H. Oshio, M. Nakano, *Chem. Eur. J.* **2005**, *11*, 5178.

(19) (a) J. A. Bertrand, A. P. Ginsberg, R. I. Kaplan, C. E. Kirkwood, R. L. Martin, R. C. Sherwood, *Inorg. Chem.* **1971**, *10*, 240; (b) A. K. Ghosh, M. Shatruk, V. Bertolasi, K. Pramanik, D. Ray, *Inorg. Chem.* **2013**, *52*, 13894; (c) J. A. Barnes, W. E. Hatfield, *Inorg. Chem.* **1971**, *10*, 2355; (d) C. Ding, C. Gao, S. Ng, B. Wang, Y. Xie, *Chem. Eur. J.* **2013**, *19*, 9961; (e) A. Ferguson, M. Schmidtmann, E. K. Brechinb, M. Murrie, *Dalton Trans.* **2011**, *40*, 334; (f) H.-S. Wang, Y. Song, *Inorg. Chem. Commun.* **2013**, *35*, 86; (g) J.-P. Sun, L.-C. Li, X.-J. Zheng, *Inorg. Chem. Commun.* **2011**, *14*, 877; (h) M. A. Halcrow, J.-S. Sun, J. C. Huffman, G. Christou, *Inorg. Chem.* **1995**, *34*, 4167; (i) A. Burkhardt, E. T. Spielberg, S. Simon, H. Görls, A. Buchholz, W. Plass, *Chem. Eur. J.* **2009**, *15*, 1261; (j) A. D. Katsenis, V. G. Kessler, G. S. Papaefstathiou, *Dalton Trans.* **2011**, *40*, 4590; (k) A. Das, F. J. Klinke, S. Demeshko, S. Meyer, S. Dechert, F. Meyer, *Inorg. Chem.* **2012**, *51*, 8141.

(20) (a) A. Okazawa, T. Nogami, N. Nojiri, T. Ishida, *Chem. Mater.* **2008**, *20*, 3110; (b) T. Shimada, A. Okazawa, N. Kojima, S. Yoshii, H. Nojiri, T. Ishida, *Inorg. Chem.* **2011**, *50*, 10555; (c) T. Ishida, R. Watanabe, K. Fujiwara, A. Okazawa, N. Kojima, G. Tanaka, S. Yoshii, H. Nojiri, *Dalton Trans.* **2012**, *41*, 13609.

(21) R. Biswas, Y. Ida, M. L. Baker, S. Biswas, P. Kar, H. Nojiri, T. Ishida, A. Ghosh, *Chem. Eur. J.* **2013**, *19*, 3943.

(22) (a) A. Bencini, C. Benelli, A. Caneschi, R. I. Carlin, A. Dei, D. Gatteschi, *J. Am. Chem. Soc.* **1985**, *107*, 8128; (b) N. Matsumoto, M. Sakamoto, H. Tamaki, H. Okawa, S. Kida, *Chem. Lett.* **1990**, *19*, 853; (c) O. Guillow, P. Bergerat, O. Kahn, E. Bakalbassis, K. Boubekeur, P. Batail, M. Guillot, *Inorg. Chem.* **1992**, *31*, 110; (d) M. Andruh, I. Ramade, E. Codjovi, O. Guillou, O. Kahn, J. C. Trombe, *J. Am. Chem. Soc.* **1993**, *115*, 1822; (e) J.-P. Costes, F. Dahan, A. Dupuis, *Inorg. Chem.* **2000**, *39*, 5994; (f) J.-P. Costes, F. Dahan, A. Dupuis, J.-P. Laurent, *Inorg. Chem.* **2000**, *39*, 169; (g) J.-P. Costes, F. Dahan, A. Dupuis, J.-P. Laurent, *Chem. Eur. J.* **1998**, *4*, 1616; (h) T. Kido, Y. Ikuta, Y. Sunatsuki, Y. Ogawa, N. Matsumoto, N. Re, *Inorg. Chem.* **2003**, *42*, 398; (i) M. Evangelisti, M. L. Kahn, J. Bartolome, L. J. de Jongh, C. Meyers, J. Leandri, Y. Leroyer, C. Mathoniere, *Phys. Rev. B* **2003**, *68*, 184405.

(23) (a) S. Ueki, A. Okazawa, T. Ishida, T. Nogami, H. Nojiri, *Polyhedron* **2007**, *26*, 1970; (b) A. Okazawa, T. Nogami, H. Nojiri, T. Ishida, *Inorg. Chem.* **2008**, *47*, 9763; (c) A. Okazawa, T. Nogami, H. Nojiri, T. Ishida, *Inorg. Chem.* **2009**, *48*, 3292; (d) A. Okazawa, R. Watanabe, H. Nojiri, T. Nogami, T. Ishida, *Polyhedron* **2009**, *28*, 1808; (e) A. Okazawa, R. Watanabe, M. Nezu, T. Shimada, S. Yoshii, H. Nojiri, T. Ishida, *Chem. Lett.* **2010**, *39*, 1331; (f) A. Okazawa, K. Fujiwara, R. Watanabe, N. Kojima, S. Yoshii, H. Nojiri, T. Ishida, *Polyhedron* **2011**, *30*, 3121; (g) R. Watanabe, K. Fujiwara, A. Okazawa, G. Tanaka, S. Yoshii, H. Nojiri, T. Ishida, *Chem. Commun.* **2011**, *47*, 2110; (h) K. Fujiwara, A. Okazawa, G. Tanaka, S. Yoshii, H. Nojiri, T. Ishida, *Chem. Phys. Lett*. **2012**, *530*, 49; (i) A. Okazawa, T. Shimada, N. Kojima, S. Yoshii, H. Nojiri, T. Ishida, *Inorg. Chem.* **2013**, *52*, 13351.

(24) S. Ghosh, Y. Ida, T. Ishida, A. Ghosh, *Cryst. Growth Des.* **2014**, *14*, 2588.

(25) (a) O. Kahn, *Molecular Magnetism*; VCH: Weinheim, Germany, **1993**; (b) O. Kahn, *Molecular Magnetism*; VCH: Weinheim, Germany, Chapter 1, Table I.1, **1993**.

(26) D. Gatteschi, R. Sessoli, J. Villain, *Molecular Nanomagnets*; Oxford University Press: New York, USA, **2006**.

(27) J. H. van Vleck, *The Theory of Electric and Magnetic Susceptibilities*; Oxford University Press: Oxford, UK, **1932**.

(28) C. J. O'Connor, *Reseach Frontiers in Magnetochemistry*; World Scientific: Singapore, **1993**.

(29) W. Z. Heisenberg, *Physik*. **1926**, *38*, 411.

(30) P. A. M. Dirac, *Proc. Roy. Soc. A* **1926**, *112*, 661.

(31) K. Kambe, *J. Phys. Soc. Jpn.* **1950**, *5*, 48.

(32) G. A. Kakos, G. Winter, *Aust. J. Chem.* **1970**, *23*, 15.

(33) G. H. Dieke, H. M. Crosswhite, *Appl. Opics* **1963**, *2*, 675.

(34) J. S. Miller, M. Drillon, *Magnetism: Molecules to Materials III*; Wiley-VCH: Weinheim, Germany, **2002**.

(35) J. McConnell, *Rotational Brownian Motion and Dielectric Theory*; Academic Press: New York, USA, **1980**.

(36) K. S. Cole, H. R. Cole, *J. Chem. Phys.* **1941**, *9*, 341.

(37) C. Dekker, A. F. M. Arts, H. W. Wijn, A. J. van Duyneveldt, J. A. Mydosh, *Phys. Rev. B* **1989**, *40*, 11243.

(38) H. Nojiri, K.-Y. Choi, N. Kitamura, *J. Magn. Magn. Mater.* **2007**, *310*, 1468.

(39) H. Nojiri, Y. Ajiro, T. Asano, J.-P. Boucher, *New J. Phys.* **2006**, *8*, 218.

(40) *CRYSTALSTRUCTURE, version 4.0,* Rigaku/MSC, The Woodlands, TX 77381, USA, **2010**.

(41) (a) J. J. Borrás-Almenar, J. M. Clemente-Juan, E. Coronado, B. S. Tsukerblat, *Inorg. Chem.* **1999**, *38*, 6081; (b) J. J. Borrás-Almenar, J. M. Clemente-Juan, E. Coronado, B. S. Tsukerblat, *J. Comput. Chem.* **2001**, *22*, 985.

2 Study on Triangular Ni_3 Complexes

2.1 Abstract

In the 3d ion-based system of SMMs, the relatively high energy barrier Δ and ground high spin polynuclear compounds are required. To design easily accessible molecules with uniaxial magnetic anisotropy, the author and co-workers have prepared a novel nickel(II) trinuclear compound $[Ni_3(tmen)_3(\mu_2\text{-}Cl)_3(\mu_3\text{-}OMe)(\mu_3\text{-}OH)](BPh_4)\cdot 0.5MeOH\cdot 0.5CH_2Cl_2$ (**1**; tmen = *N*, *N*, *N*',*N*'-tetra-methylethylenediamine) with a characteristic trigonal bipyramid structure. For comparison with **1**, two known compounds $[Ni_3(tmen)_3(\mu_2\text{-}X)_3(\mu_3\text{-}X)(\mu_3\text{-}OH)]X$ (X = Cl (**2**), Br (**3**)) were also investigated. The magnetic studies clarified the ground high-spin (S = 3) state, which the intramolecular exchange coupling parameters were determined as $2J/k_B$ = 18.0±0.2, 27.2±0.2, and 19.6±0.2 K for **1**, **2**, and **3**, respectively. From the crystallographic analysis, the axes of triangular Ni molecular of **1** are aligned almost parallel in the crystallographic *b* axis. In addition, relatively short intermolecular Cl···Cl distances (3.725(1) and 3.847(2) Å) are found among linearly arrayed Ni_3 molecules. Thanks to the molecular arrangement in this manner, two magnetic parameters, zero-field-splitting $D_{S=3}$ and intermolecular exchange coupling parameters j could be estimated. The zero-field-splitting parameter $D_{S=3}/k_B$ = −2.2±0.1 K was obtained by the single-crystal magnetic study, and the intermolecular exchange coupling parameter was determined as $2j/k_B$ = −0.14±0.01 K from simulation. The intermolecular exchange coupling parameter is also possible to predict from the pulsed-field magnetization study. The magnetization on **1** at 0.5 K showed a jump at ca. 1.2 T. The alternating current magnetic susceptibility measurements revealed the Arrhenius behavior with E_a = 10.1±0.8 K at zero bias field. Therefore, the magnetic properties of **1** can be understood as an antiferromagnetic chain consisting of potential single-molecule magnets.

2.2 Introduction

The background and characteristics of the single-molecule magnets (SMMs) have been described in Chapter 1, and this section will make a brief introduction. SMMs of Mn12ac have appeared in the early 1990s, and they are supposed to have the potential applications for information storage media and quantum computing at the molecular level.[1-3] These 3d systems show slow magnetization relaxation, which requires the magnetic anisotropy barrier (Δ) regulated with $\Delta = |D|S^2$ for integer S, where S is the spin quantum number, and D is the zero-field splitting parameter as uniaxial anisotropy.[1] To increase Δ, it is important to develop ground high-spin polynuclear complexes having intermolecular ferromagnetic couplings.[2,4] In addition to the examples of the Mn_{12} family,[5] there are samples of SMMs from Co_4 and Ni_4 polynuclear complexes.[6,7] Their structures involve cubane, half-cubane, and/or fused-cubane motifs.[8] Reducing the nuclearity seems to be another attractive issue for easy accessibility,[9] and the ultimate in this direction has been realized in single-ion magnets.[10]

From the work of Ghosh's group, the Ni_3-based molecules exhibiting SMM character have been developed, $[Ni_3L_3(OH)(X)]\cdot(ClO_4)$ where L = 2-[(3-dimethylaminopropylimino)methyl]-phenol; X = Cl^-, OCN^-, N_3^-). They possess an X-bridge atom and two μ_2-bridging oxygen atoms as a "belt" (X) on the molecular plane and μ_3-bridging oxygen atoms as a "cap" (Y^1, Y^2) above and beneath the molecular plane (see Scheme 2.1).[11] These compounds have a ground high spin S = 3 state, owing to intramolecular ferromagnetic interactions. Despite the low symmetry due to the presence of different "belt" bridges, the intramolecular exchange coupling parameters were determined by assuming a three-fold symmetry.

In the present work, the author and co-workers utilized ligands as simplified as possible and have actually prepared a novel triangular compound $[Ni_3(tmen)_3(\mu_2\text{-}Cl)_3(\mu_3\text{-}OMe)(\mu_3\text{-}OH)]\text{-}(BPh_4)\cdot 0.5MeOH\cdot 0.5CH_2Cl_2$ (**1**; tmen = *N*,*N*,*N*',*N*'-tetramethylethylenediamine or tmeda) having an approximate D_{3h} symmetry for the complex cation moiety (Scheme 2.1). In this regard, there

have been a few reports on triangular nickel(II) compounds having a three-fold symmetry. Two known compounds $[Ni_3(tmen)_3(\mu_2\text{-}X)_3(\mu_3\text{-}X)(\mu_3\text{-}OH)]X$ (X = Cl (**2**), Br (**3**))[12,13] with symmetrical "belt" bridges also seem to be attractive. Their synthesis and structures have already been reported, but no magnetic properties were known. The ground spin states for **2** and **3** will be clarified, which have the similarity with **1** in their magnetic properties.

Scheme 2.1. Trigonal bipyramid skeleton and coordination atoms of **1 – 3**.

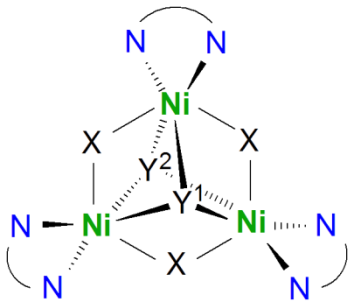

1 : X = Cl, Y^1 = OH, Y^2 = OCH_3

2 : X = Y^1 = Cl, Y^2 = OH

3 : X = Y^1 = Br, Y^2 = OH

The group theory tells us that molecules with a three-fold (or more) axis has a rhombic anisotropy parameter $E = 0$, and the uniaxial anisotropy D direction corresponds to the molecular axis.[14] The absence of E will lead to raising an effective activation energy of the magnetization reversal. Furthermore, such a symmetrical structure will also justify the prevalence of a unique exchange coupling. Hence, the magnetic analyses of **1 – 3** will be simpler than those of the lower symmetry ones.[11] Compound **1** exhibited peculiar low-dimensional properties due to intermolecular interaction, and as the last portion in this report the dynamical properties of weakly coupled SMMs with intermolecular antiferromagnetic interaction will be discussed.

2.3 Experimental Section

Preparation of $[Ni_3(tmen)_3(\mu_2\text{-}Cl)_3(\mu_3\text{-}OMe)(\mu_3\text{-}OH)](BPh_4)\cdot 0.5MeOH\cdot 0.5CH_2Cl_2$ (1). To a green solution of $NiCl_2\cdot 6H_2O$ (0.487 g, 2.1 mmol) in MeOH (6 mL) was added *N*,*N*,*N*',*N*'-

tetramethylethylenediamine (tmen) (0.32 mL, 2.2 mmol) and $NaBPh_4$ (0.240 g, 0.7 mmol). The resultant mixture was heated in a Discover microwave oven (CEM Corporation) at below 60°C and 200 W for 20 min, affording yellowish green powder. The powder was collected on a filter, washed with MeOH, and recrystallized from an 8/2 MeOH/dichloromethane mixed-solvent after insoluble impurity was filtered off with celite. Green crystals of **1** (48 mg (7%)) with m.p. 215°C (decomp.) were obtained. IR spectra were recorded on a Nicolet FT-IR spectrometer. IR (neat, attenuated total reflection): 3655 (O-H), 2873 (CH_3), 1463, 775, 700, 610 cm^{-1}. The elemental analysis (C, H, N) of their complexes on a PerkinElmer CHNS/O 2400 supported the chemical composition. Anal. Calcd.: C, 50.01; H, 7.15; N, 8.12% for $C_{44}H_{75}BCl_4N_6Ni_3O_{2.5}$; found: C, 50.35; H, 7.31; N, 8.12%. Crystal structure: selected structure data are as follows. Formula $C_{44}H_{75}BCl_4N_6Ni_3O_{2.5}$ ($[Ni_3(tmen)_3(\mu_2\text{-}Cl)_3(\mu_3\text{-}OMe)(\mu_3\text{-}OH)](BPh_4)\cdot 0.5MeOH\cdot 0.5CH_2Cl_2$), monoclinic, *C2/c*, a = 23.690(7), b = 19.112(5), c = 22.080(11) Å, β = 96.264(6)°, V = 9937(6) $Å^3$, Z = 8, d_{calcd} = 1.413 g cm^{-3}, μ(MoKα) = 1.383 mm^{-1}, T = 100 K, R_{int} = 0.0468, $R(F)$ ($I > 2\sigma(I)$) = 0.0532, $R_w(F^2)$ (all data) = 0.0891, and a goodness-of-fit indicator of 1.293 for 11360 unique reflections.

Compounds **2** and **3** were prepared according to the methods described elsewhere.[12,13]

Preparation of $[Ni_3(tmen)_3(\mu_2\text{-}Cl)_3(\mu_3\text{-}Cl)(\mu_3\text{-}OH)]Cl$ (2). $NiCl_2\cdot 6H_2O$ (1.188 g, 5.0 mmol) was dissolved in 15 mL dehydrated ethanol, and the mixture was heated at 50°C. To the solution was slowly added tmen (0.74 mL) by syringe, and the solution was stirred for 50 min at room temperature. The solution was concentrated until two thirds of the whole volume. After this concentrated solution was allowed to stand overnight, yellow-green crystals were separated out together with colorless deposition. The crystals were collected on a filter, washed with EtOH, and recrystallized from an 8/2 1,2-dichloroethane/EtOH mixed-solvent. Yellow-green crystals of **2** (772 mg (65%)) were obtained with m.p. 320°C (decomp.). Anal. Calcd.: C, 30.07; H, 6.87; N, 11.69% for $C_{18}H_{49}Cl_5N_6Ni_3O$. Found: C, 30.20 H, 6.73; N, 11.54%.

Preparation of $[Ni_3(tmen)_3(\mu_2\text{-}Br)_3(\mu_3\text{-}Br)(\mu_3\text{-}OH)]Br$ (3). $NiBr_2$ (502 mg, 2.3 mmol) and THF (30 mL) were added to a two-neck round-bottom flask under a nitrogen atmosphere, and the mixture was stirred and boiled for 20 min. The mixture turned bluish-green. An excess amount of tmen (0.7 mL) was added to the solution by syringe. Refluxing for 1.5 h followed by cooling to room temperature gave pale green solids, which were collected on a filter and washed with THF. The resultant green solids were recrystallized from a 1/1 THF/CH_2Cl_2 mixed solvent using a vapor diffusion method with ether. Green solids together with insoluble impurities were deposited, and pale green crystals of **3** (160 mg (22%)) with m.p. 205°C (decomp.) were collected on a filter. Anal. Calcd.: C, 22.97; H, 5.25; N, 8.93% for $C_{18}H_{49}Br_5N_6Ni_3O$. Found: C, 22.87 H, 5.49; N, 8.90%.

Magnetic measurements. The measurement instruments are described in Chapter 1.8. To study the details of the magnetic data in a low temperature region, the measurements were performed in 500 Oe dc field applied. The accuracy of the data in 100 – 300 K was checked by referring the data measured at 5000 Oe. In the measurements of magnetization and susceptibility, the specimens of **1** – **3** were fixed in a small amount of eicosane so that the data on randomly oriented polycrystalline specimens could be acquired. A small amount of eicosane in a holder was melted with a heat gun, and then specimens were added. After being cooled to room temperature, the sample was fixed by solidified eicosane. The cell holders made of gelation and polyethylene film were used. For the magnetic anisotropy study, a green single crystal (2.0×1.0×0.6 mm^3) of **1** was fixed with a small amount of Apiezon H grease. The crystal faces of **1** were characterized with the Miller indices prior to the magnetic study. In the measurement of single-crystal magnetization, the crystallographic principal axis of the single-crystal was made parallel to a magnetic field direction.

2.4 Results

2.4.1 Preparation

The molecular design such as $Ni^{II}_3X_3Y_2$ (Scheme 2.1) contains a counter anion to balance the charge. A sterically bulky BPh_4^- seems to be suitable for this propose. Actually, a novel ionic crystal $[Ni_3(tmen)_3Cl_3(\mu_3\text{-OMe})(\mu_3\text{-OH})]BPh_4$ has been developed. The isolated crystal of **1** involves solvent molecules in the clearance of the ions, as clarified by means of single-crystal X-ray diffraction study (see below) together with elemental analysis.

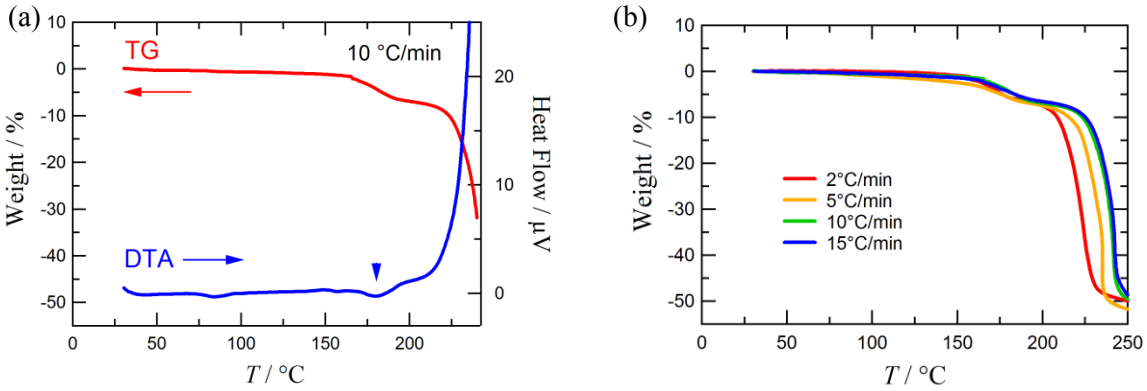

Figure 2.1. (a) Simultaneous TG-DTA measurements of **1**. The specimen was heated from 30 to 250 ºC at a sweep rate of 10 ºC /min. A small triangle indicates an endothermic signal. (b) TG curves of **1** measured at four heating rates from 2 to 15 ºC /min.

The result of the thermogravimetry (TG) and differential thermal analysis (DTA) for **1** is shown in Figure 2.1. A broad endothermic DTA peak of **1** was observed around 160°C, and a concomitant gradual weight loss was recorded in TG by ca. 6%. The strong peaks of DTA and TG indicate the decomposition of specimen of **1** above ca. 220°C. The weight loss percentage around 160°C is significantly close to the calculated value (5.5%) from the desorption of a half MeOH and a half CH_2Cl_2 molecules in the formula of **1**, $[Ni_3(tmen)_3(\mu_2\text{-Cl})_3(\mu_3\text{-OMe})(\mu_3\text{-OH})]$-$(BPh_4)\cdot 0.5MeOH\cdot 0.5CH_2Cl_2$, as determined by means of elemental analysis. The elemental analysis also clarified that the solvent molecules hardly escaped from the crystal during the

present experiments. This finding is supported by the desorption temperature much higher than room temperature. There is no effect on the magnetic measurement.

Two known compounds, **2** and **3**, were also prepared, and their crystal structures were confirmed. The difference of **2** and **3** is the halide ligands such as "belt" parts around the Ni triangle and counter anions (Cl^- and Br^-, respectively). They isomorphously crystallize in the same $P2_12_12_1$ space group. Compound **3** tends to decompose and change color from greenish brown to greenish white in the air, while **2** is relatively stable. The hydrogen bond is present between the cap ligand OH^- and counter anion X^- (Cl^- or Br^-). The crystal packing seems to be tight, so that no lattice solvent molecule is incorporated. These preparations and characterizations well reproduced the previously reported results.[12,13]

2.4.2 Crystal Structures

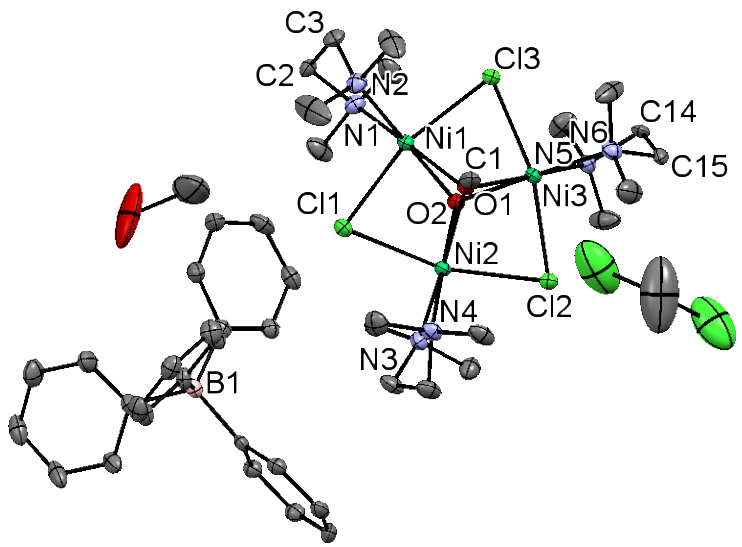

Figure 2.2. ORTEP representation of **1** with selected principal atomic numbering. Thermal ellipsoids are drawn at the 50% level. Only the major conformations are shown except the low-occupancy atoms, C44 – C47. The methanol configuration is assumed to be 1/1 disordered due to the symmetry.

From the X-ray crystal structure of **1**, this formula was determined as

$[Ni_3(tmen)_3(\mu_2\text{-}Cl)_3(\mu_3\text{-}OMe)(\mu_3\text{-}OH)](BPh_4)\cdot 0.5MeOH\cdot 0.5CH_2Cl_2$ (Figure 2.2). The asymmetric unit involves one $[Ni_3(tmen)_3(\mu_2\text{-}Cl)_3(\mu_3\text{-}OMe)(\mu_3\text{-}OH)]^+$ cation, one BPh_4^- anion, a half of methanol and dichloromethane molecules. Three Ni(tmen) moieties and three chloride ions are alternatingly arranged in the "belt" of the $[Ni_3(tmen)_3(\mu_2\text{-}Cl)_3(\mu_3\text{-}OMe)(\mu_3\text{-}OH)]^+$ cation. There are four disordered C atoms as an ethylene conformation isomer in the Ni_3 cation of **1**. The occupancy factors of C2 – C3/C44 – C45 and C14 – C15/C46 – C47 were refined to be 0.662(12)/0.338(12) and 0.728(13)/ 0.272(13), respectively.

Table 2.1. Selected bond lengths (d in Å) and bond angles (θ in °) of **1**.

	d / Å		d / Å		θ / °
Ni1–Cl1	2.4309(11)	Ni2–O2	2.087(2)	Ni1–O1–Ni2	87.95(10)
Ni1–Cl3	2.4407(11)	Ni3–O1	2.149(3)	Ni2–O1–Ni3	87.84(9)
Ni2–Cl1	2.4324(15)	Ni3–O2	2.068(3)	Ni3–O1–Ni1	87.29(10)
Ni2–Cl2	2.4231(15)	Ni1–N1	2.141(3)	Ni1–O2–Ni2	91.42(8)
Ni3–Cl2	2.4344(10)	Ni1–N2	2.160(3)	Ni2–O2–Ni3	91.27(8)
Ni3–Cl3	2.4212(10)	Ni2–N3	2.141(3)	Ni3–O2–Ni1	91.69(9)
Ni1–O1	2.150(3)	Ni2–N4	2.174(3)	Ni1–Cl1–Ni2	75.41(3)
Ni1–O2	2.068(2)	Ni3–N5	2.137(3)	Ni2–Cl2–Ni3	75.39(3)
Ni2–O1	2.133(3)	Ni3–N6	2.179(3)	Ni3–Cl3–Ni1	75.22(4)

Table 2.2. Selected interatomic distances (d in Å) of **1**.[a)]

	d / Å
Ni1···Ni2	2.974(1)
Ni2···Ni3	2.970(1)
Ni3···Ni1	2.967(2)
Cl1···Cl1^{iii}	8.633(5)
Cl2···Cl2^{i}	3.847(2)
Cl3···Cl3^{ii}	3.725(1)

[a)] For the symmetry operation codes, see Figure 2.3.

Each nickel ion of **1** has a distorted octahedral coordination structure with $Cl_2N_2O_2$ donor atoms. The octahedron is elongated toward two chloride bridges (2.43(1) Å for Ni–Cl on the average, Table 2.1) while compressed toward μ_3-OH and μ_3-OCH_3 groups (2.11(4) Å for Ni–O on the average, Table 2.1). Neighboring nickel ions share a Cl_1O_2 face, and the three atoms are presumed to give intramolecular magnetic exchange paths. The triangular Ni plane is capped with a μ_3-OCH_3 group from one pole and a μ_3-OH group from the other. The two μ_3-O atoms form a pseudo-three-fold axis. The Ni^{2+} ions of **1** are formed as an almost equilateral triangle with almost equivalent interatomic Ni···Ni distances of 2.974(1) (Ni1···Ni2), 2.970(1) (Ni2···Ni3), and 2.967(2) Å (Ni3···Ni1) (Table 2.2). The averaged angles of Ni–μ_3-O(H)–Ni and Ni–μ_3-O(CH_3)–Ni are 91.5(2) and 87.7(3)°, respectively. Neighboring Ni^{2+} ions in the Ni_3 core are connected with a μ_2-Cl bridge. The angles of Ni–Cl–Ni are 75.41(3) (Ni1–Cl1–Ni2), 75.39(3) (Ni2–Cl2–Ni3), and 75.22(4)° (Ni3–Cl3–Ni1). As Figure 2.2 and Table 2.1 show, the symmetry of the cation moiety can be regarded as C_{3v}, but the $Ni_3Cl_3O_2$ core is an approximate D_{3h} (a trigonal bipyramid).

The cation portions of **1** are arranged almost parallel, which give a layered molecular arrangement (Figure 2.3). Namely, all the molecular axes of the Ni_3 cation are approximately aligned to the *b* axis direction. As Figures 2.3b and 2.3c display, there are two layers located at *b*/4 and 3*b*/4 in a unit cell. The tilt angles of the Ni_3 molecular plane against the *ac* plane are within ca. 7.1°.

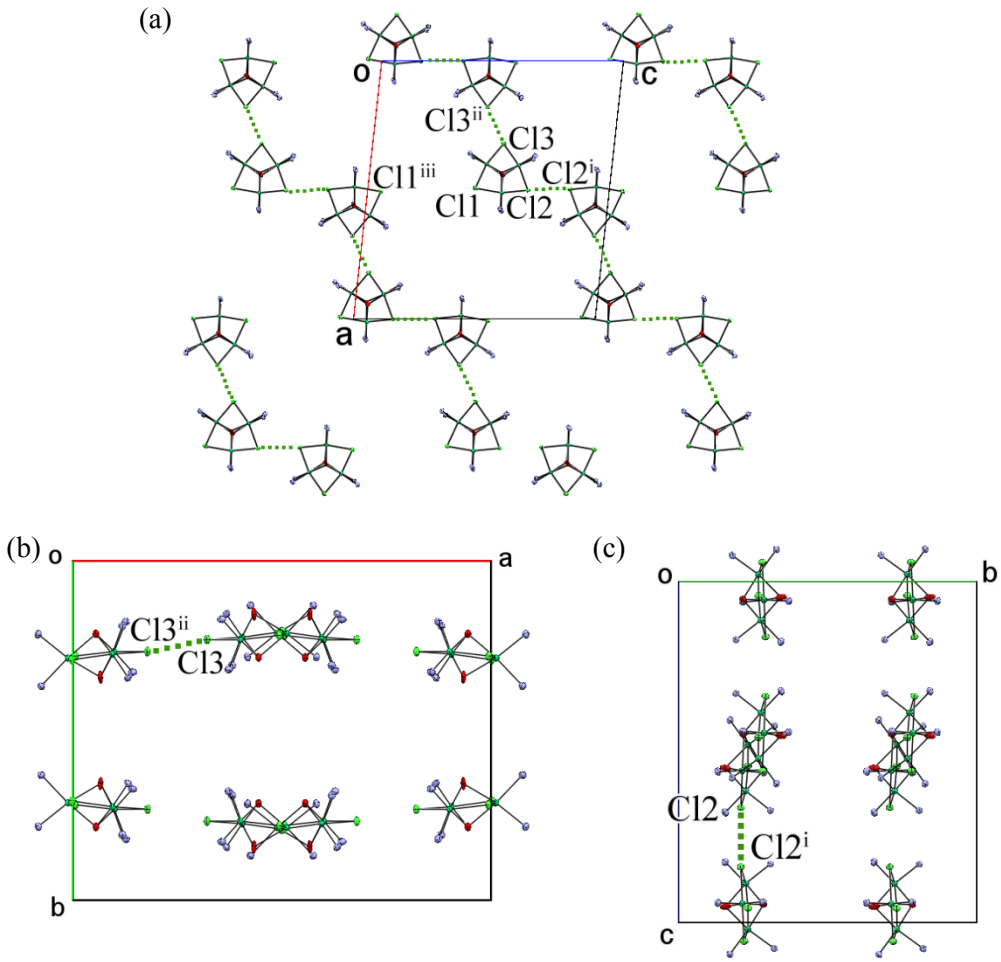

Figure 2.3. Packing diagrams of **1** projected onto (a) the *ac*, (b) the *ab*, and (c) the *bc* planes. An anion, solvent molecules (CH_2Cl_2 and MeOH), and hydrogen atoms are omitted for the sake of clarity. Relatively short intermolecular Cl2···Cl2^{i} and Cl3···Cl3^{ii} contacts are illustrated by broken lines. The symmetry operator codes for ^{i}, ^{ii}, and ^{iii} are (1−*x*, *y*, 3/2−*z*), (1/2−*x*, 1/2−*y*, 1−*z*), and (1−*x*, *y*, 1/2−*z*), respectively.

Table 2.2 summarizes the neighboring interatomic distances. The neighboring intermolecular distances (Cl2···Cl2^{i} and Cl3···Cl3^{ii}) in the crystal of **1** are 3.847(2) and 3.725(1) Å, which are close to the sum of the van der Waals radii[15] (3.50 Å) and that of the ionic radii[16] (3.62 Å). The symmetry operation codes for ^{i} and ^{ii} are (1−*x*, *y*, 3/2−*z*) and (1/2−*x*, 1/2−*y*, 1−*z*), respectively. These intermolecular geometries alternatingly repeat in the *a* + *c* diagonal direction. On the other hand, the third nearest neighboring intermolecular distances (Cl1···Cl1^{iii}) in the crystal is found

within a layer (the symmetry operation code for ^{iii} is (1−*x*, *y*, 1/2−*z*)). This distance is 8.633(5) Å and over twice as long as those of the first (Cl2···Cl2^{i}) and second (Cl3···Cl3^{ii}) intermolecular distances. Furthermore, because the interlayer distance is also relatively long (*b*/2 = 9.56 Å), the molecular arrangement of **1** can be regarded as a one-dimensional (1D) chain along the *a* + *c* direction (Figure 2.4). The quasi 1D chain seems to recuse the exchange path through the interstitial counter ion and solvent molecules. The halogen···halogen short distances, (Cl2···Cl2^{i}) and (Cl3···Cl3^{ii}) will provide intermolecular exchange paths, and accordingly the present crystal structure allows the magnetic analysis based on a quasi 1D model.

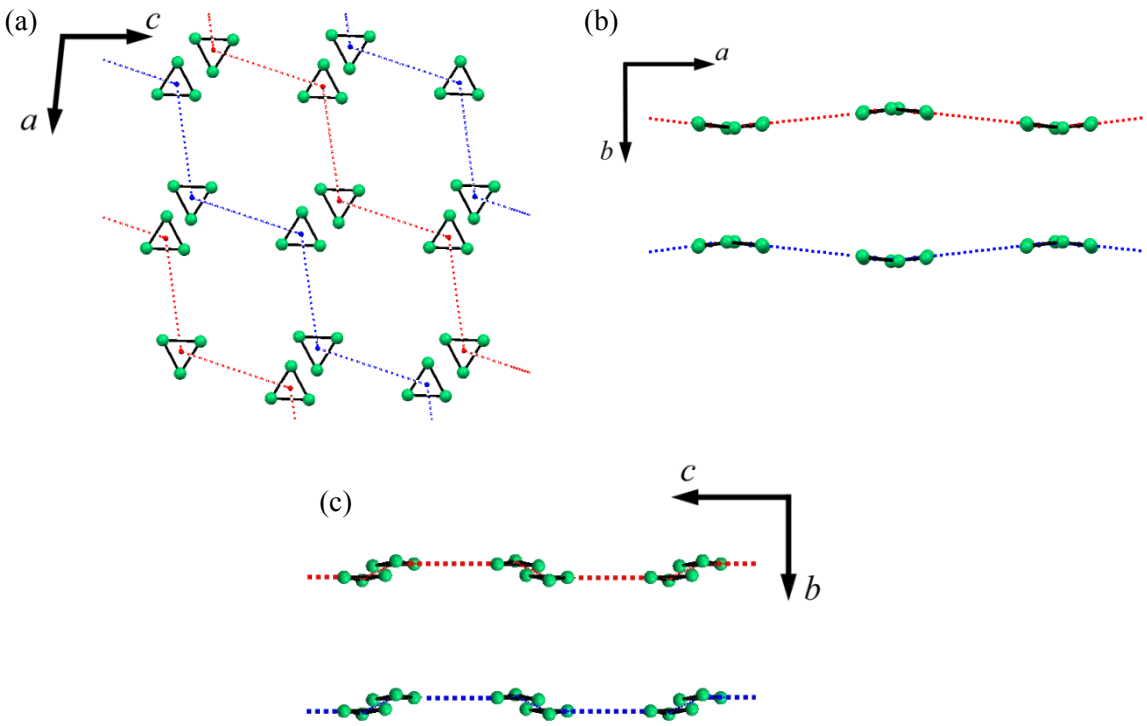

Figure 2.4. Packing diagrams of **1** projected onto (a) the *ac*, (b) the *ab*, and (c) the *bc* planes. Triangles denote the Ni trinuclear molecules. Dotted lines imply possible intermolecular interaction through relatively short Cl···Cl distances, which form one-dimensional (1D) chains in the *a* + *c* direction. Red and blue chains are symmetry-related arranged at different levels (*b*/4 and 3*b*/4).

2.4 Results

As shown in Scheme 2.1, the molecule of **1** has two O caps (–OH and $–OCH_3$ groups), while **2** and **3** have the caps of an O atom and a halogen atom (Cl for **2** and Br for **3**). The averaged intramolecular Ni···Ni distance of **1** is the shortest (2.970(4) Å on the average) of these compounds; those of **2** and **3** are 3.04[12] and 3.13 Å,[13] respectively. Compounds **2** and **3** crystallize in an orthorhombic $P2_12_12_1$ space group (Figure 2.5). The molecular axis direction seems to be important, because it coincides with the direction of uniaxial magnetic anisotropy. Although the arrangement of the Ni_3 cation of **2** and **3** is different from that of **1**, these Ni_3 molecular structures are similar to each other. There are four molecular axis directions in a unit cell of **2** and **3**, and each molecular axis tilts each other. Estimation of the magnetic anisotropy seems to be difficult for **2** and **3**. Therefore, the molecular arrangement of **1** (Figure 2.3) is concluded to be unique and suitable for the detailed study of magnetic anisotropy and exchange couplings. Relatively short intermolecular Cl···Cl and Br···Br distances are found; the shortest one is assigned between the "belt" halogen atoms (4.232(8) Å for **2** and 4.158(3) Å for **3**) and the second one between the "belt" and cap halogen atoms (4.667(7) Å for **2** and 4.339(2) Å for **3**). The former constructs a 1D chain, and the latter weakly connects the chains. The interchain connection gives rise to a three-dimensional network (Figure 2.5), which may be responsible for the bulk magnetic property.

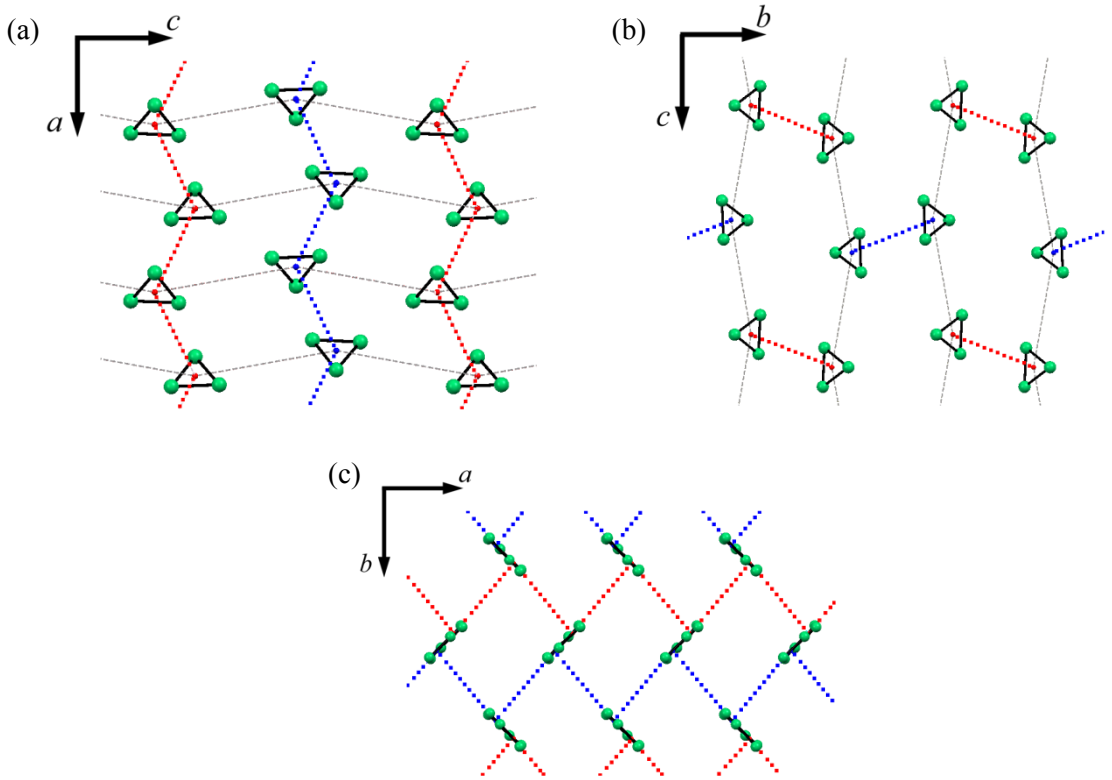

Figure 2.5. Packing diagrams of **3**[13] projected onto (a) the *ac*, (b) the *bc*, and (c) the *ab* planes. Triangles denote the Ni trinuclear molecules. Dotted lines imply possible intermolecular interaction through relatively short Br···Br distances, which form a three-dimensional network. Red and blue dotted lines denote strong interaction, and gray dotted lines denote weak interaction. The packing diagrams of **2**[12] are quite similar to that of **3** at only difference of the halogen atom.

2.4.3 Magnetic Properties

The dc magnetic susceptometry of polycrystalline specimens of **1** – **3** were performed, in which the randomly oriented samples were fixed with eicosane (Figure 2.6). The detailed measurement conditions are described in Chapter 1, Section 1.8. The $\chi_m T$ values at 300 K were 4.37, 4.12, and 4.19 cm^3 K mol^{-1} for **1**, **2**, and **3**, respectively, which are larger than the expected value 3.0 cm^3 K mol^{-1} from the spin-only values of the sum of three independent paramagnetic Ni^{2+} ions ($3d^8$, $S_{Ni} = 1$, $g = 2$). These large $\chi_m T$ values at 300 K can be mostly explained by the larger g values. The $\chi_m T$ is proportional to g^2, and $\chi_m T = 4$ cm^3 K mol^{-1} is expected from $g = 2.3$.

On cooling down to 20 K, the $\chi_m T$ values of **1** – **3** increased to the maximum ($\chi_m T$ = 6.64 cm^3 K mol^{-1} at 18 K, 6.48 cm^3 K mol^{-1} at 26 K, and 6.49 cm^3 K mol^{-1} at 20 K, respectively), indicating the presence of considerably strong intramolecular ferromagnetic interaction. Below 20 K, the $\chi_m T$ values of **1** – **3** decreased owing to intermolecular interaction and/or zero-field-splitting (ZFS) effect.

The intramolecular exchange parameters (J's) of **1** – **3** were estimated. The three J's are assumed to be unique in each molecule because the three Ni centers form an approximate triangle with three-fold symmetry. Based on the spin-Hamiltonian (Eq. 1.13 in Chapter 1), the van Vleck equation (Eq. 1.16 in Chapter 1)[17] was derived.

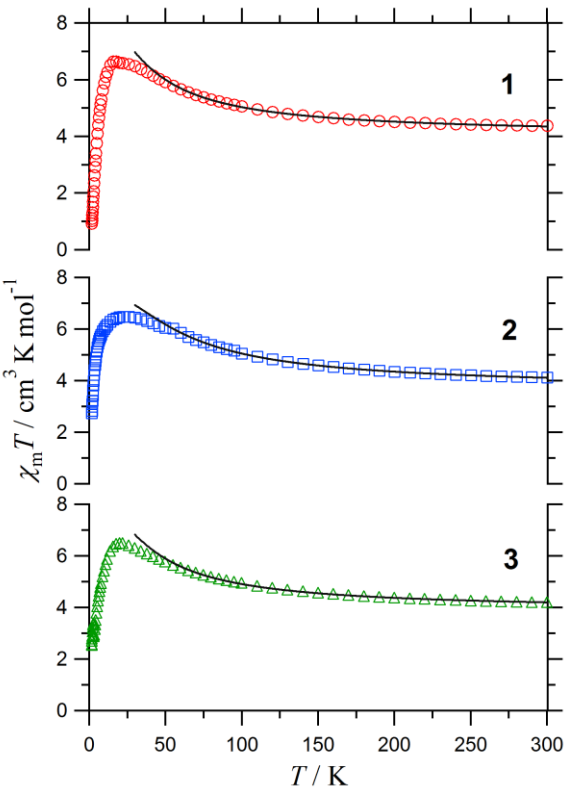

Figure 2.6. Temperature dependence of $\chi_m T$ for **1** – **3** measured. In the temperature range from 1.8 to 100 K, they were measured at 500 Oe. While the ranging from 100 to 300 K, at 5000 Oe. The solid lines represent calculated curves. For the parameters, see the text.

The solid lines in Figure 2.6 represent the best fit to Eq. 1.16 in a temperature range from ca. 60 to 300 K for **1** – **3**. The optimized parameters were $2J/k_B$ = 18.0±0.2, 27.2±0.2, and 19.6±0.2 K with g = 2.32±0.01, 2.21±0.01, and 2.27±0.01 for **1**, **2**, and **3**, respectively. The g value of **1** is close to that of the preliminary high-frequency electron paramagnetic resonance (HF-EPR) measurements (Figure 2.7). The ν-intercept of the red line gave determination of the D value, which was deduced to $D_{S=3}/k_B$ = −2.2±0.1 K. The negative sign of $D_{S=3}$ from the relative signal intensity were determined. Figure 2.7b shows the temperature dependence of HF-EPR spectra at 360 GHz on a powder specimen of **1**. When the strong signal intensity was observed at a low-field region, the signal intensity was reduced on elevating temperature. This phenomenon means that the signal originates in the transition from the ground spin state. For details of the analysis method, see ref 11.

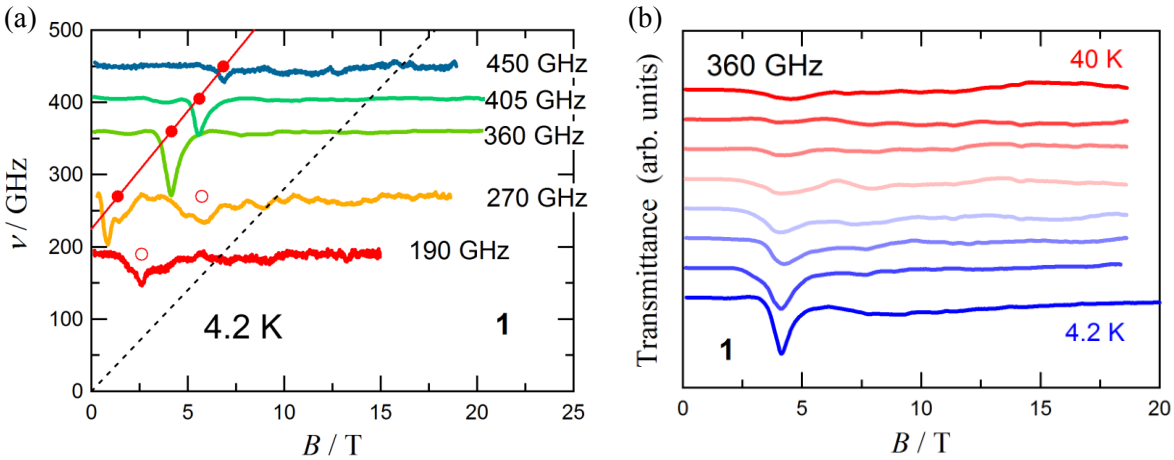

Figure 2.7. (a) Selected HF-EPR spectra on a powder specimen of **1**. The spectra are offset in proportion to the frequency. A broken line is shown in a g = 2 line. The g value g_z = 2.33±0.04 from the slope of the red line. (b) Temperature dependence of HF-EPR spectra at 360 GHz on a powder specimen of **1**.

The unique molecular arrangement of **1** (Figure 2.3) enables us to determine the magnetic anisotropy. The results of the magnetization measurements on a single crystal and a powder

specimen of **1** are summarized in Figure 2.8, measured in a magnetic field range 0 – 7 T at 1.8 K. The plot displays the data with the magnetic fields applied parallel to the *a*, *b*, and *c* axes. The averaged magnetization data over the three directions was closely to the powder data. The present results revealed that the *b* axis is located parallel to a magnetic easy axis. From Figure 2.3, the *b* axis corresponds to the molecular symmetry axis. Consequently, it is reasonably accepted that the magnetic moment would arise perpendicular against the Ni_3 triangle in each molecule. On the other hand, the magnetizations along the *a* and *c* axes linearly increased with respect to the applied field. This behavior is typical of hard-axis magnetization process in uniaxial magnetic systems, which the nearly coincident data of the *a* and *c* axes were regarded as hard-plane data. The crossing point between the easy-axis and hard-plane data was formed as the maximum coercive field. An extrapolation gave 8.35 T, it should be noted that that a metamagnetic-like jump occurred at ca. 1.2 T in the data of *H*//*b* and also in powder. They were conjectured that this jump would be caused by a weak intermolecular interaction acting between neighboring molecules. This point is discussed later.

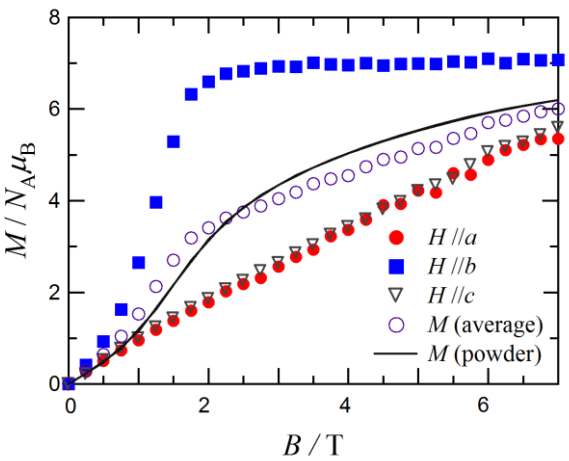

Figure 2.8. Single-crystal magnetization data for **1** measured at 1.8 K.

As **2** and **3** are isomorphous, the magnetization curves of **2** and **3** basically showed a similar

behavior (Figure 2.9). However, the magnetization of **3** measured at 1.8 K showed a sigmoid curve such as metamagnetic behavior with a broad inflection around 1 – 2 T, while **2** only displayed a typical monotonic magnetization curve under the same conditions. This finding indicates that **3** has stronger anisotropy and/or intermolecular interaction than **2**.

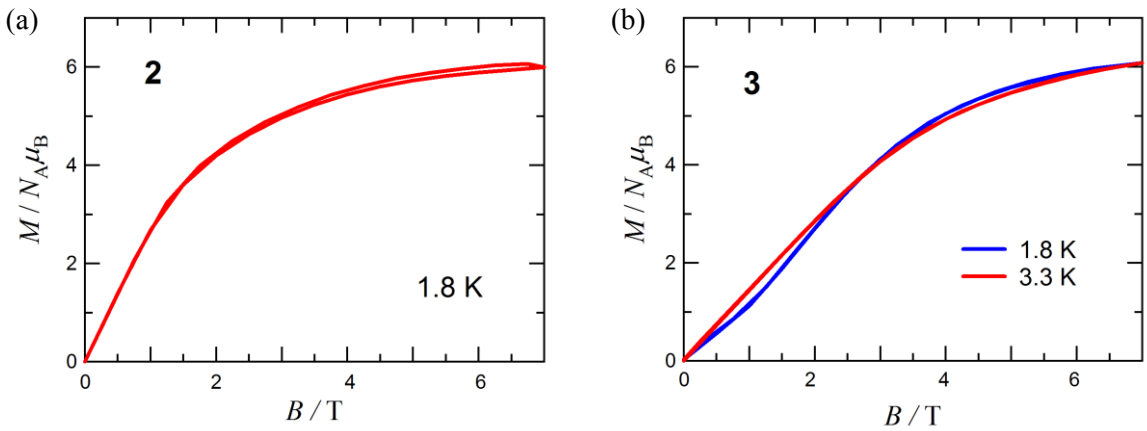

Figure 2.9. Magnetization curves for (a) **2** and (b) **3**.

Now let us evaluate an activation energy for the magnetization reorientation and a zero-field-splitting parameter D[18] for **1**. As for a magnetic single domain such as SMMs, a magnetization process involves only a magnetization reversal.[19] The orientation of the magnetic moment of the particle can be described as the sum of its uniaxial and the Zeeman energies (Eq. 2.1).

$$E = -K_u V \cos^2(\theta - \theta_0) - M_s V H \cos\theta, \tag{2.1}$$

where K_u is an anisotropy energy, V is the volume per unit, M_s is the saturation magnetization, θ is the angle between the easy axis and the field, and θ_0 is the angle between the easy axis and the saturation magnetization. These angles are shown in Scheme 2.2.

Scheme 2.2. Angles of θ and θ_0 associated with the direction of the magnetic easy axis, the saturation magnetization, and the field.

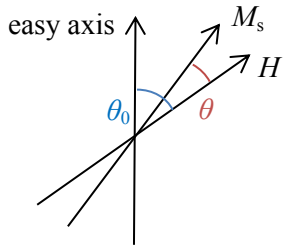

Taking the partial derivative of Eq. 2.1 with respect to θ, Eq. 2.2 was derived as:

$$\frac{\partial E}{\partial \theta} = 2K_u \cos(\theta - \theta_0)\sin(\theta - \theta_0) + M_s H \sin\theta . \tag{2.2}$$

When Eq. 2.2 has the minimum energy, it is zero. Then $\theta_0 = 90°$ value is substituted into Eq. 2.2, $\cos\theta = M_s H/2K_u$ was obtained. The activation energy is given by $\Delta = K_u V$. The anisotropy energy is related to an anisotropy field H_a by the expression $H_a = 2K_u/M_s$.[20] The anisotropy field coincides with the maximum coercive field.

From Figure 2.8, $\mu_0 H_a$ and M_s were found to be 8.35 T and 6.82 μ_B, respectively. The anisotropy energy was estimated as K_u/k_B = 19 K from the above values. On the other hand, the anisotropy energy is expressed by Néel-Arrhenius theory[21] (Eq. 2.3) where τ is a relaxation time and τ_0 a pre-exponential factor.

$$\tau = \tau_0 \exp\left(\frac{K_u V}{k_B T}\right) = \tau_0 \exp\left(\frac{\Delta}{k_B T}\right) \tag{2.3}$$

An activation energy Δ causes a magnetization dynamics, as regulated with $\Delta = |D|S^2$.[1] Using the activation energy Δ/k_B = 19 K and the molecular total spin S = 3, the ZFS parameter was

estimated as $D_{S=3}/k_B$ = −2.1 K. The negative sign was chosen from the uniaxial magnetic anisotropy and the results of the HF-EPR measurements on **1** (Figure 2.7). The anisotropy energy is also related to the slope of the hard plane data as expressed with Eq. 2.4. From the slope of this equation K_u/k_B = 20 K was obtained, thus leading to $D_{S=3}/k_B$ = −2.2 K. By taking average of these two values, $D_{S=3}/k_B$ = −2.2±0.1 K is determined for the Ni_3 cation of **1**. The present $D_{S=3}$ value is close to that of the HF-EPR results (Figure 2.7).

$$\frac{M}{M_S} = \frac{M_S}{2K_u} H \tag{2.4}$$

The pulsed-field magnetization curve for **1** measured at 0.5 K is shown in Figure 2.10. A major magnetization jump was recorded at 1.2 T besides minor steps between 2.0 and 3.3 T, measured with a sweep rate of 6.3 T/ms. The major jump coincides with that found in the magnetization curve by SQUID results (Figure 2.8). The additional minor jumps are possibly caused by the enhancement of the relaxation at the level crossing of the SMM energy state.[11] In fact, the intensities and the positions of the minor jumps are sensitive to the sweep velocity of pulsed magnetic fields.

The molecular arrangement of **1** shows a quasi 1D structure due to the interatomic interaction via Cl···Cl contacts. The major jump may be ascribed to the reorientation of the antiferromagnetically coupled S = 3 spins in a quasi 1D chain. These interatomic interactions would trigger an exchange bias prohibiting tunneling at zero magnetic field; namely, the presence of exchange bias leads to remnant magnetization. For examples,[22] $[Ni(hmp)(MeOH)Cl]_4 \cdot H_2O$ and $[Ni(hmp)(EtOH)Cl]_4 \cdot H_2O$ (hmpH = 2-(hydroxymethyl)pyridine) have a pseudo three-fold axis symmetry. The magnetization curves at 0.04 K of these compounds show some jumps and the remnant magnetization due to intermolecular interaction through Cl···Cl contact.[22] These first

jump seems to record at ca. 0.3 T, at which are smaller than the jump of **1** at 1.2 T. To investigate the nature of the relaxation, the ac magnetic susceptibilities were measured at zero field and at certain dc bias field inside a hysteresis loop.

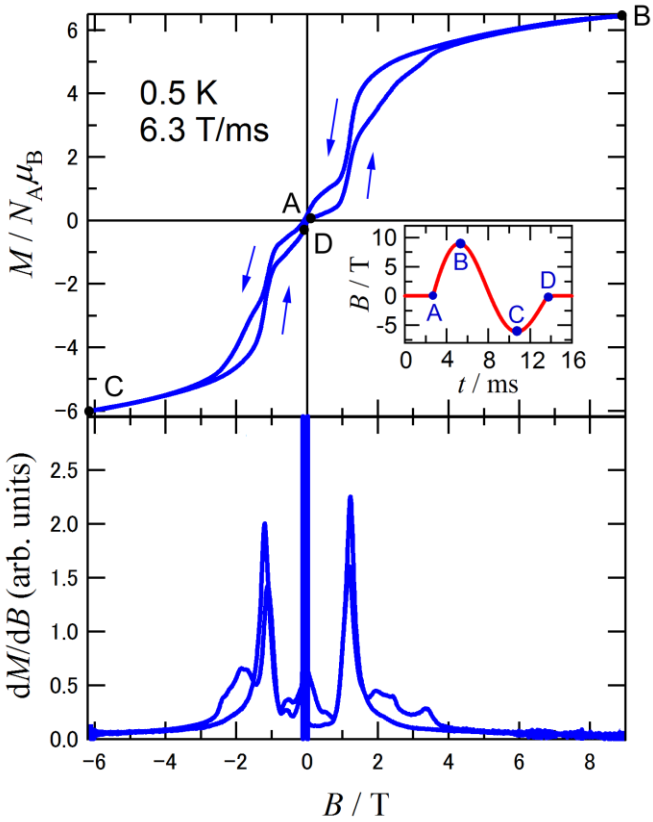

Figure 2.10. (Top) Pulsed-field magnetization curve and (Bottom) differential of magnetization for **1** measured at 0.5 K. The inset shows a field-scan sequence as a function of time.

The ac susceptibilities of **1** are plotted as a function of temperature and ac frequency (Figure 2.11). These data were recorded at applied magnetic fields (H_{dc}) of 0, 10, and 15 kOe in 1.9 – 20 K. The latter field was chosen for cancelling the intermolecular antiferromagnetic coupling. The temperature dependence of out-of-phase (χ") signals was observed in a low temperature region. At 15 kOe, the SMM is aligned to the field direction, and the relaxation of the SMM can be observed without the influence of weak antiferromagnetic coupling, as indicated with their

sharper upsurge of χ' in (c) than in (a).

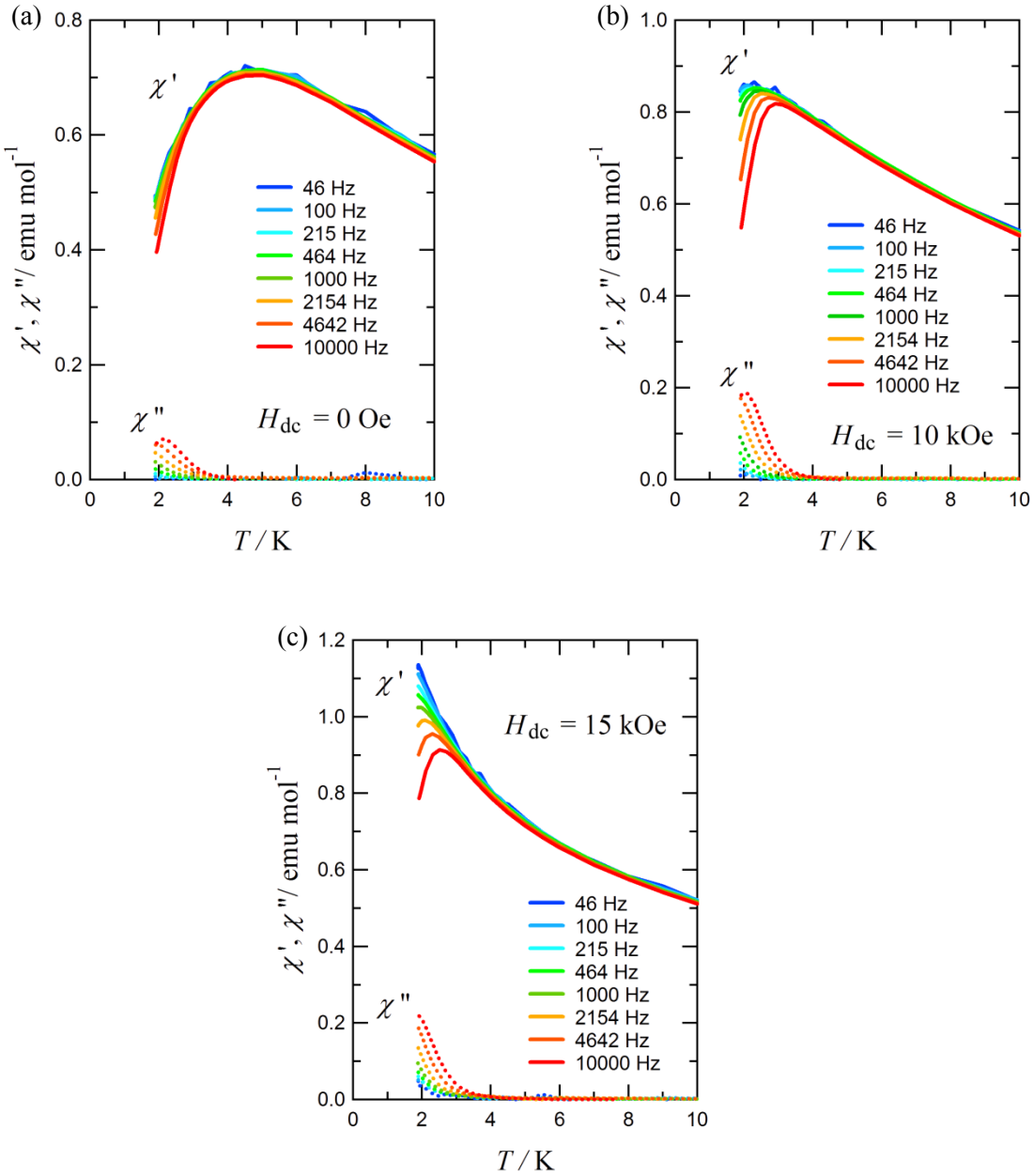

Figure 2.11. Ac susceptibilities for **1** measured (a) at zero dc bias field, (b) at the dc bias field of 10 kOe, and (c) at the dc bias field 15 kOe. χ' and χ'' represent the in-phase and out-of-phase components, respectively.

One may notice that the onset of the χ'' is nearly the same between the data sets recorded

under two conditions. It indicates that the origin of the present relaxation is common. Figure 2.12 shows the modified Arrhenius plots[23] for **1** based on Eq. 2.5 from the ac susceptibility data (Figure 2.11). Selected four high frequency and region low temperature, the plots displayed, which the calculation was estimated with all plotted data. The plot shows non-linear temperature dependence.

$$\ln(\chi''/\chi') = \ln(2\pi\nu\tau_0) + U_{\mathrm{eff}}/k_{\mathrm{B}}T \tag{2.5}$$

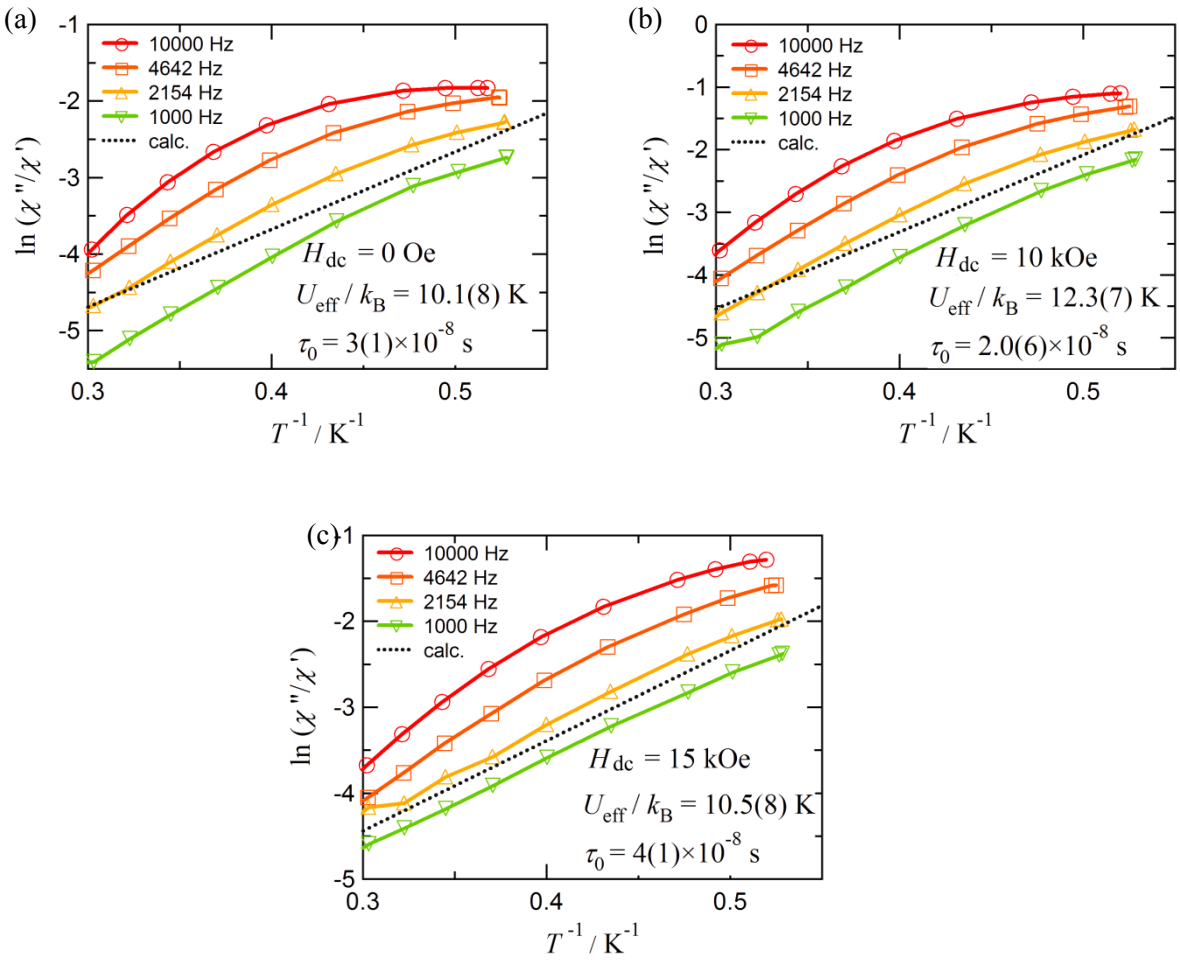

Figure 2.12. Modified Arrhenius plots[23] for **1** (a) without, (b) with the dc bias field of 10 kOe, and (c) with the dc bias field of 15 kOe. Dotted lines imply the calculation using the four frequency data. Solid lines are drawn for a guide to the eye.

The effective energy barriers U_{eff} of the magnetization reversal and pre-exponential factors τ_0 for **1** were obtained to be U_{eff}/k_B = 10.1±0.8, 12.3±0.7, and 10.5±0.8 K and τ_0 = (3±1)×10^{-8}, (2.0±0.6)×10^{-8}, and (4±1)×10^{-8} s without, with H_{dc} = 10 kOe and with H_{dc} = 15 kOe, respectively. The barrier is almost unchanged among the three, and the values are not far from the estimated barrier caused by the uniaxial anisotropy. The dominant origin of the observed relaxation can be concluded to be the activation energy from the uniaxial magnetic anisotropy of **1** as a SMM. The experimental activation energy barrier is smaller than that of the calculation (Δ/k_B = 19 K), probably because of the presence of longitudinal magnetization due to the molecular axis tilted by ca. 7.1° against the ac plane.

2.5 Discussion

The topics of ferromagnetic exchange paths are discussed in this section. Compounds **1** – **3** were found to possess intramolecular ferromagnetic coupling, configuring the ground S = 3 molecules. As noted in Chapter 1, Section 1.4, according to the Anderson-Goodenough-Kanamori rule,[24] ferromagnetic coupling is larger when a Ni–O–Ni angle approaches 90° (superexchange mechanisms). The angle Ni–O–Ni in the range 90±14° is proposed to favor ferromagnetic coupling.[25a] The principal pathway of ferromagnetic coupling in **1** – **3** is considered to be via the μ_3-O atom. "Cubane"-type Ni_3O_3 compounds have been well known[25] to show ground high-spin states based on superexchange interactions across the μ_3-oxido bridges.[25] For example, the relationship between Ni–O–Ni angles and exchange parameters (J's) has intensively been studied.[25k] The averaged Ni–O–Ni angles are 90±0.2, 97±1, and 100±1° for **1**, **2**, and **3**, respectively, and the present μ_3-O capped structures seem to be suitable for ferromagnetic interaction.

Another exchange interaction is supposed to occur via the μ_2-halogen atom on the "belt". The averaged Ni–X–Ni angles are 75.3±0.1, 77.3±0.2, and 75.5±0.2° for **1**, **2**, and **3**, respectively. The

ferromagnetic exchange couplings though Ni–X–Ni have been reported,[26] and the relation between J and the Ni–X–Ni angle indicates that the larger J values are derived from the smaller angles in the angular range of ca. 93 – 107°.[26] Although the bridging halogen atoms are different in **2** and **3**, the ferromagnetic trends in Ni–Cl–Ni and Ni–Br–Ni are similar.[26b] It is difficult to predict exactly J values from the relation plots proposed. The Ni–X distances are basically longer than the Ni–O distances. The J value is insensitive to the bridging X atoms. These findings suggest that the role of the Ni–μ_2-X–Ni path would be minor for the ferromagnetic coupling observed here.

The parameters g and J were determined from the high-temperature data, and the low-temperature-limit values $\chi_m T$ = 8.1, 7.3, and 7.7 cm^3 K mol^{-1} are expected from g = 2.32, 2.21, and 2.27 for **1**, **2**, and **3**, respectively. Paying attention only to the intramolecular origin, the $\chi_m T$ reductions recorded around, and below the $\chi_m T$ peaking temperature can be mostly understood in terms of the ZFS effect. Even after J and $D_{S=3}$ were included in the magnetic analysis; however, the experimental data for **1** were still dislocated downward from the calculation. Contribution of intermolecular antiferromagnetic interactions seems to be important to interpret the further reduction of the experimental χ_m. It is rationalized from the small magnetization in a field region within ±1.2 T for **1** (Figures 2.8 and 2.10), which is related to the 1D structure through the intermolecular van der Waals halogen contacts (Figure 2.3).

The intermolecular interaction in the crystal of **1** takes place through the halogen···halogen contacts between neighboring Cl atoms from adjacent complex ions (3.847(2) and 3.725(1) Å), as clarified in the crystallographic analysis (Figure 2.3). The Ni_3 molecules behave as an S = 3 species in such a low temperature region, and, to simplify a model, a Ni_3 molecule is assumed as an S = 3 center with the ZFS constants $D_{S=3}$ (−2.2 K) and null $E_{S=3}$. Furthermore, the chain is supposed to be uniform. Simulation according to the spin-Hamiltonian of Eq. 2.6 will lead to quantify the intermolecular coupling constant j. Here, each i-th and k-th site has an S = 3 center.

$$\hat{H} = \hat{H}_{\mathrm{EX}} + \hat{H}_{\mathrm{ZFS}} = -2\sum_{i<k} j\hat{S}_i \cdot \hat{S}_k + \sum_i D_{S=3}(\hat{S}_i^z)^2 . \tag{2.6}$$

The chain is infinite, and accordingly finite oligomer models should be introduced to satisfy a cyclic boundary condition. Owing to the computational cost, n = 1, 2, 3, 4, and 5 n-mer (oligomer) model calculations of the S = 3 species were performed in the MAGPACK software[27] (Figure 2.13). The simulation curves were drawn so that the experimental data appeared between the calculated curves of the tetramer (4-mer) and pentamer (5-mer) models. Eventually, the parameter $2j/k_B$ was estimated to be −0.14±0.01 K for **1**. The errors of the parameters $2j/k_B$ were estimated to be ±0.01 K from several simulation works.

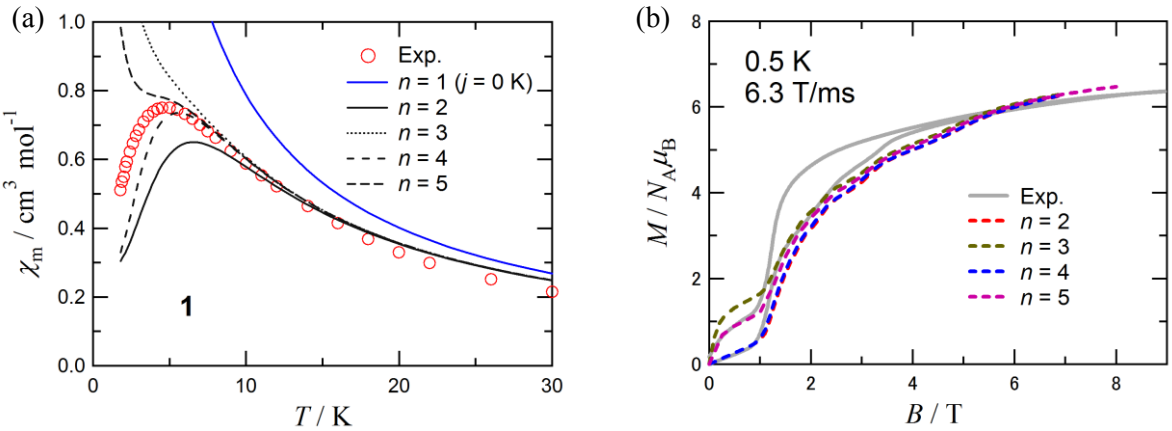

Figure 2.13. (a) Experimental and calculated χ_m for **1** at a dc field of 500 Oe. The lines represent simulations of cyclic oligomer (n-mer) models of S = 3 centers with $D_{S=3}/k_B$ = −2.2 K, $2j/k_B$ = –0.14 K, and g = 2.32. (b) Experimental and calculated magnetization curves for **1** at 0.5 K. Dashed lines represent simulation curves on cyclic n-mer models of S = 3 centers. The parameters are the same as those of (a).

As Figure 2.13a shows, the χ_m value of the experimental data around 50 K fell below the calculation data because of the thermal depopulation of the S = 3 state. At lower temperatures, the simulation curves better reproduced the experimental data. The magnetization curve of **1** at 0.5 K was also calculated with the same magnetic parameters by using MAGPACK (Figure 2.13b). The

field position of the magnetization jump was calculated to be 1.4 T. The experimental critical field was 1.2 T (Figure 2.10). Although the finite models were utilized, the two fields are considerably close to each other. This finding supports that the estimated j value is reliable and furthermore affords complete comprehension of the metamagnetic-like behavior.

Similarly, the j and $D_{S=3}$ values of **2** and **3** could be estimated by simulation using MAGPACK (Figure 2.14). Note that we could not determine the $D_{S=3}$ values from the magnetization measurements of single crystal specimens. Thus, after determination of $D_{S=3}$ was skipped, the j values were firstly calculated by the simulation of the magnetization curves. The j value is related with the jump position of the pulsed-*MH* curve like Figure 2.13b. Actually, they derived $2j/k_B = -0.06$ K from the jump position 0.5 T for **2** and $2j/k_B = -0.15$ K from 1.4 T for **3** (Figure 2.15).

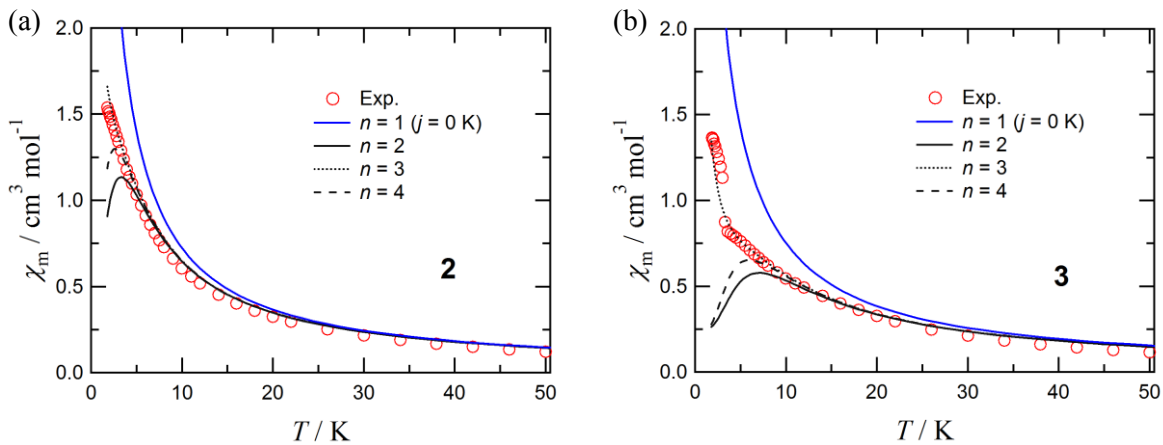

Figure 2.14. Experimental and calculated χ_m for (a) **2** and (b) **3** at a dc field of 500 Oe. The lines represent simulations of cyclic oligomer (n-mer) models of $S = 3$ centers with $D_{S=3}/k_B = -1.6$ and -2.4 K, $2j/k_B = -0.06$ and -0.15 K, and $g = 2.21$ and 2.27 for **2** and **3**, respectively.

By using these j's, the $D_{S=3}$ values of **2** and **3** were estimated from a simulation of the χ_m vs. T curves of an $S = 3$ species (Figure 2.14). Namely, only the $D_{S=3}$ value was variable, while the g, $2j$, and $E_{S=3}$ (=0) were frozen, and the simulation curves were drawn so that the experimental data

were located between the calculated curves of the trimer and tetramer models. The parameters were optimized $D_{S=3}/k_B = -1.6$ and -2.4 K for **2** and **3**, respectively. The errors were estimated to be ±0.2 K from several simulation works. Table 2.3 summarizes the results of the magnetic parameters on **1** – **3**. It should be noted that there is a sharp increase of χ_m in **3** at around 3 K. As shown later, this anomaly is related to the three-dimensional magnetic ordering.

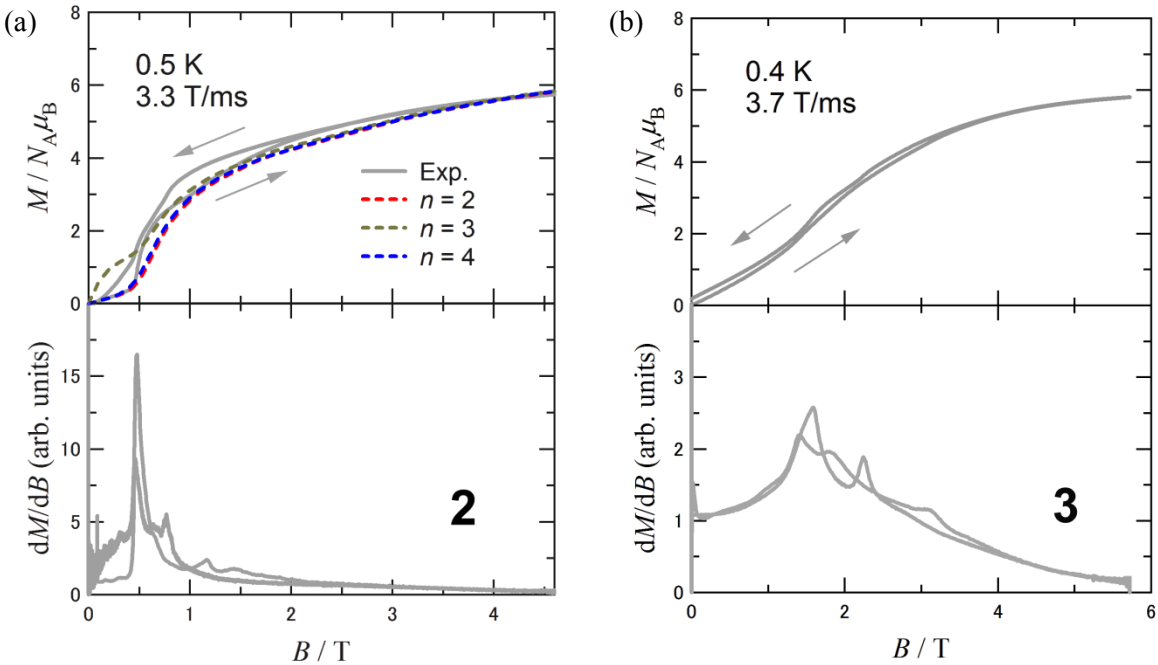

Figure 2.15. (Top) Pulsed-field magnetization curve and (Bottom) differential of magnetization for (a) **2** and (b) **3**, measured at 0.5 and 0.4 K, respectively. In (a, top), calculated magnetization curves (dashed lines) for **2** are superposed. The parameters are the same as those of Figure 2.14.

One may wonder if there would be any relationship between the molecular structure and magnetic anisotropy. From the comparison among the two $Ni_3Cl_3O_2$ clusters investigated here, the strong magnetic anisotropy may be related to the smaller Ni–O–Ni angles; namely, $D_{S=3}/k_B = -2.2\pm0.1$ K was found in the complex with the Ni–O–Ni angle of 90±2° while $D_{S=3}/k_B = -1.6\pm0.2$ K for the complex with 97±1° (compounds **1** and **2**, respectively). Unfortunately, there are too small numbers of the examples to discuss any further. The capping oxygen atoms may play an

important role both in the superexchange coupling and in the magnetic anisotropy.

There have been several reports which describe the linked SMMs having intermolecular interactions.[28] Linked SMMs would prohibit the zero-field tunneling by the exchange and/or dipolar bias, possibly improving magnetic coercivity.[29] The frequency dependence of the ac susceptibilities of **1** (Figure 2.11) reveals that the molecule has a magnetization reversal barrier. Compound **1** has been proven as a potential SMM. From the previous studies,[11] the three analogous Ni triangular compounds were SMMs showing hysteresis loops in the pulsed-field magnetization measurements at 0.5 K. As seen in Figure 2.10, the intermolecular antiferromagnetic interaction was appreciable in **1**, the ground state magnetization was almost lost, and the pure SMM character was hidden. The Arrhenius behavior may be related to the remaining trace of SMM dynamics and become obvious during the magnetization jump.

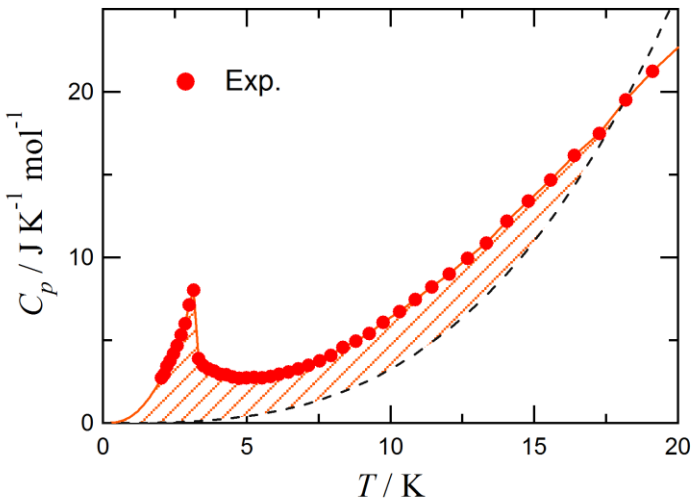

Figure 2.16. Low temperature heat capacity of **3** in zero magnetic field.

The author has to make a comment on a χ_m jump at 3.2 K observed for **3**. The SQUID measurements of **3** revealed that the magnetization curve measured at 1.8 K showed a sigmoid while only a monotonic curve was recorded at 3.3 K (Figure 2.9b). Preliminary heat capacity measurements on **3** clarified the bulk magnetic phase transition at 3.2 K by relaxation method

(Figure 2.16). An orange line at low-temperature region (0 – 2 K) indicates an extrapolation. The entropy change of the phase transition $\Delta_{trs}S$ was estimated as 7.9 J K^{-1} mol^{-1}. The value is smaller than a theoretical value 16.2 J K^{-1} mol^{-1} by a magnetic contribution of Rln 7, which is the thermal excitation of electrons in a molecule from an antiferromagnetic state to a paramagnetic state in the S = 3 species. As discussed in the section of the crystal structure, the magnetic network of **3** shows the three dimensionality (Figure 2.5), which is responsible for the phase transition. Namely, there are antiferromagnetic "super-superexchanges"[30] through the Ni–X···X–Ni paths (as opposed to the Ni–X–Ni superexchange paths). This mechanism mostly brings about antiferromagnetic interaction,[30] but the intermolecular ferromagnetic coupling would attract much more attention to the materials researchers.

Many reports described that the Br···Br intermolecular superexchange is stronger than that of Cl···Cl.[31] In the present case the Cl···Cl distance in **2** is 17% longer than the sum of the ionic radii of Cl^- (3.62 Å), whilst the Br···Br distance in **3** is only 6% longer than the sum of the ionic radii of Br^- (3.92 Å).[16] In fact, the intermolecular coupling of **3** ($2j/k_B$ = –0.15±0.01 K) was stronger than that of **2** (–0.06±0.01 K). Thus, it is rationally acceptable that **3** underwent the magnetic phase transition at 3.2 K but that **2** did not above 1.8 K.

Table 2.3. Magnetic parameters g, $2J$, $D_{S=3}$, and $2j$ for **1** – **3**.

Compounds	**1**	**2**	**3**
g	2.32±0.01	2.21±0.01	2.27±0.01
$2Jk_B^{-1}$/K	18.0±0.2	27.2±0.2	19.6±0.2
$D_{S=3}k_B^{-1}$/K	−2.2±0.1	−1.6±0.2	−2.4±0.2
$2jk_B^{-1}$/K	–0.14±0.01	–0.06±0.01	–0.15±0.01

2.6 Conclusion

To realize (1) ground high-spin states and (2) strong anisotropy, novel trinuclear **1** with two μ_3-O caps has prepared, and two known compounds **2** and **3** also were prepared. These purposes have successfully assessed by the structures and magnetic properties. It should be noted that the $D_{S=3}$ value (–2.2±0.1 K) of **1** was larger than that of the previous work[11] ($D_{S=3}/k_B$ = (−1.67) – (−1.90) K). The Ni_3 complex cations of **1** are linearly arranged in a crystal lattice. The Cl atoms at the "belt" in the complex cations are located close to each other, and the resultant Cl···Cl contacts lead to sizable intermolecular exchange coupling between the neighboring molecules.

There are two common characteristics in the physical properties of the Ni_3 complex ions in **1** – **3** and the previous compounds.[11] (1) Intramolecular ferromagnetic interactions give the ground high-spin state (S = 3). (2) A uniaxial anisotropy is supposed to be present in the molecular axis direction. They are regarded as a prerequisite of SMMs. The features specific for **1** are summarized as follows. Thanks to the molecular arrangement in the crystal, the $D_{S=3}$ value has been precisely determined to be –2.2±0.1 K from single-crystal magnetic study. Furthermore, the cation portions of **1** are closely contacted and form an antiferromagentically coupled S = 3 SMM chain.

The crystal structure of **1** is very unique, and the Ni_3 trigonal bipyramid clusters like **1** – **3** have the following general advantages in the development of SMMs: preparation is simple, typically by one-step, the cost is low because nickel(II) is a common metal ion, and the analysis is easy because of the high symmetry. It is of great interest to explore novel SMMs showing intermolecular interaction, and development in this line is feasible by appropriate molecular and crystal design.[28] The halogen···halogen contacts seem to be one of good options to bestow intermolecular exchange couplings to SMM systems. The strength of intermolecular exchange coupling may be controlled by replacing a bulky substituent.

The ligand tmen has also been used in triangular compounds with cobalt(II) and iron(II)

ions,[13,32] and their molecular structures were similar to those of **1** – **3**. The magnetic properties of the Fe derivative were investigated, and the intramolecular ferromagnetic coupling was found in the magnetic measurements in 90 – 300 K.[32] The magnetic properties of the cobalt derivative have not yet been reported. Since a cobalt(II) ion has orbital angular momentum and magnetic anisotropy, the magnetic properties of the cobalt(II) triangles are of great interest for the development of novel SMMs.

References

(1) (a) D. Gatteschi, R. Sessoli, J. Villain, *Molecular Nanomagnets*, Oxford University Press, New York, **2006**; (b) D. Gatteschi, R. Sessoli, *Angew. Chem.*, *Int. Ed.* **2003**, *42*, 268; (c) *Single-Molecule Magnets and Related Phenomena*, ed. by R. Winpenny, Springer-Verlag Berlin, **2006**; (d) L. Bogani, W. Wersdorfer, *Nature Mat.* **2008**, *7*, 179.

(2) (a) P. D. W. Boyd, Q. Li, J. B. Vincent, K. Folting, H.-R. Chang, W. E. Streib, J. C. Huffman, G. Christou, D. N. Hendrickson, *J. Am. Chem. Soc.* **1988**, *110*, 8537; (b) A. Caneschi, D. Gatteschi, R. Sessoli, *J. Am. Chem. Soc.* **1991**, *113*, 5873; (c) R. Sessoli, H.-L. Tsai, A. R. Schake, S. Wang, J. B. Vincent, K. Folting, D. Gatteschi, G. Christou, D. N. Hendrickson, *J. Am. Chem. Soc*. **1993**, *115*, 1804.

(3) (a) J. R. Friedman, M. P. Sarachik, *Annu. Rev. Condens. Matter Phys.* **2010**, *1*, 109; (b) G. Christou, *Polyhedron* **2005**, *24*, 2065; (c) M. Andruh, J.-P. Costes, C. Diaz, S. Gao, *Inorg. Chem.* **2009**, *48*, 3342; (d) K. S. Pedersen, J. Bendix, R. Clérac, *Chem. Commun.* **2014**, *50*, 4396; (e) T. Glaser, *Chem. Commun.* **2011**, *47*, 116.

(4) (a) A. L. Barra, A. Caneschi, A. Cornia, F. Fabrizi de Biani, D. Gatteschi, S. Sangregorio, R. Sessoli, L. Sorace, *J. Am. Chem. Soc.* **1999**, *121*, 5302; (b) S. L. Castro, Z. Sun, C. M. Grant, J. C. Bollinger, D. N. Hendrickson, G. Christou, *J. Am. Chem. Soc.* **1998**, *120*, 2365; (c) A. J. Tasiopoulos, A. Vinslava, W. Wernsdorfer, K. A. Abboud, G. Christou, *Angew. Chem.*, *Int. Ed.* **2004**, *43*, 2117; (d) M. Murugesu, M. Habrych, W. Wernsdorfer, K. A. Abboud, G. Christou, *J. Am. Chem. Soc.* **2004**, *126*, 4766.

(5) (a) G. Christou, D. Gatteschi, D. N. Hendrickson, R. Sessoli, *MRS Bull.* **2000**, *25*, 66; (b) R. Bagai, G. Christou, *Chem. Soc. Rev.* **2009**, *38*, 1011; (c) G. Rogez, B. Donnio, E. Terazzi, J.-L. Gallani, J.-P. Kappler, J.-P. Bucher, M. Drillon, *Adv. Mater.* **2009**, *21*, 4323.

(6) (a) E.-C. Yang, D. N. Hendrickson, W. Wernsdorfer, M. Nakano, L. N. Zakharv, R. D. Sommer, A. L. Rheingold, M. Ledezma-Gairaud, G. Christou, *J. App. Phys.* **2002**, *91*, 7382;

(b) M.-H. Zeng, M.-X. Yao, H. Liang, W.-X. Zhang, X.-M. Chen, *Angew. Chem.*, *Int. Ed.* **2007**, *46*, 1832.

(7) (a) M. Moragues-Cánovas, M. Helliwell, L. Ricard, E. Rivière, W. Wernsdorfer, E. Brechin, T. Mallah, *Eur. J. Inorg. Chem.* **2004**, 2219; (b) E.-C. Yang, W. Wernsdorfer, L. N. Zakharov, Y. Karaki, A. Yamaguchi, R. M. Isidro, G.-D. Lu, S. A. Wilson, A. L. Rheingold, H. Ishimoto, D. N. Hendrickson, *Inorg. Chem.* **2006**, *45*, 529.

(8) (a) M. D. Godbole, O. Roubeau, R. Clérac, H. Kooijman, A. L. Spek, E. Bouwman, *Chem. Commun.* **2005**, 3715; (b) S. M. J. Aubin, M. W. Wemple, D. M. Adams, H.-L. Tsai, G. Christou, D. N. Hendrickson, *J. Am. Chem. Soc.* **1996**, *118*, 7746.

(9) (a) H. Miyasaka, R. Clérac, W. Wernsdorfer, L. Lecren, C. Bonhomme, K. Sugiura, M. Yamashita, *Angew. Chem.*, *Int. Ed.* **2004**, *43*, 2801; (b) H. Oshio, M. Nihei, A. Yoshida, H. Nojiri, M. Nakano, A. Yamaguchi, Y. Karaki, H. Ishimoto, *Chem. Eur. J.* **2005**, *11*, 843; (c) J.-P. Costes, F. Dahan, W. Wernsdorfer, *Inorg. Chem.* **2006**, *45*, 5; (d) G. Cucinotta, M. Perfetti, J. Luzon, M. Etienne, P.-E. Car, A. Caneschi, G. Calvez, K. Bernot, R. Sessoli, *Angew. Chem.*, *Int. Ed.* **2012**, *51*, 1606; (e) T. Ishida, R. Watanabe, K. Fujiwara, A. Okazawa, N. Kojima, G. Tanaka, S. Yoshii, H. Nojiri, *Dalton Trans.* **2012**, *41*, 13609.

(10) (a) G. A. Craig, M. Murrie, *Chem. Soc. Rev.* **2015**, *44*, 2135; (b) S. Gomez-Coca, E. Cremades, N. Aliaga-Alcalde, E. Ruiz, *J. Am. Chem. Soc.* **2013**, *135*, 7010.

(11) R. Biswas, Y. Ida, M. L. Baker, S. Biswas, P. Kar, H. Nojiri, T. Ishida, A. Ghosh, *Chem. Eur. J.* **2013**, *19*, 3943.

(12) K. Miyamoto, R. Koizumi, E. Horn, Y. Fukuda, *Z. Kristallogr. NCS* **2005**, *220*, 226.

(13) D. A. Handley, P. B. Hitchcock, G. J. Leigh, *Inorg. Chim. Acta* **2001**, *314*, 1.

(14) F. A. Cotton, *Chemical Applications of Group Theory,* 2nd Ed., John Wiley and Sons, Inc., New York, **1971**.

(15) A. Bondi, *J. Phys. Chem.* **1964**, *68*, 441.

(16) L. Pauling, *The Nature of the Chemical Bond*, Cornell University Press, Ithaca, **1961**.

(17) G. A. Kakos, G. Winter, *Aust. J. Chem.* **1970**, *23*, 15.

(18) M. A. Novak, R. Sessoli, *Quantum Tunneling of magnetization−QTM'94*, ed. by L. Gunther, B. Barbara, Springer Netherlands, **1995**, pp. 171–188.

(19) E. C. Stoner, E. P. Wohlfarth, *Philos. Trans. R. Soc., A* **1948**, *240*, 599.

(20) (a) D. Serantes, D. Baldomir, *The Open Surface Sci. J.* **2012**, *4*, 71; (b) G. C. Papaefthymiou, *Nano Today* **2009**, *4*, 438.

(21) (a) L. Néel, *Ann. Geophys.* **1988**, *5*, 99; (b) *Selected Works of Louis Néel*, ed. by N. Kurti, Gordon and Breach Science Publishers, pp. 405–427.

(22) E.-C. Yang, W. Wernsdorfer, S. O. Hill, R. S. Edwards, M. Nakano, S. Maccagnano, L. N. Zakharov, A. L. Rheingold, G. Christou, D. N. Hendrickson, *Polyhedron* **2003**, *22*, 1727.

(23) J. Bartolomé, G. Filoti, V. Kuncser, G. Schinteie, V. Mereacre, C. E. Anson, A. K. Powell, D. Prodius, C. Turta, *Phys Rev. B* **2009**, *80*, 014430.

(24) (a) P. W. Anderson, *Phys. Rev*. **1959**, *115*, 2; (b) J. Kanamori, *J. Phys. Chem. Solids* **1959**, *10*, 87; (c) J. B. Goodenough, *J. Phys. Chem. Solids* **1958**, *1*, 287; (d) H. Oshio, M. Nakano, *Chem. Eur. J.* **2005**, *11*, 5178.

(25) (a) J. A. Bertrand, A. P. Ginsberg, R. I. Kaplan, C. E. Kirkwood, R. L. Martin, R. C. Sherwood, *Inorg. Chem.* **1971**, *10*, 240; (b) A. K. Ghosh, M. Shatruk, V. Bertolasi, K. Pramanik, D. Ray, *Inorg. Chem.* **2013**, *52*, 13894; (c) J. A. Barnes, W. E. Hatfield, *Inorg. Chem.* **1971**, *10*, 2355; (d) C. Ding, C. Gao, S. Ng, B. Wang, Y. Xie, *Chem. Eur. J.* **2013**, *19*, 9961; (e) A. Ferguson, M. Schmidtmann, E. K. Brechinb, M. Murrie, *Dalton Trans.* **2011**, *40*, 334; (f) H.-S. Wang, Y. Song, *Inorg. Chem. Commun.* **2013**, *35*, 86; (g) J.-P. Sun, L.-C. Li, X.-J. Zheng, *Inorg. Chem. Commun.* **2011**, *14*, 877; (h) M. A. Halcrow, J.-S. Sun , J. C. Huffman, G. Christou, *Inorg. Chem.* **1995**, *34*, 4167; (i) A. Burkhardt, E. T. Spielberg, S. Simon, H. Görls, A. Buchholz, W. Plass, *Chem. Eur. J.* **2009**, *15*, 1261; (j) A. D. Katsenis, V.

G. Kessler, G. S. Papaefstathiou, *Dalton Trans.* **2011**, *40*, 4590; (k) A. Das, F. J. Klinke, S. Demeshko, S. Meyer, S. Dechert, F. Meyer, *Inorg. Chem.* **2012**, *51*, 8141.

(26) (a) Q.-X. Li, Q.-H. Luo, Y.-Z. Li, C.-Y. Duan, Q.-Y. Tu, *Inorg. Chim. Acta* **2005**, *358*, 504; (b) A. Tamayo, L. Escriche, C. Lodeiro, J. Ribas-Ariño, J. Ribas, B. Covelo, J. Casabó, *Inorg. Chem.* **2006**, *45*, 7621.

(27) (a) J. J. Borrás-Almenar, J. M. Clemente-Juan, E. Coronado, B. S. Tsukerblat, *Inorg. Chem.* **1999**, *38*, 6081; (b) J. J. Borrás-Almenar, J. M. Clemente-Juan, E. Coronado, B. S. Tsukerblat, *J. Comput. Chem.* **2001**, *22*, 985.

(28) (a) W. Wernsdorfer, N. Aliaga-Alcalde, D. N. Hendrickson, G. Christou, *Nature* **2002**, *416*, 406; (b) H. Miyasaka, K. Nakata, L. Lecren, C. Coulon, Y. Nakazawa, T. Fujisaki, K. Sugiura, M. Yamashita, R. Clérac, *J. Am. Chem. Soc.* **2006**, *128*, 3770; (c) A. Okazawa, T. Nogami, H. Nojiri, T. Ishida, *Chem. Mater.* **2008**, *20*, 3110.

(29) J. D. Rinehart, M. Fang, W. J. Evans, J. R. Long, *J. Am. Chem. Soc.* **2011**, *133*, 14236.

(30) (a) M.-H. Whangbo, H.-J. Koo, D. Dai, *J. Solid State Chem.* **2003**, *176*, 417; (b) M.-H. Whangbo, H.-J. Koo, D. Dai, D. Jung, *Inorg. Chem.* **2003**, *42*, 3898; (c) R. D. Willett, B. Twamley, W. Montfrooij, G. E. Granroth, S. E. Nagler, D. W. Hall, J.-H. Park, B. C. Watson, M. W. Meisel, D. R. Talham, *Inorg. Chem.* **2006**, *45*, 7689; (d) J. L. Manson, M. M. Conner, J. A. Schlueter, A. C. McConnell, H. I. Southerland, I. Malfant, T. Lancaster, S. J. Blundell, M. L. Brooks, F. L. Pratt, J. Singleton, R. D. McDonald, C. Lee, M.-H. Whangbo, *Chem. Mater.* **2008**, *20,* 7408; (e) J. A. Schlueter, H. Park, G. J. Halder, W. R. Armand, C. Dunmars, K. W. Chapman, J. L. Manson, J. Singleton, R. McDonald, A. Plonczak, J. Kang, C. Lee, M.-H. Whangbo, T. Lancaster, A. J. Steele, I. Franke, J. D. Wright, S. J. Blundell, F. L. Pratt, J. deGeorge, M. M. Turnbull, C. P. Landee, *Inorg. Chem.* **2012**, *51*, 2121.

(31) (a) J. A. Schlueter, H. Park, G. J. Halder, W. R. Armand, C. Dunmars, K. W. Chapman, J. L. Manson, J. Singleton, R. McDonald, A. Plonczak, J. Kang C. Lee, M.-H. Whangbo, T.

Lancaster, A. J. Steele, I. Franke, J. D. Wright, S. J. Blundell, F. L. Pratt, J. de George, M. M. Turnbull, C. P. Landee, *Inorg. Chem.* **2012**, *51*, 2121; (b) M.-H. Whangbo, H.-J. Koo, D. Dai, D. Jung, *Inorg. Chem.* **2003**, *42*, 3898; (c) M. M. Turnbull, C. P. Landee, B. M. Wells, *Coord. Chem. Rev.* **2005**, *249*, 2567; (d) R. D. Willett, B. Twamley, W. Montfrooij, G. E. Granroth, S. E. Nagler, D. W. Hall, J.-H. Park, B. C. Watson, M. W. Meisel, D. R. Talham, *Inorg. Chem.* **2006**, *45*, 7689; (e) L. Li, M. M. Turnbull, C. P. Landee, J. Jornet, M. Deumal, J. J. Novoa, J. L. Wikaira, *Inorg. Chem.* **2007**, *46*, 11254.

(32) S. C. Davies, D. L. Hughes, G. J. Leigh, J. R. Sanders, J. S. de Souza, *J. Chem. Soc., Dalton Trans.* **1997**, 1981.

3 Study on Hinge-like $Dy(O_2Cu)_2$ Complexes

3.1 Abstract

In the 3d-4f heteronuclear systems, it is usually difficult to evaluate the exchange coupling of Ln^{3+} compounds by using conventional magnetic measurements because of the presence of unquenched orbital moment contribution and crystal field splitting. The HF-EPR technique was properly utilized to this system. The important point is that the resonance fields of 3d transition metal ions are biased by the exchange field from 4f ions. Two novel trinuclear isomeric compounds $[\{(Cu^{II}(salpn))(Me(CO)Me)\}_2Dy^{III}(NO_3)_3]$ (**4**) and $[\{Cu^{II}(salpn)\}_2Dy^{III}(H_2O)(NO_3)_3]$-·MeOH (**5**) along with one novel polymeric compound $\{[\{Cu^{II}(salpn)\}_2Dy^{III}(NO_3)_3bpy]\cdot MeOH\cdot H_2O\}_n$ (**6**) were prepared by Ghosh and co-workers, using a metalloligand $[Cu^{II}(salpn)]$, where H_2salpn and bpy stand for *N*,*N'*-bis(salicylidene)-1,3-propanediamine and 4,4'-bipyridine, respectively. The Dy^{3+} and Cu^{2+} ions are doubly bridged with oxygen atoms, and the core DyO_2Cu skeletons are characterized by the "butterfly" angles of 140.9±0.1, 147±2, and 142.4±0.2° for **4**, **5**, and **6**, respectively. The author and co-workers have investigated that the molecular structures and magnetic properties of **4** – **6** by using high-frequency electron paramagnetic resonance (HF-EPR), magnetization, and magnetic susceptibility techniques. These compounds showed slow magnetization reversal and SMM behavior in the measurements of alternating current magnetic susceptibility. The HF-EPR analyses of frequency-field diagrams were used an effective spin-Hamiltonian including and found that the exchange couplings are ferromagnetic in all compounds. The exchange coupling parameters $J_{Dy\text{-}Cu}$'s of **4**, **5**, and **6** were determined as 2.25±0.05, 1.82±0.04, and 1.79±0.04 K, respectively. In order to find out relationship for exchange coupling parameter and structural parameters, the previously reported compounds were also considered by using EPR analysis on $[Cu^{II}(L^A)(C_3H_6O)Dy^{III}(NO_3)_3]$ (H_2L^A = *N*,*N*'-bis(3-methoxysalicylidene)-1,3-diamino-2,2-dimethylpropane) and $[Dy^{III}L^B{}_2(NO_3)_2\{Cu^{II}$-

$(CH_3OH)\}_2](NO_3)(CH_3OH)$ (H_2L^B = 2,6-bis(acetylaceto)pyridine). The present result shows an advantage of doubly oxygen-bridged motifs to contribute strong ferromagnetic interactions between 4f and 3d ions. The exchange coupling strength was found to be sensitive to the structural parameters such as bond angles, bond lengths, and "butterfly" angles. Determination of the exchange parameters would contribute to development of exchange-coupled 4f-3d heterometallic complexes.

3.2 Introduction

Single-molecule magnets SMMs with 3d ions have been well researched (see Chapter 1 and 2), and heterometallic 4f-3d compounds have been also intensively studied for the development of SMMs,[1-3] because using each lanthanide (Ln) ion has advantages in strong magnetic anisotropy and large magnetic moment.[4-6] It is important to estimate the exchange coupling between 4f-3d ions for development of high-performance SMMs. The relationship of exchange couplings and structural parameters has been investigated in the Gd-Cu systems. In Gd-Cu systems, the ferromagnetic couplings between Gd^{3+} (S = 7/2) and Cu^{2+} (S = 1/2) are often observed;[7-10] for example, the dinuclear doubly oxygen-bridged Gd-Cu complexes have ferromagnetic couplings and show the S = 4 ground state.[11] In case of Gd-based complexes, the exchange coupling can be evaluated by combining the temperature dependence of the magnetic susceptibility and the magnetization curve at low temperature. It is because a Gd^{3+} ion is in the isotropic S-state, leading to simple analysis even with a powder sample. Moreover, the consideration of the LS multiplet splitting is not necessary to analyze the magnetic data at low temperatures because the splitting is very large. Hence, the exchange couplings have been quantitatively studied by conventional magnetometries,[11-13] and their magneto-structure relation was well examined. It is noticed that a planar structure favors ferromagnetic coupling in the four-membered CuO_2Gd moiety. Although Gd^{3+} and Cu^{2+} ions are coupled ferromagnetically, there is a weak point of Gd complexes in

creating new SMMs; Gd^{3+} ion has a spin-only character and weak magnetic anisotropy. It is the disadvantage compared to the heavy Ln ions having an unquenched orbital moment and large magnetic anisotropy.

Despite the clear advantages of using heavy Ln ions involving Tb^{3+} and Dy^{3+} ions, there has been an essential difficulty in the determination of the exchange couplings. An analysis of temperature dependence of the magnetic susceptibility is quite difficult because of the complex energy scheme caused by the spin-orbit coupling and crystal field splitting (CFS), and thus the exchange coupling parameter can hardly be determined by the only magnetic susceptibility due to ignoring the spin-orbit coupling effects.

Nojiri, Ishida, and co-workers have developed a new microscopic method for the precise evaluation of exchange coupling in SMMs including heavy Ln ions,[14-16] and have established the usefulness in the studies of various 4f-3d-based SMMs.[2,17] They utilize the high-frequency electron paramagnetic resonance (EPR) to observe the resonances of 3d transition metal ions biased by the exchange fields from Ln ions. The high magnetic field and low-temperature magnetization measurement which traces the ground state of the system is also combined with the EPR analysis. The author and co-workers would like to apply it to a series of 4f-3d heterometallic compounds with a small structural modification. The systematic work may afford a magneto-structure relation which is highly important in researches of 4f-based magnetic materials.

There is, for example, the diphenoxo-bridged dinuclear Cu–Tb motif. It is found that when the environment around Tb^{3+} ion has a low symmetry of the ligand field, a uniaxial anisotropy may be favorable, but in a high symmetrical environment, axial anisotropy is weak.[18] The paucity of such examples is presumably due to the low synthetic strategies using designed organic ligands allowing significant flexibility in the 3d-4f coordination clusters.[19] Recently, Ghosh et al. have synthesized of $[\{Cu^{II}(salpn)\}_2Ln^{III}(X)_n]$ (Ln^{3+} = Tb^{3+}, a non-Kramers ion, H_2salpn =

N,*N′*-bis(salicylidene)-1,3-propanediamine), which show SMM behavior.[20]

The motivation of the present work is to investigate the SMM behavior and 4f-3d exchange coupling in above derivatives involving Ln^{3+} = Dy^{3+} (a Kramers ion) in different coordination environments but with the same ligand systems. Herein, two trinuclear isomeric compounds $[\{(Cu^{II}(salpn))(Me(CO)Me)\}_2Dy^{III}(NO_3)_3]$ (**4**) and $[\{Cu^{II}(salpn)\}_2Dy^{III}(H_2O)(NO_3)_3]\cdot MeOH$ (**5**) along with one polymeric compound $\{[\{Cu^{II}(salpn)\}_2Dy^{III}(NO_3)_3bpy]\cdot MeOH\cdot H_2O\}_n$ (**6**) have been synthesized, where bpy stands for 4,4'-bipyridine (Scheme 3.1). They possess a DyO_2Cu structure in common. The ferromagnetic coupling by dc magnetic measurements and slow magnetization reorientation by ac magnetic susceptibility measurements for all complexes are also reported here.

The next motivation is to study the exchange coupling of a few new Dy–Cu compounds and compare the results on relevant compounds. The examination of relation between the exchange couplings and various structural parameters would be helpful for rational molecular design and synthesis of high-performance SMMs and related magnetic materials. To the best of our knowledge such systematic study of exchange coupling has not been made so far.

Scheme 3.1. Structural formulae of **4** – **6**.

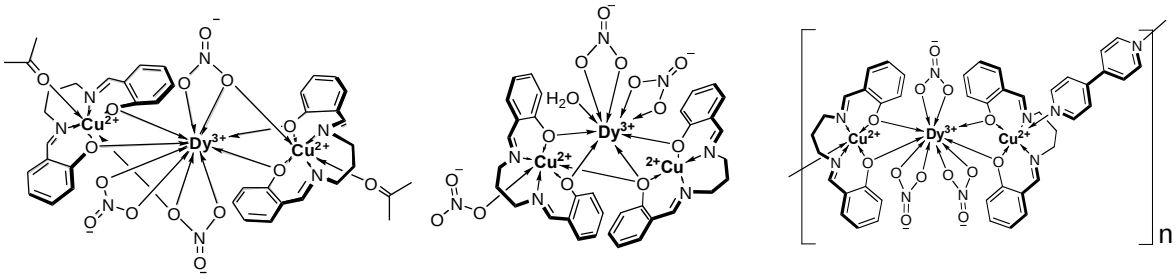

4 **5** **6**

3.3 Experimental Section

The specimens **4** – **6** were provided by Mr. Soumavo Ghosh (Univ. of Calcutta). For the details of preparation and crystal structure analysis of the Tb analogues, see ref 21.

The measurement instruments are described in Chapter 1.8. The magnetizations and susceptibilities on randomly oriented polycrystalline specimens were collected after the sample suspension was suspended on heating and then solidified on cooling without any applied field.

3.4 Results

3.4.1 Characterization

Compounds **4** and **5** have a similar chemical composition although there are some differences of the synthesis methods (solvents, temperature etc.). The phase purity of both **4** and **5** has been confirmed from the identity of the PXRD patterns (Figure 3.1), indicating that each isomeric structure was formed exclusively.

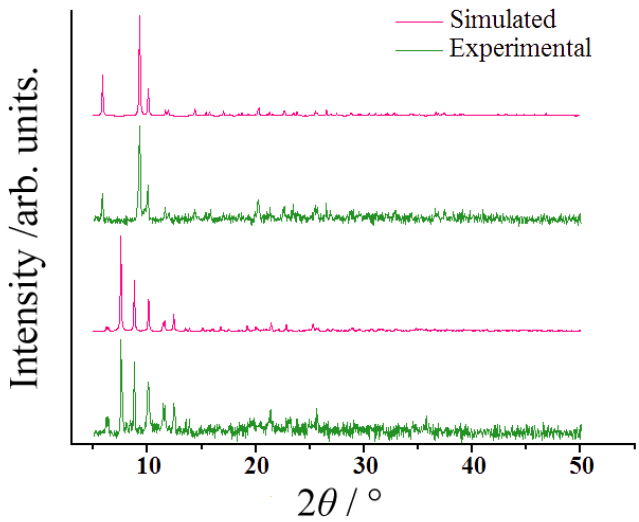

Figure 3.1. Powder XRD patterns of (top) **4** and (bottom) **5**.

3.4.2 Crystal Structures

Compounds **4** – **6** have the same [{Cu(salpn)}$_2$Dy] core skeleton, like a molecular hinge with *cisoid-transoid*-type folding.[22] Selected crystal data and structure refinement results for **4** – **6** are summarized in Table 3.1. The molecular structure of **4** together with atomic numbering is shown in Figure 3.2a. The space group of the crystal of **4** is tetragonal $I4_1/a$ with $Z = 8$. In the trinuclear molecule, two metalloligands [Cu(salpn)] serve as a chelate ligand to the central Dy^{3+} ion via bidentate μ_2-phenoxido oxygen atom in approximately coplanar orientation, making the {Cu(salpn)}$_2$Dy coordination cluster *transoid*. In addition, three chelating nitrato (κ^2*O,O*') coligands are bonded to the Dy center, building up deca-coordination. Two of three nitrates also bridge (1κ*O*:2κ^2*O,O*') the Cu atoms with the Dy centers. The molecule is symmetrically halved by a C_2 axis passing parallel to the crystallographic *c*-axis through the O4−N3−Dy1 atoms. Accordingly the nearest Dy···Cu geometry is unique, which will be important information for modeling of exchange coupling.

Table 3.1. Crystal data and structure refinement results for **4** – **6**.

Compound	**4** (*transoid*)	**5** (*cisoid*)	**6** (polymeric)
Formula	$C_{40}H_{44}N_7O_{15}Cu_2Dy$	$C_{35}H_{38}N_7O_{15}Cu_2Dy$	$C_{45}H_{46}N_9O_{15}Cu_2Dy$
Formula weight	1152.42	1086.32	1242.49
Crystal system	Tetragonal	Triclinic	Monoclinic
Space group	$I4_1/a$	$P\bar{1}$	$C2/c$
a /Å	17.583(5)	10.467(3)	15.334(6)
b /Å	17.583(5)	14.653(4)	25.950(10)
c /Å	29.716(5)	15.096(4)	15.975(9)
α /°	90	104.450(3)	90
β /°	90	100.006(3)	113.080(4)
γ /°	90	99.252(3)	90
V /Å^3	9187(4)	2156.8(11)	5848(4)
Z	8	2	4
$R(F)$ ($I > 2\sigma(I)$)[a)]	0.0347	0.0650	0.0758
$R_w(F^2)$ (all data)[b)]	0.0890	0.2245	0.2336

[a)] $R = \Sigma \, ||F_o| - |F_c|| / \Sigma \, |F_o|$. [b)] $R_w = [\Sigma \, w(F_o^2 - F_c^2)^2 / \Sigma \, w(F_o^2)^2]^{1/2}$.

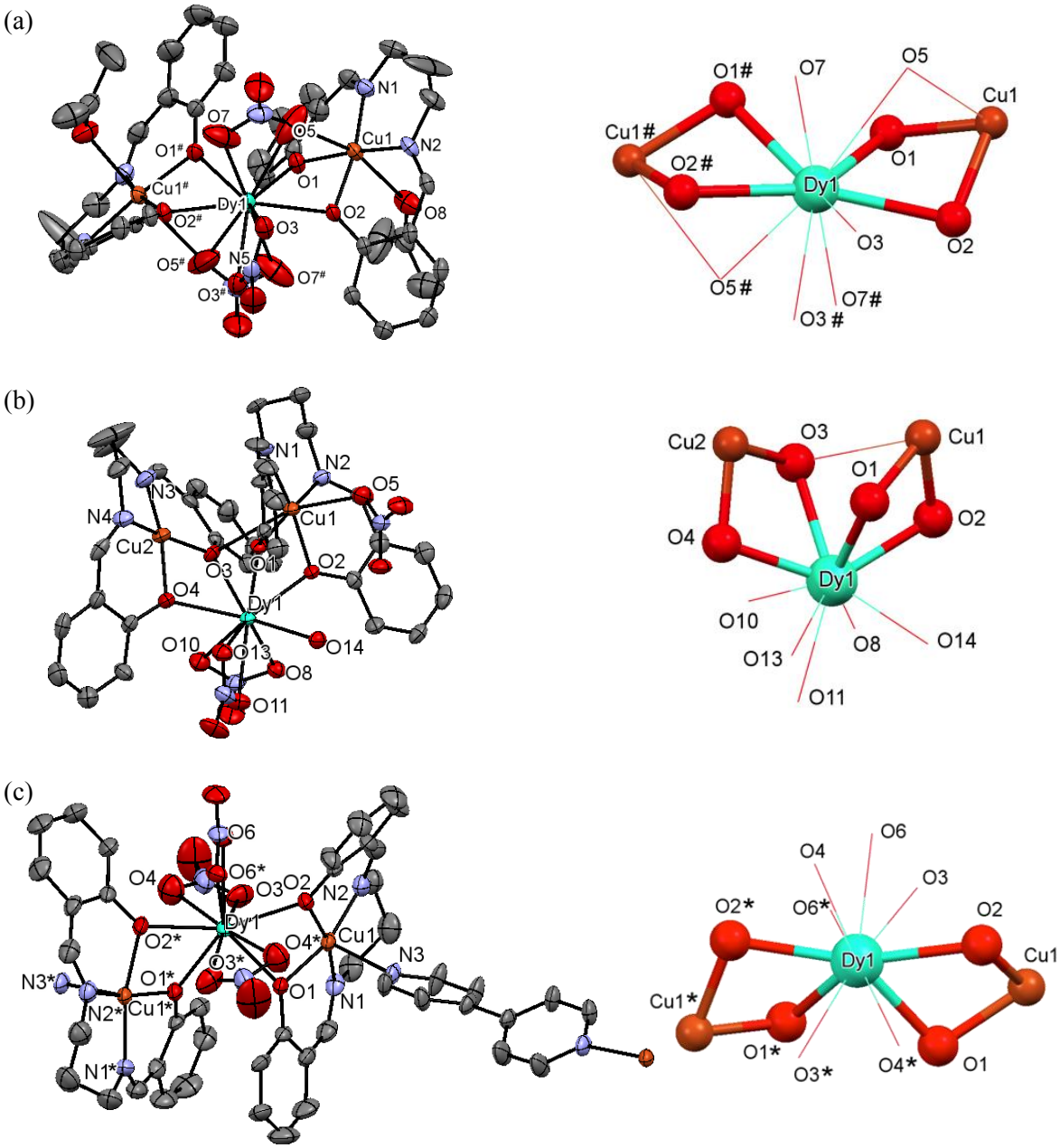

Figure 3.2. X-ray crystal structures (left) and skeletal views of the Dy surroundings and Cu atoms (right) for (a) **4**, (b) **5**, and (c) **6**. Thermal ellipsoids are drawn at the 30% probability level. Hydrogen atoms and solvent molecules are omitted for clarity. Atomic labeling of selected atoms is also shown. Symmetry operation codes of # in **4** and * in **6** are (1−*x*, 1/2−*y*, *z*) and (1−*x*, *y*, 1/2−*z*), respectively.

The vertex of the coordination polyhedron of the central Dy^{3+} ion in **4** is symmetrically constructed by ten oxygen atoms from five bidentate ligands with an average Dy−O bond

distances of 2.51(1) Å that can be regarded as a distorted tetradecahedron.[23] Selected bond distances and angles are summarized in Table 3.2. Four oxygen atoms of the two metalloligands, i.e., O1 and O2 (and O1# and O2#) are at the distances of 2.368(3) and 2.372(2) Å, respectively, where the symmetry operation code of # is (1−*x*, 1/2−*y*, *z*).

Table 3.2. Selected atomic distances (Å), bond angles (°), and "butterfly" angles (ϕ, °).

Compound	**4**	**5**	**6**
Dy1⋯Cu1	3.301(1)	3.311(2)	3.358(1)
Dy1⋯Cu2	-	3.356(2)	-
Dy1–O1	2.368(3)	2.337(7)	2.376(6)
Dy1–O2	2.372(2)	2.385(7)	2.387(7)
Cu1–O1	1.944(3)	1.977(7)	1.976(6)
Cu1–O2	1.952(2)	1.959(7)	1.975(8)
Cu1–O3	-	2.802(8)	-
Cu1–O5	2.616(6)	2.446(10)	-
Dy1–O3	2.500(3)	2.496(7)	2.530(12)
Dy1–O7/–O4[a)]	2.543(7)	2.362(8)	2.606(14)
Cu2–O3	-	1.944(8)	-
Cu2–O4	-	1.915(7)	-
Cu1–O1–Dy1	99.5(1)	99.9(3)	100.6(2)
Cu1–O2–Dy1	99.1(1)	98.9(3)	100.3(3)
Cu2–O3–Dy1	-	97.4(3)	-
Cu2–O4–Dy1	-	102.9(3)	-
ϕ(Dy1−O1⋯O2−Cu1)	140.9(1)	148.9(3)	142.4(2)
ϕ(Dy1−O3⋯O4−Cu2)	-	145.2(3)	-

[a)] O7 for **4** and O4 for **5** and **6**.

Each of the two symmetrically related terminal copper atoms of the trinuclear [{Cu(salpn)}$_2$Dy] core in **4** is bonded to N_2O_2 donor set of atoms (O1, O2, N1, N2 for Cu1) of the tetradentate ligand salpn^{2-}, making up the equatorial plane with Cu−O and Cu−N distances of 1.944(3) − 1.952(3) and 1.958(3) − 1.978(4) Å respectively. Two axial positions of the distorted

octahedral Cu1 atoms are occupied by oxygen atoms O5 and O8 of bridging nitrato coligand and acetone solvate at the distances of 2.616(6) and 2.573(4) Å, respectively. The bridging atoms are O1, O2, and O5, but the O1 and O2 bridges are important for the exchange coupling because they are located at the equatorial sites of Cu1.

The space group of **5** is $P\bar{1}$ with Z = 2. The whole molecule is crystallographically independent. Two bidentate metalloligands are bonded to the central Dy atom in an asymmetric angular orientation via two μ_2-phenoxido oxygen atoms (Figure. 3.2b) that can be regarded as *cisoid* coordination. Two chelating nitrato (κ^2*O,O'*) and one coordinated water molecule build up the nine-coordination, approximately forming a tricapped trigonal prism.[20] The third nitrato ligand is coordinated axially to the Cu atom of one of the coordinated metalloligands.

The vertexes of the coordination polyhedron of the central Dy^{3+} ion in **5** are constructed by nine oxygen atoms with average Dy−O bond distances of 2.43(2) Å. The four of the nine oxygen atoms, namely O1, O2, O3, and O4, that belong to the two metalloligands are at distances 2.337(7) − 2.496(7) Å. Another four oxygen atoms belonging to two nitrato coligands, i.e., O8, O10, O11, and O13, are at distances between 2.438(8) − 2.550(9) Å.

There are two independent copper ions and accordingly two independent nearest Dy···Cu geometries. Each of the two terminal copper atoms of the trinuclear [{Cu(salpn)}$_2$Dy] core in **5** is bonded to four donor atoms of the N_2O_2 Schiff base salpn^{2-}, making up a planar arrangement. The Cu−O and Cu−N distances are in the ranges of 1.915(7) − 1.977(7) Å and 1.937(12) − 1.985(9) Å, respectively. One of the axial coordination sites of Cu1 atom is occupied by an oxygen atom O5 of a nitrato coligand at the distance of 2.446(10) Å, indicating a square pyramidal geometry. Although Cu1 and Dy1 are triply bridged, the bond mediated by O3 does not contribute to Dy−Cu magnetic coupling because of the long bond length (2.802(8) Å). On the other hand, Cu2 has no axial ligand.

Compound **6** crystallizes in a monoclinic $C2/c$ space group with Z = 4 (Figure 3.2). The

molecules of **6** forms an infinite chain along the crystallographic *a* axis with $[\{Cu(salpn)\}_2Dy(NO_3)_3bpy]$ as a repeating unit. The asymmetric unit involves a half of the repeating unit owing to the twofold symmetry; namely, the nearest Cu···Dy geometry is unique.

The repeating unit of **6** consists of a trinuclear core $\{Cu(salpn)\}_2Dy(NO_3)_3$ and a bpy bridge. The Dy^{3+} ion is ten-coordinate with four oxygen atoms from two [Cu(salpn)] and six oxygen atoms from three bidentate nitrate ions. The copper ion has an N_2O_2 donor set (O1, O2, N1, and N2) of the tetradentate salpn ligand on the basal plane. Although there is a bpy molecule between the nearest neighboring Cu···Cu ions, the nitrogen atoms in bpy are located at an axial position of the copper ion. Hence, Cu···Cu exchange coupling will be negligible.[24] In short, **6** has a polymeric crystal structure, but the magnetic structure is practically monomeric as a $\{Cu(salpn)\}_2Dy(NO_3)_3$ unit.

In the repeating unit of **6**, the vertex of the coordination polyhedron of the central Dy^{3+} ion is similar to that of **4**. A C_2 axis runs through the Dy^{3+} ion, and an average Dy−O bond distance is 2.48(3) Å.

To feature the skeleton of LnO_2Cu four-membered rings, a "butterfly" angle, ϕ, is proposed as an important parameter.[11-13] The "butterfly" angle is between the two planes (CuO_2 and LnO_2) involving the bridging oxygen atoms and each metal ion. In the Gd−Cu dinuclear systems examined in the ref. 11, when the GdO_2Cu ring is more planar, ferromagnetic coupling is stronger. Table 3.1 shows important geometrical parameters including "butterfly" angles. In the present $\{Cu(salpn)\}_2Dy$ compounds, the nearest neighboring Dy^{3+} and Cu^{2+} ions are always exchange-coupled through the double oxygen bridge with a "butterfly" skeleton. There are one, two, and one crystallographically independent Dy···Cu geometries in the unit cells of **4**, **5**, and **6**, respectively. Accordingly the exchange coupling parameters $J_{Dy\text{-}Cu}$ are unique for **4** and **5**, while **6** has two independent $J_{Dy\text{-}Cu}$ parameters.

3.4.3 Magnetic Properties

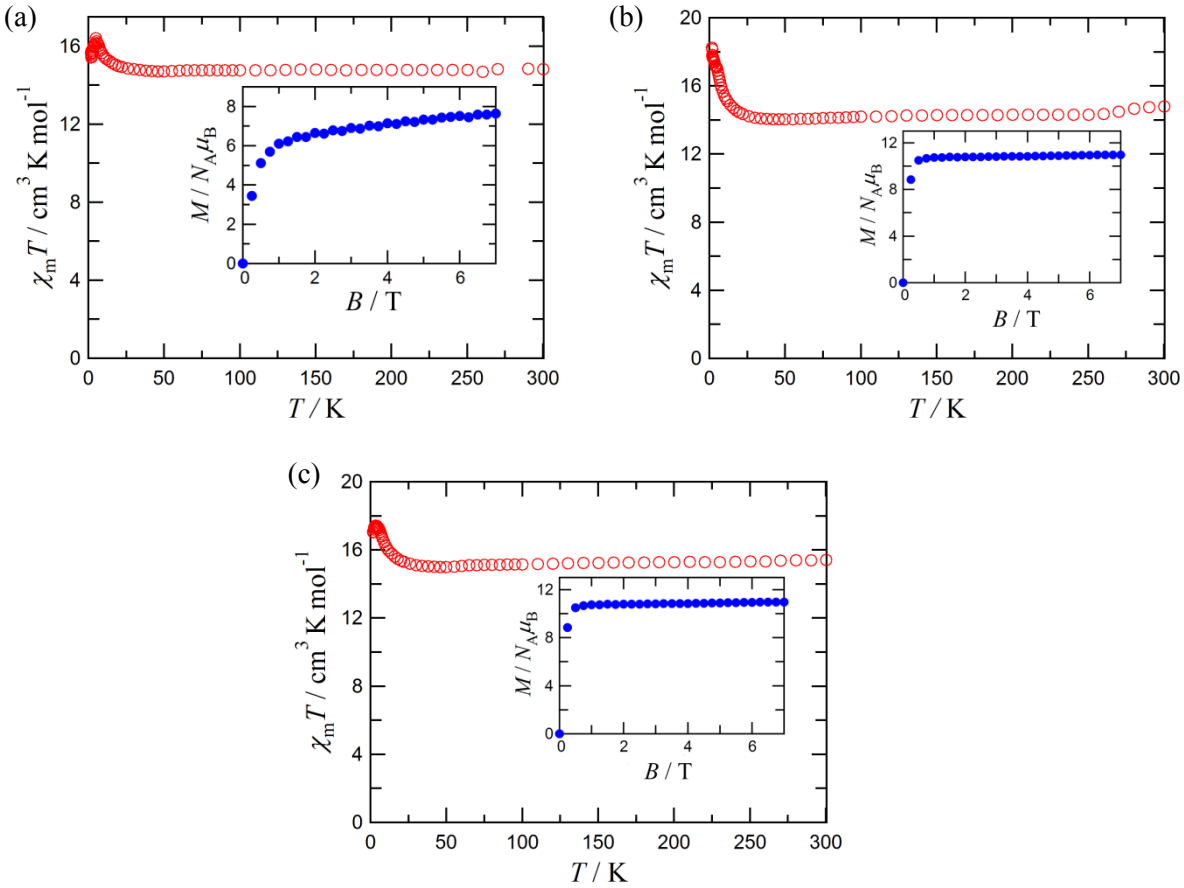

Figure 3.3. $\chi_m T$ vs. T plots measured at 500 Oe for (a) **4**, (b) **5**, and (c) **6**. The insets show the magnetization curves measured at 1.8 K under non-fixed powder conditions.

Polycrystalline specimens of **4** – **6** were subjected to magnetic susceptometry (Figure. 3.3). The randomly oriented samples were fixed with a small amount of mineral oil. Here, the $\chi_m T$ vs. T plots are drawn in a temperature range of 1.8 – 300 K, and the dc field of 500 Oe was applied. The observed $\chi_m T$ value at 300 K was 14.8, 14.8, and 15.4 cm^3 K mol^{-1} for **4**, **5**, and **6**, respectively, which are close to the expected value 14.9 cm^3 K mol^{-1} from the sum of two paramagnetic Cu^{2+} ions (S = 1/2, g = 2) and one free Dy^{3+} ion (J = 15/2, g_J = 4/3) for every $\{Cu(salpn)\}_2Dy$ unit. On cooling, the $\chi_m T$ values increased for all case, which indicates the possible ferromagnetic coupling, and as the crystallographic analysis indicates, they are ascribable

to the interactions between the nearest Dy^{3+} and Cu^{2+} ions. Intermolecular exchange couplings are negligible because the non-monotonic behavior of susceptibility at the lowest temperature regions is possibly caused by such negligible couplings.

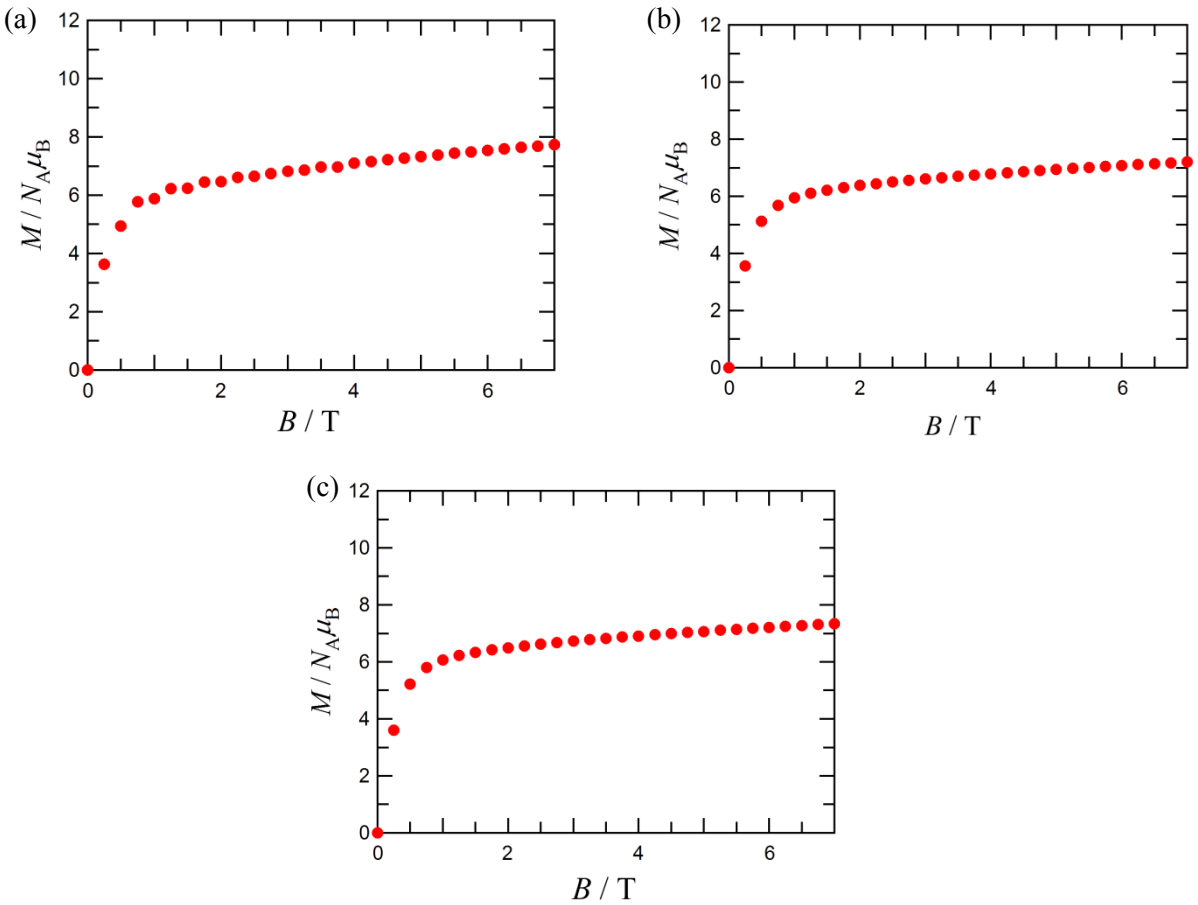

Figure 3.4. Magnetization curves measured at 1.8 K for the randomly oriented polycrystalline specimens of (a) **4**, (b) **5**, and (c) **6**. The samples were fixed with a small amount of mineral oil.

The powder data of the magnetization curves of **4** – **6** were obtained at 1.8 K after the specimens were fixed with a small amount of mineral oil (Figure. 3.4). Slow saturation behavior was found, indicating the relatively strong magnetic anisotropy. To obtain information on the ground J^F value, the magnetizations of powdery specimens were measured without mineral oil and allowed them to align in the applied field direction. The field alignment effect was confirmed by

the increase of the magnetization in the successive measurement cycles. As shown in the inset of Figure 3.3a, the magnetization of **4** is 7.6 μ_B at 7 T, and it is still gradually increasing. It indicates that the magnetic field alignment is not perfect. The finite slope of the magnetization curve in higher magnetic fields region is consistent with the partial orientation. Owing to the molecular arrangement in the tetragonal $I4_1/a$ space group, there are four different easy axis orientations in a unit cell. Because of the strong anisotropy of Dy^{3+}, the moments are canted from the external uniform magnetic field direction. This canting causes the large reduction of the saturation moments and almost linear increase in a high magnetic field region for **4**. Such behavior could not be observed for **5** or **6**, being in compatible with the unique magnetic easy axis in a unit cell owing to the crystallographic centrosymmetry.

The magnetization of **5** displayed more rapid saturation and reached the value of 11.0 μ_B at 7 T (the inset of Figure 3.3b). The saturation magnetization for ferrimagnetic configuration is 8 μ_B, and the ferromagnetic configuration is 12 μ_B when g-value of Cu^{2+} is 2 and $J^z = \pm 15/2$ for Dy^{3+} ion. Although the observed value was slightly smaller than 12 μ_B for the incomplete field alignment, the larger saturation value clearly indicates the presence of ferromagnetic coupling between Cu^{2+} and Dy^{3+} and the domination of the ground $J^z = \pm 15/2$ state for the Dy^{3+} ion in **5**.

A sharp rise of magnetization was found with the saturation moment of 11.0 μ_B per the formula unit for **6** (the inset of Figure 3.3c). The saturation moment is close to the theoretical 12 μ_B. Similar to the case of **5**, the susceptibility and magnetization indicate that Dy^{3+} and Cu^{2+} couples ferromagnetically and that $J^z = 15/2$ is dominant in the ground state of Dy^{3+}.

However, it should be noted that the perfectness of the magnetic field alignment is determined by the relation between the domain and powder sizes of the sample. The reduction is expected when the powder size is larger than the single domain size to give polycrystalline. Thus, the bulk measurement alone cannot give conclusion about the magnetic coupling and the ground state, and the EPR measurement is essential for the quantitative analysis (see below).

The results on dc magnetic measurements are summarized in Table 3.3. The exchange couplings of the present Dy–Cu derivatives probably are all ferromagnetic. Many "butterfly" GdO_2Cu compounds showed ferromagnetic coupling.[11-13] According to an empirical rule,[6b,8,15-17,20,25] the sign of the exchange coupling among Gd and heavy lanthanide ions are common in many cases. The present results are reasonably acceptable.

Table 3.3. Magnetic properties of **4** – **6**.

Compound	**4**	**5**	**6**
$\chi_m T$ / cm^3 K mol^{-1} at 300 K	14.8	14.8	15.4
Theoretical $\chi_m T$ [a)] / cm^3 K mol^{-1}	14.9	14.9	14.9
$\chi_m T$ / cm^3 K mol^{-1} at 3 K	15.8	17.5	17.4
Applied magnetic field / Oe	500	500	500
M /μ_B at 7 T, 1.8 K	7.6	11.0	11.0
Theoretical saturation M [b)] /μ_B	12	12	12

[a)] Sum of free ion values; one J = 15/2 (Dy^{3+}) and two S =1/2 (Cu^{2+}) ions. [b)] Sum of the values from one J = 15/2 (Dy^{3+}) and two S =1/2 (Cu^{2+}) ions.

3.4.4 Relaxation of Magnetization

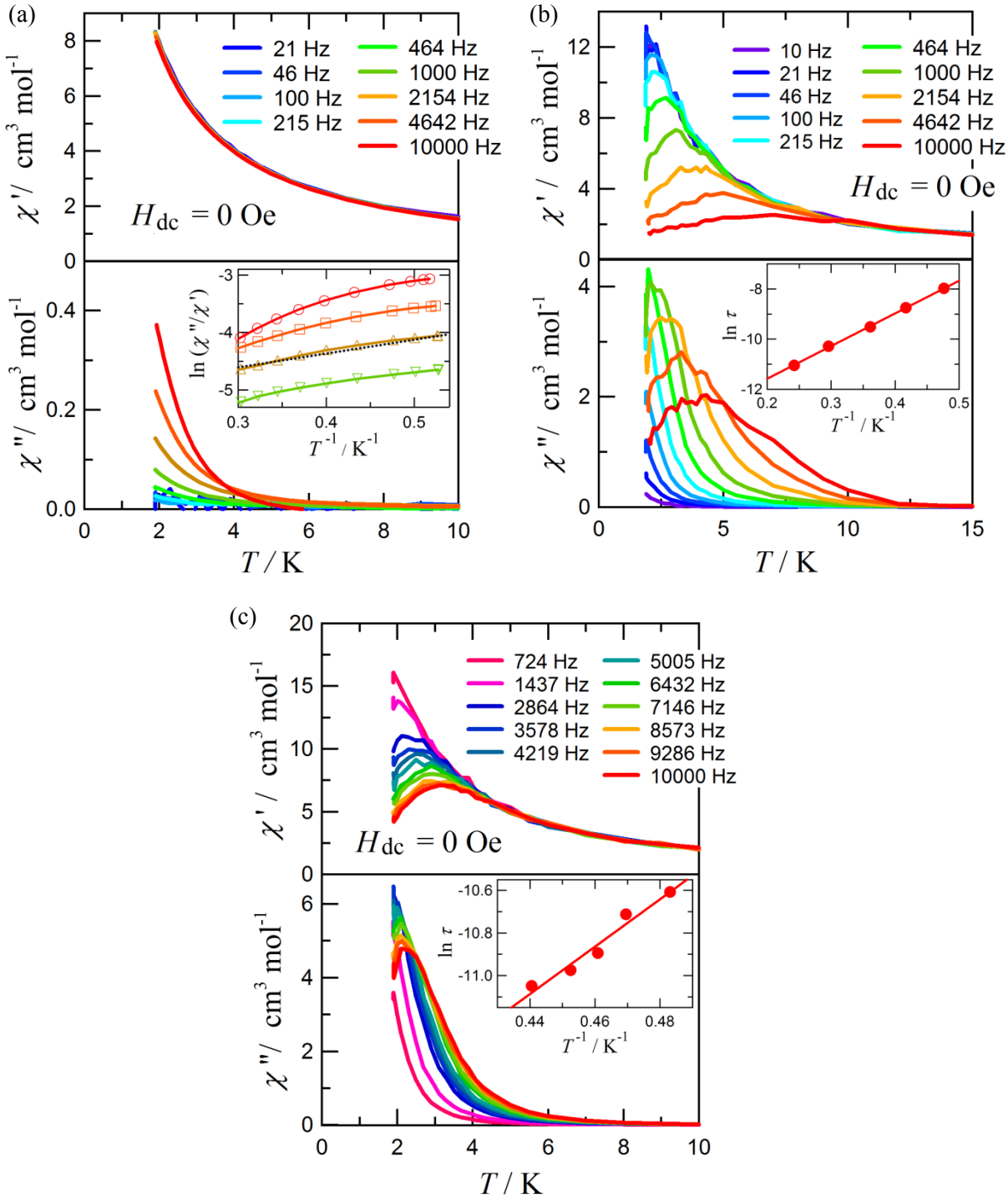

Figure 3.5. Ac magnetic susceptibilities (in-phase χ' (top) and out-of-phase χ'' (bottom)) measured for (a) **4**, (b) **5**, and (c) **6** without any dc bias field. Lines are shown as a guide to the eyes. The insets show the (modified) Arrhenius plots together with optimized lines.

The ac magnetic susceptibilities of powder specimens of **4** – **6** were measured at frequencies: ν = 10 – 10000 Hz in T = 1.9 – 20 K (Figure 3.5). Below ca. 10 K, χ' decrease and concomitant χ" increase were observed, especially for **5** and **6**, and their positions were shifted to a higher temperature on increasing frequency. The frequency dependence of the χ" peak temperature can be analyzed by the Arrhenius law;[26] namely, the plots of the natural logarithm of the relaxation time τ evaluated by $1/(2\pi\nu)$ vs. the inverse of the χ" peak temperature T (Eq. 3.1). However, owing to the absence of χ" peaks in the data of **4** (Figure 3.5a), a modified Arrhenius equation (Eq. 2.5 in Chapter 2) was applied to the analysis.[27]

$$\ln(2\pi\nu) = -\ln(\tau_0) - U_{\mathrm{eff}}/k_{\mathrm{B}}T \tag{3.1}$$

The modified Arrhenius plot for **4** and Arrhenius plots for **5** and **6** are shown in the insets of Figure 3.5. The effective energy barriers U_{eff} of the magnetization reversal and pre-exponential factors τ_0 were calculated to be $U_{\mathrm{eff}}/k_{\mathrm{B}}$ = 2.4±0.6, 13.0±0.2, and 11±1 K and τ_0 = (3.6±0.1)×10^{-7}, (6.9±0.5)×10^{-7}, and (1.1±0.7)×10^{-7} s for **4**, **5**, and **6**, respectively.

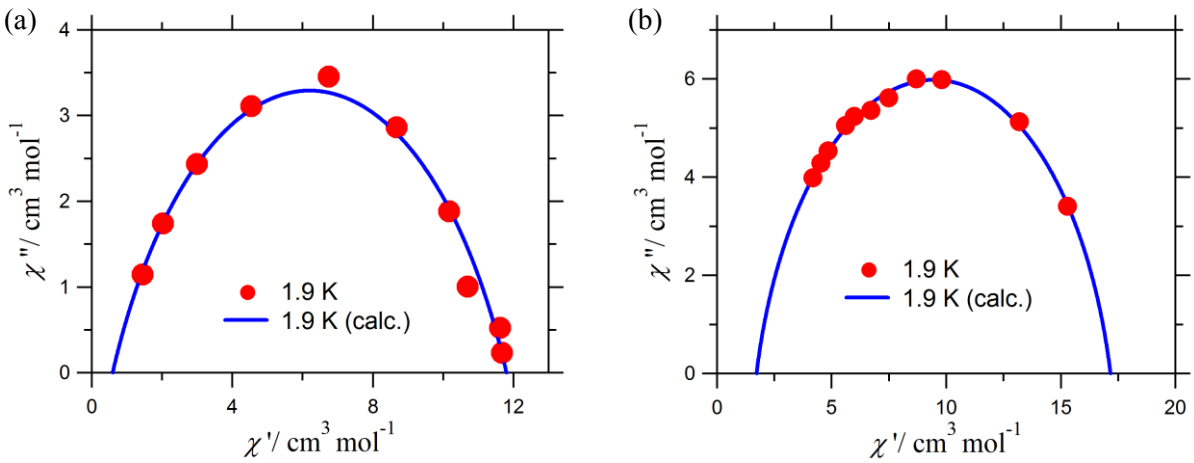

Figure 3.6. Cole-Cole plot[28] for (a) **5** and (b) **6** from the data of Figure 3.5b and 3.5c, respectively. Partial semicircles were drawn, and the optimized α values[5c] were 0.32±0.03 and 0.16±0.01, respectively, at 1.9 K.

Table 3.4. Effective energy barrier U_{eff}, pre-exponential factor τ_0, and α in the Cole-Cole analysis from the ac magnetic susceptibility measurements.

Compound	**4**	**5**	**6**
$U_{eff}k_B^{-1}$ / K	2.4±0.6	13.0±0.2	11±1
τ_0 / s	$(3.6\pm0.1)\times10^{-7}$	$(6.9\pm0.5)\times10^{-7}$	$(1.1\pm0.7)\times10^{-7}$
α at 1.9 K	- [a)]	0.32±0.03	0.16±0.01

[a)] Not determined because of a narrow range of the susceptibility data.

The Cole-Cole analysis[28] was performed for **5** and **6** using the above ac susceptibilities (see Chapter 1, Section 1.7.6). The equation $\chi(\omega) = \chi_S + (\chi_T - \chi_S)/(1 + (i\omega\tau)^{1-\alpha})$ was applied, where χ_T and χ_S are the isothermal and adiabatic magnetic susceptibilities, respectively.[5c] A semicircle with a small value of α usually indicates one relaxation process operative. Actually, these plots displayed a partial semicircle (Figure 3.6), and the optimized α values were 0.32±0.03 at 1.9 K for **5**, and 0.16±0.01 at 1.9 K for **6**. The results on ac magnetic susceptibilities are summarized in Table 3.4. The existence of the finite barriers shows that the present compounds behave as SMMs.

3.4.5 HF-EPR Study

HF-EPR spectra of a powder specimen were collected in a wide frequency range between 95 and 450 GHz at 4.2 K for **4** and **6** and at 1.7 K for **5** (Figure 3.7). In the plot, each spectrum is given as the offset corresponding to the frequency, and the resonance fields are also plotted in the same figure. Hence, the figure is the combined plot of the frequency dependence of spectra and the frequency-field relation.

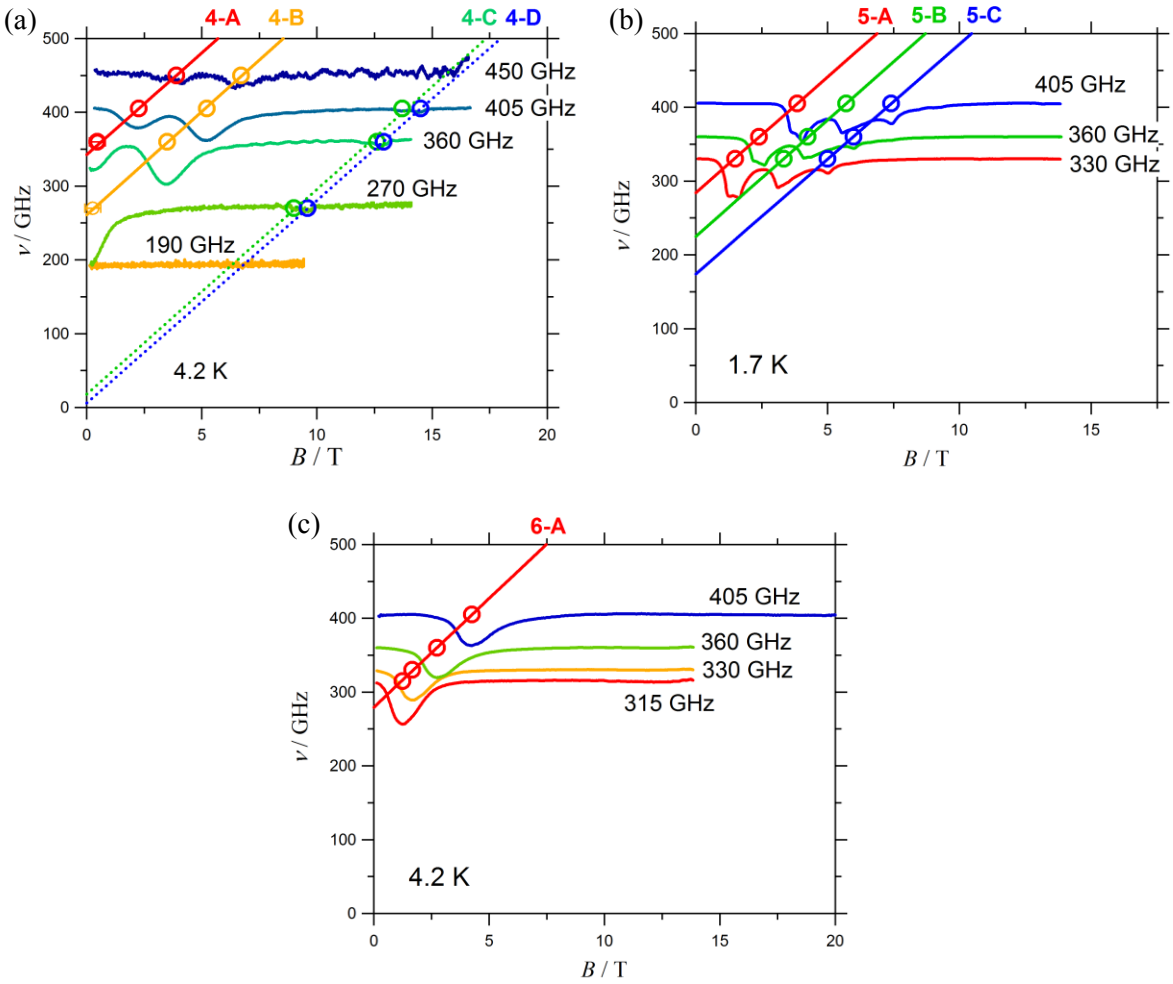

Figure 3.7. Combined plots of the spectra and the frequency-field relation for (a) **4**, (b) **5**, and (c) **6**. The temperatures are indicated inside the panels. Each spectrum is given by an offset corresponding to the frequency. Solid lines are the linear fits of the frequency-field diagrams. Small signals found in **4**, presumably caused by impurities, are indicated by the dotted lines.

Compound **4** shows two strong absorption (4-A and 4-B) and a few weak ones (4-C and 4-D), and **5** shows three strong absorptions (5-A, 5-B, and 5-C) with additional doublet structures at each signal, while **6** shows practically only one strong absorption (6-A). The slopes of the EPR modes defined as effective *g*-values are listed in Table 3.5. All of them fell in the range from 2.0±0.1 to 2.27±0.04. The intensity for all of the EPR absorption monotonically decreased with increasing temperature (Figure 3.8). This finding indicates that the absorption is assigned to the transition from the ground state or low-lying states.

Table 3.5. HF-EPR results of **4**, **5**, and **6**.

Compound	**4**		**5**			**6**
peak number	4-A	4-B	5-A	5-B	5-C	6-A
g	2.0±0.1	2.00±0.08	2.27±0.04	2.26±0.04	2.26±0.02	2.11±0.04
J^z	±15/2	±11/2	±15/2	±11/2	±9/2	±15/2
J/k_B	2.25±0.05		1.82±0.04			1.79±0.04

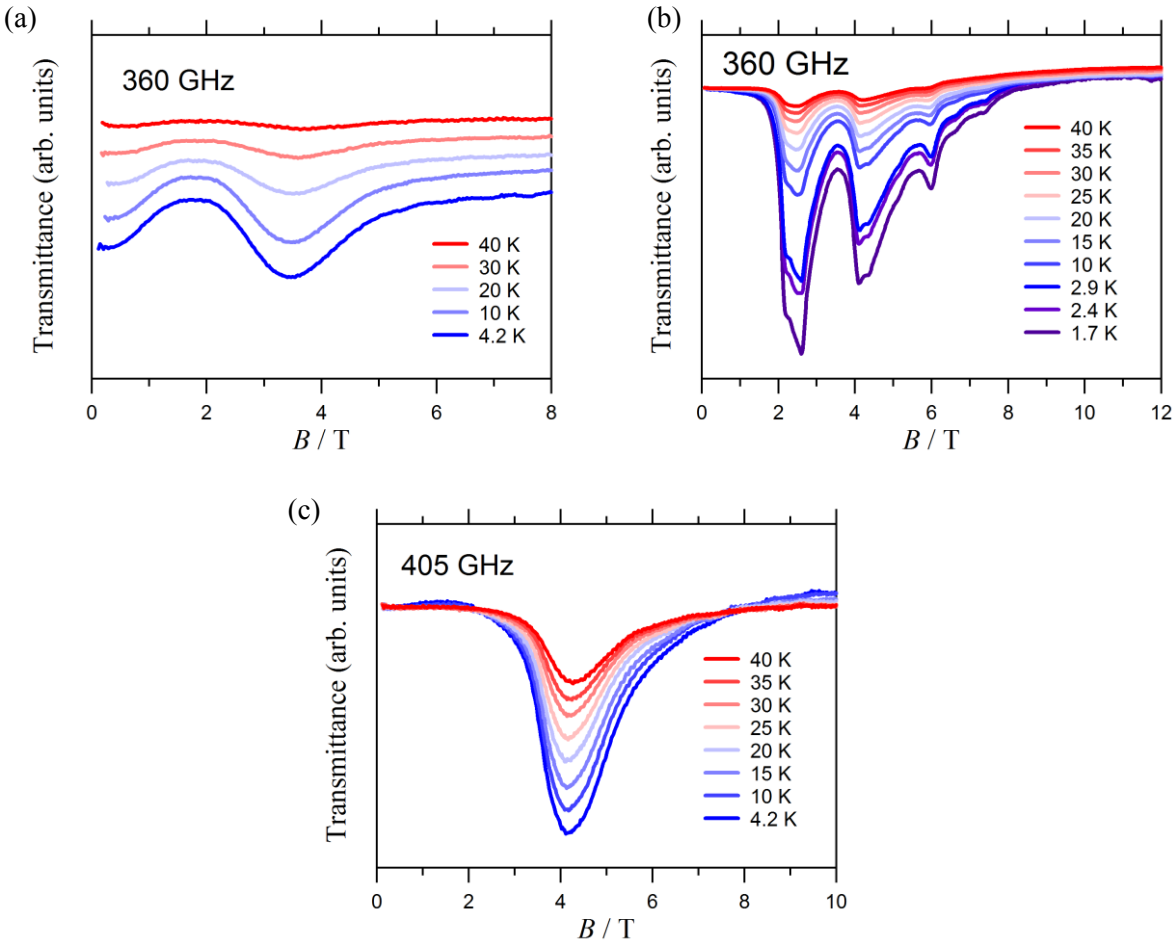

Figure 3.8. Variable-temperature HF-EPR spectra of (a) **4**, (b) **5**, and (c) **6**.

An effective g value in the $J^z = \pm 15/2$ doublets of Dy^{3+} would be 20, which is much different from the observed g-values. Hence, the signals can be assigned to Cu^{2+}-related transition biased with the exchange field between Cu^{2+} and Dy^{3+}. Strictly speaking, the reversal of Cu^{2+} spin is

forbidden EPR transition (EPR selection rules: $\Delta m_s = \pm 1$ and $\Delta S = 0$) because it is associated with the change of the total angular momentum of the exchange coupled effective moment; namely, the spin selection rules cannot be established with Ln ions of spin-orbit effect. However, transition becomes observable when the molecular symmetry is low, and the different states are mixed. Such conditions may be applicable for the present systems.

Let us explain the procedure of evaluating exchange couplings by using an energy level diagram for the simplest case of **6**. The outline of the procedure applied to system[15-17] is as follows: (1) Ln ions are treated as Ising spins. In other words, only the lowest J^F doublet of Dy^{3+} is included. This treatment can be justified when the splitting between the ground and the excited states is larger than the EPR frequencies, and the measurement was performed at low temperatures. (2) The energy level diagram was drawn by assuming the sign of 4f-3d exchange coupling and the possible EPR transitions by the reversal of 3d spins are assigned. (3) The magnitude of the exchange coupling is evaluated by adjusting the splittings of the calculated energy levels with those of the experimental data. (4) In case of antiferromagnetic exchange coupling, the level crossing in the energy level diagram is assigned to the magnetization steps. The last procedure is not used in the present case since there is no level crossing for ferromagnetically coupled molecules.

The following spin-Hamiltonian was applied:

$$\hat{H} = -J_{\mathrm{Dy-Cu1}} J_{\mathrm{Dy}}^{z} \cdot S_{\mathrm{Cu1}} - J_{\mathrm{Dy-Cu2}} J_{\mathrm{Dy}}^{z} \cdot S_{\mathrm{Cu2}} + \mu_{\mathrm{B}} H^{z} \left(g_{\mathrm{Dy}} J_{\mathrm{Dy}}^{z} + g_{\mathrm{Cu1}} S_{\mathrm{Cu1}} + g_{\mathrm{Cu2}} S_{\mathrm{Cu2}} \right). \quad (3.2)$$

Here, the first and second terms mean the exchange energy between one Dy^{3+} and two Cu^{2+} spins. The exchange coupling between two terminal Cu1⋯Cu2 is disregarded, because of the long Cu⋯Cu distance. Owing to the molecular symmetry, the condition of $J_{\mathrm{Dy-Cu1}} = J_{\mathrm{Dy-Cu2}}$ is

applied for **4** and **6**. The third term expresses the Zeeman energies of magnetic ions.

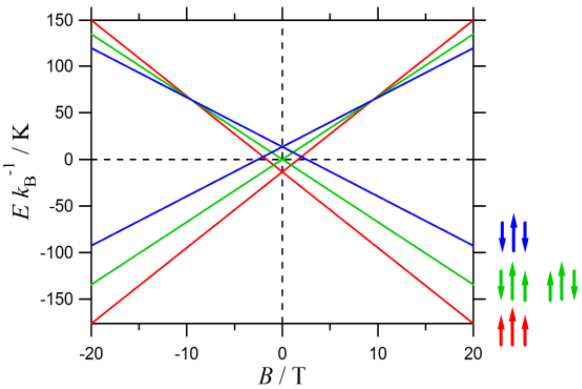

Figure 3.9. Energy levels of **6** in the ground state J^z = 15/2 manifold. The arrangement of Dy (long arrow) and Cu (short arrows) magnetic moments are schematically shown.

First, the simplest energy level diagram of **6** was analyzed to be depicted in Figure 3.9. As mentioned previously, the observed EPR signal is the transition from the ground state. Hence, the signal should be assigned to the transition between the red and green levels. Note that the green level is doubly degenerated for the presence of two identical exchange couplings. The difference between the red and green levels is expected to increase linearly with the magnetic field and the exchange coupling energy can be evaluated from the gap at zero magnetic field. These expected characteristic features are consistent with the experimentally obtained linear frequency-field diagram in Figure 3.7c. From the extrapolation of the EPR mode, the energy gap (ΔE) at zero field is evaluated to be 279±1 GHz. The $J_{\text{Dy-Cu}}$ was derived according to the relation $\Delta E = -2J_{\text{Dy-Cu}}(J^z_{\text{Dy}} \cdot S_{\text{Cu1}})$, from the first term of Eq. 3.2. The Dy–Cu exchange coupling $J_{\text{Dy-Cu}}$ was determined to be J/k_B = +1.79±0.04 K. Here, the used parameters are $S_{\text{Cu1}} = S_{\text{Cu2}} = 1/2$, $g_{\text{Cu1}} = g_{\text{Cu2}}$ = 2.11±0.04, and J^z_{Dy} = 15/2. The parameters obtained from the HF-EPR experiments are listed in Table 3.5. The level-crossing field was −9.5±0.2 T (Figure 3.9), which implies the crossing of two states with respect to the Cu spin-flip and shows degeneracy due to the symmetry. In Figure 3.7c,

the level-crossing field corresponds to the field-axis intercept with the extrapolation of line 6-A. Such a negative crossing field is not detected in magnetization curves when the exchange coupling is ferromagnetic.

Next the result of **4** was analyzed to be depicted in Figure 3.7a, and two weak absorptions (4-C and 4-D) with g = (2.0±0.2) – (1.97±0.02) were found besides the strong peaks. Since the extrapolation of these modes go to the origin of the frequency-field diagram, these are considered as Cu^{2+}-involved impurity and removed from further analysis. This content is practically negligible, as guaranteed by the PXRD data [Figure 3.1(top)].

The behavior of each of two major absorptions 4-A and 4-B of **4** is quite similar to the broad signal 6-A observed for **6**. There are two possible interpretations for the observation of two EPR modes. The first one is the existence of two non-equivalent Dy–Cu exchange couplings, or in other words the case of $J_{\text{Dy-Cu1}} \neq J_{\text{Dy-Cu2}}$. However, it is unlikely for **4**, because the crystallographic analysis clarified that the two Dy–Cu bonds are identical.

Alternative interpretation is that the two signals originate from the admixture of two kinds of J^z doublets of Dy^{3+} ion in the ground-state wave function. According to Eq. 3.3, the ratio of the zero field energy values of two modes should scale with J^z. The ratio of zero field energy is 261±6 GHz / 347±2 GHz = 0.75 is close to the ratio of J^z's, (11/2)/(15/2) = 0.73. The matching of the theoretical and experimental ratios indicates that the second interpretation is more plausible. In 4f-electron systems, the mixing of the J^z states happens in low-symmetry molecules through the spin-orbit coupling and CFS. There are some known Dy^{3+} compounds with a ground J^z = ±11/2 state,[29] in which a two-fold symmetry was characterized like **4**.[30] It also supports that the two EPR modes found in **4** are originated from the mixture of two J^z states. The exchange coupling is thus determined to be $J_{\text{Dy-Cu}}/k_B$ = 2.25±0.05 K. The determined Zeeman diagrams for J^z_{Dy} = ±15/2 and ±11/2 are shown in Figure 3.10.

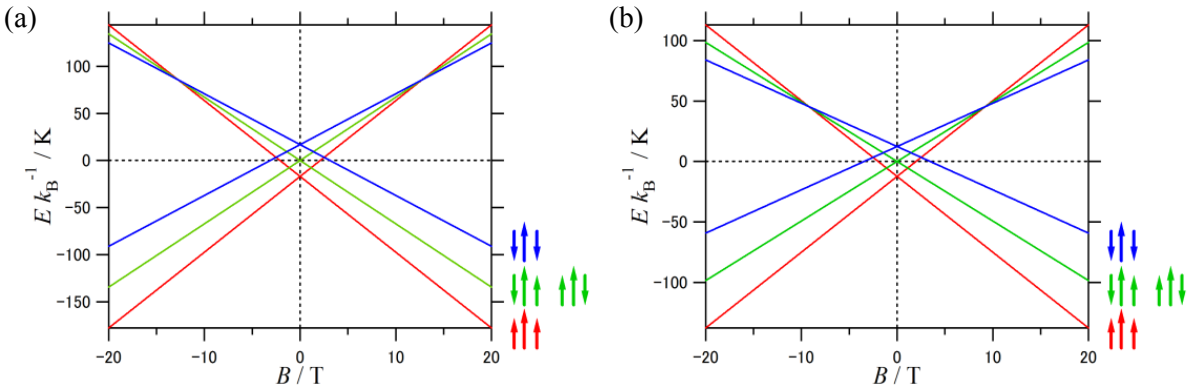

Figure 3.10. Energy levels of **4** with $J^{\mathcal{F}}$ = 15/2 (a) and $J^{\mathcal{F}}$ = 11/2 (b) for Dy^{3+}. The arrangement of Dy (long arrow) and Cu (short arrows) magnetic moments are schematically shown.

Finally, the data of **5** were analyzed to be depicted in Figure 3.7b. There are two Cu^{2+} sites in the crystal of **5**, and thus $J_{Dy\text{-}Cu1} \neq J_{Dy\text{-}Cu2}$ could give two modes. However, the number of absorptions is more than expected. The phase purity is assured by the PXRD data [Figure 3.1(bottom)]. In this case, it must be considered to be the admixture of the multiple $J^{\mathcal{F}}$ states in the ground state. The zero field energies of the three groups are 285±6, 225±3, and 174±2 GHz, and the ratio is 1/0.79/0.61, being close to the ratio 1/0.73/0.60 from $J^{\mathcal{F}}$ = ±15/2, ±11/2, and ±9/2. Hence, the splitting into three major groups are due to the mixing of three $J^{\mathcal{F}}$ doublets in the ground state, and the small splitting within each group is caused by the non-equivalent Dy–Cu exchange interactions. The almost equal intensity between the two peaks of the each group is consistent with the small variation of the exchange couplings at two independent cites in a unit cell. The g values of the signals were 2.1±0.1 and 2.24±0.04. They have evaluated the two exchange coupling parameters $J_{Dy\text{-}Cu1}/k_B$ =1.87±0.02 K and $J_{Dy\text{-}Cu2}/k_B$ = 1.79±0.01 K, which are different from each other by 4%. The zero field energy of 285±6 GHz is an average value from the two distinct energies. The exchange coupling parameter was determined to $J_{Dy\text{-}Cu}/k_B$ = 1.82±0.04 K for **5** (Table 3.4). The determined Zeeman diagrams for $J^{\mathcal{F}}_{Dy}$ = ±15/2, ±11/2, and ±9/2 are shown in Figure 3.11.

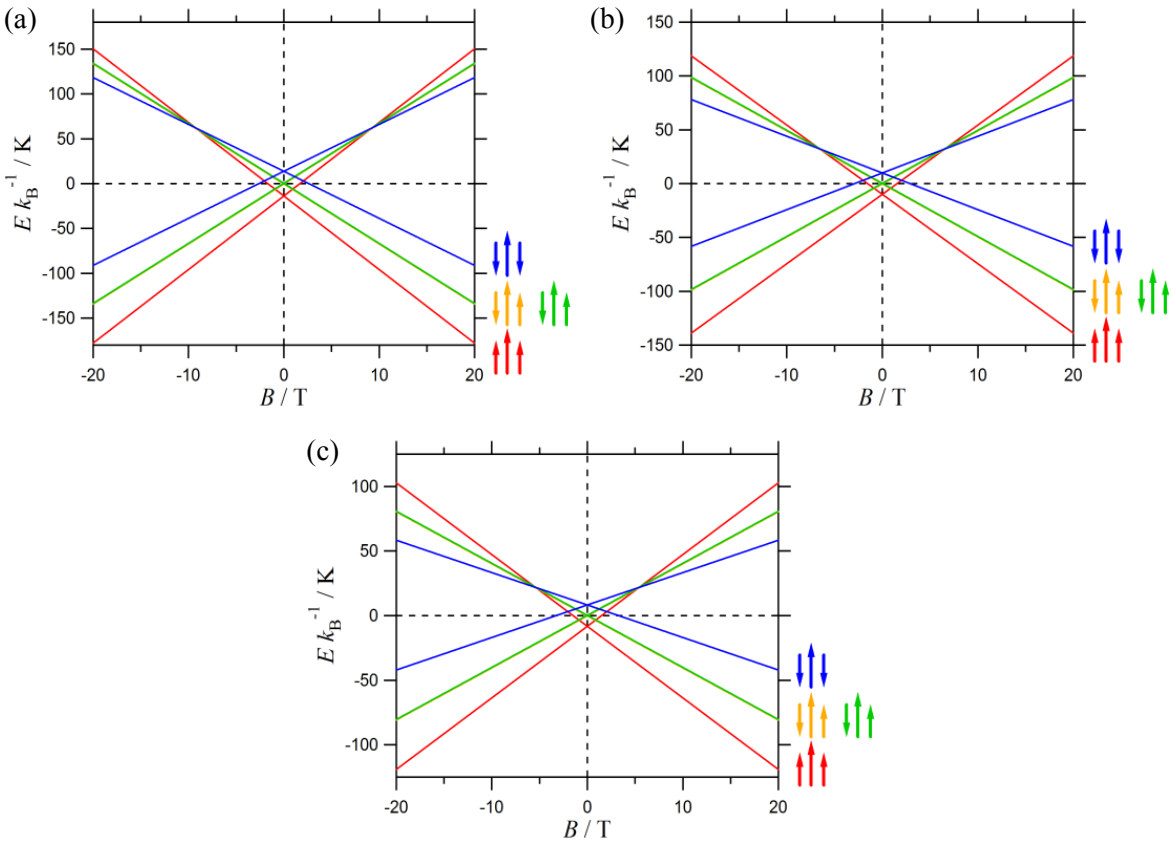

Figure 3.11. Energy levels of **5** with $\mathcal{J} = \pm 15/2$ (a), $\mathcal{J} = \pm 11/2$ (b), and $\mathcal{J} = \pm 9/2$ (c) for Dy^{3+}. The arrangement of Dy (long arrow) and Cu (short arrows) magnetic moments are schematically shown.

The HF-EPR analysis elucidated not only the Dy–Cu exchange coupling, but also the mixing of the Dy^{3+} ground-state wave functions. Even a tiny variation of exchange couplings for the non-equivalent bonds can be resolved clearly. Such quantitative and precise determination of the exchange coupling highlights the powerfulness of the HF-EPR.

3.5 Discussion

Now let us discuss the magneto-structure relation for the series of Dy–Cu compounds. To expand the parameter survey range, the data of two known compounds **A** ($[Cu^{II}(L^A)(C_3H_6O)Dy^{III}(NO_3)_3]$; H_2L^A = *N*,*N*'-bis(3-methoxysalicylidene)-1,3-diamino-2,2-dimethylpropane)[17] and **B** ($[Dy^{III}L^B{}_2(NO_3)_2\{Cu^{II}(CH_3OH)\}_2](NO_3)(CH_3OH)$; H_2L^B =

2,6-bis(acetylaceto)pyridine)[16] with analogous DyO_2Cu structures are included into the discussion. Table 3.6 summarizes the exchange coupling constants $J_{Dy\text{-}Cu}$ together with the geometrical parameters. Here the Cu–Dy–Cu hinge angles were ignored in this analysis, thus affording simplified discussion on the two-spin systems. In the following analysis, the averaged value of two exchange couplings in **5** and **B** were used, because of the uncertainty of the assignment of two exchange couplings to two Cu sites. It is found that the exchange coupling of **4** is the largest and twice as large as that of **B**. While, the values of **5** and **6** are only slightly larger than that of **A**.

Table 3.6. Exchange parameter $J_{Dy\text{-}Cu}$ for the DyO_2Cu compounds determined from the HF-EPR study and important geometrical parameters.

Compound	**4**	**5**	**6**	**A**[e)]	**B**[f)]
$J_{Dy\text{-}Cu}k_B^{-1}$ / K	2.25±0.05	1.82±0.04	1.79±0.04	1.63±0.01	0.90±0.01
coordination number	10	9	10	10	8
Dy–O[a)] / Å	2.370±0.002	2.40±0.06	2.382±0.006	2.367±0.005	2.52±0.03
Cu–O[a)] / Å	1.948±0.004	1.95±0.02	1.9755±0.0005	1.957±0.001	1.932±0.003
θ [b)] / °	99.3±0.2	99.8±2.0	100.5±0.2	108.2±0.2	109.5±0.8
ϕ [c)] / °	140.9±0.1	147.4±1.6	142.4±0.2	162.7±0.1	179.1±0.8
d [d)] / Å	3.301±0.001	3.33±0.02	3.358±0.001	3.510±0.003	3.65±0.01

[a)] The averaged bond length in the DyO_2Cu unit(s). [b)] The averaged Dy–O–Cu bond angle. [c)] The Dy–O···O–Cu "butterfly" angle. For **5** and **B**, averaged values are applied. [d)] The Dy···Cu distance. For **5** and **B**, averaged values are applied. [e)] From ref. 16. [f)] From ref. 15.

At the first stage, they investigated the relationship between the coordination number (CN) of the Dy^{3+} ion and the Dy–O bond length. Figure 3.12a shows the normalized Dy–O bond length against the CN. The Dy–O bond length of the CN = 8 subset is longer than those of the CN = 10 subset by ca. 6 %. It is quite unusual, because in general an increase of CN enlarges the ionic

radius.[31] A possible reason for the present anomaly may reside in the rigid coordination structure of **B**, where the Dy^{3+} ion is surrounded by a compartment metalloligand or metallacrown[32] $[L^B{}_2Cu^{II}{}_2]$. The resultant structure is highly planar and loses the configurational freedom. The Dy–O distance is thus regulated by the $[L^B{}_2Cu^{II}{}_2]$ structure itself regardless of CN. Discussion using CN requires a special attention.

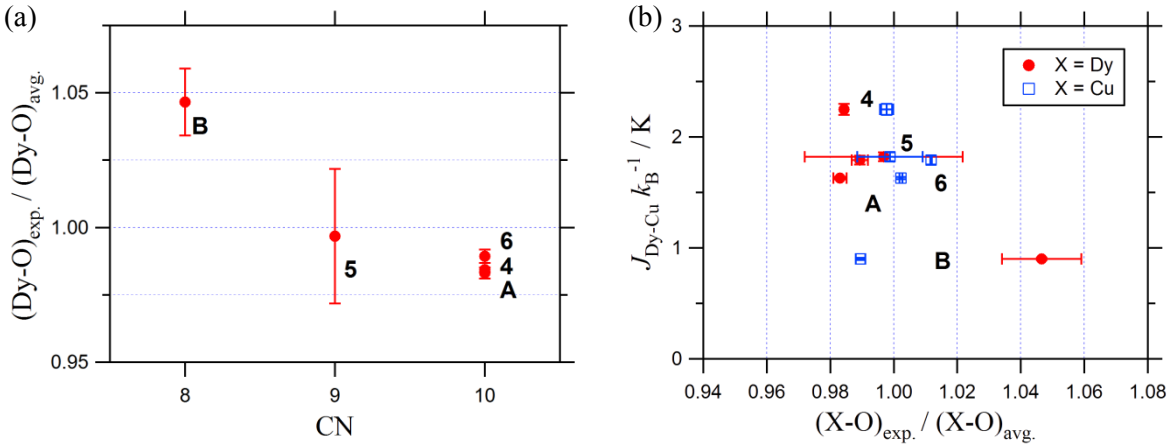

Figure 3.12. (a) Plot of the normalized Dy–O bond length against the coordination number (CN) of Dy ion. (b) Plot of the exchange coupling and two normalized bond lengths of Dy–O and Cu–O.

Next, the exchange coupling was plotted against the bond lengths of Dy–O and Cu–O averaged in the DyO_2Cu core structure, as shown in Figure 3.12b. Compound **4** has O5 at an axial position of Cu1, and **5** also has O3 at an axial site of Cu1 (see above). The contribution of the Dy1–O(axial) –Cu1 pathways is ignorable. The exchange coupling is insensitive to the Cu–O bond lengths but seems to depend slightly on the Dy–O bond lengths. Compound **B** with the longest Dy–O distance gives the weakest exchange coupling. Another relation between the exchange coupling and the Dy···Cu interatomic distance (Figure. 3.14) also exhibits that the shorter distance favors the stronger exchange coupling.

The plot of exchange coupling against the Dy–O–Cu bond angle is shown in Figure 3.13a.

The angle is the average of the double oxygen paths. They found that the bond angles are split into two regimes around 100° and 109°. The average of exchange couplings of three samples in the former regime is larger than the average in the latter regime. As a general trend of the Gd–Cu case, the exchange coupling decreases with increasing Gd–O–Cu bond angles, while exchange coupling does not much depend on the Cu–O bond length.[13,33] In the framework of the superexchange mechanism, the exchange coupling between Dy and Cu depends on the orbital overlap and the orthogonality in the Dy–O–Cu bond. The Dy–O–Cu angle may have a clue to the exchange coupling mechanism. At the present stage; however, cautious analysis is needed for further discussion because of the narrow range of the bond angle.

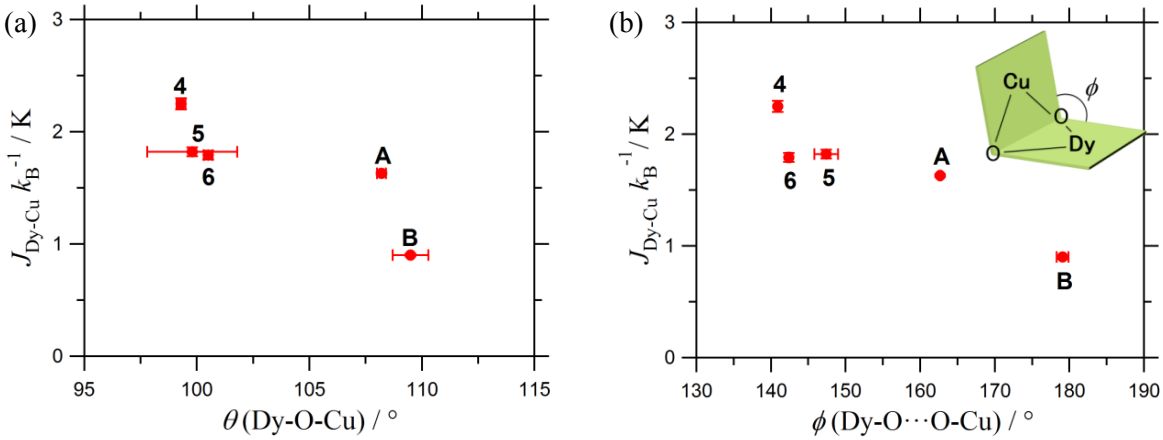

Figure 3.13. Plots of the Dy–Cu exchange parameters in five DyO_2Cu compounds (a) as a function of θ (Dy–O–Cu) and (b) as a function of ϕ (Dy–O···O–Cu).

Finally, the author discusses the effect of the geometrical parameter governing the skeleton of the molecule. In Figure 3.14, the exchange parameter is plotted against the Dy···Cu distance. Since the Dy···Cu distance becomes shorter when the Dy–O–Cu bond angle is smaller, the plot is related to Figure 3.13a. Furthermore, the plot of the exchange parameter vs. the Dy–O bond length shown in Figure 3.12b is also related to Figure 3.13a. As cited above, it is well known that $J_{Gd\text{-}Cu}$ value shows a relation with the "butterfly" angle ϕ.[11-13] The largest J/k_B = 18.1 K was

characterized for $\phi = 178.39°$, and a smaller $J/k_B = 0.6$ K was obtained for $\phi = 147.01°$. A general trend in the relation between $J_{Dy\text{-}Cu}$, and ϕ is also recognized, but the profile is quite different (Figure 3.13b). This trend may be understood in two ways. First, the change of ϕ causes the change of the Dy–O–Cu bond angle. Another possibility is that the overlap/orthogonality of the Dy–O–Cu bond varies with ϕ. These two can be understood by considering the change of bonding with spatial extension and direction of lanthanide wave functions. Although the exchange coupling must be related to the local structure of each bond; namely, the bond lengths and the bond angles, the "butterfly" angle may be useful to discuss the whole DyO_2Cu skeleton of the molecule holding the larger exchange couplings.

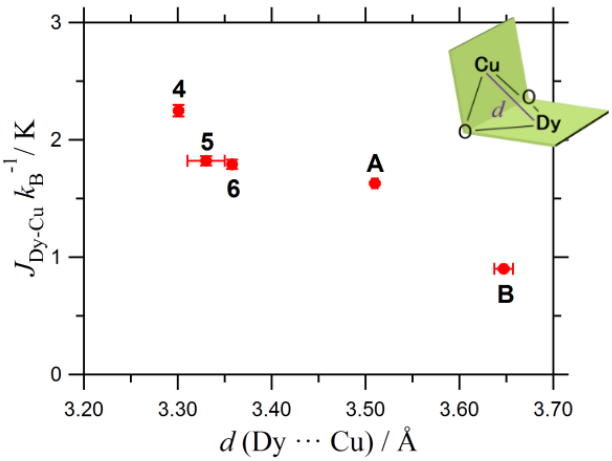

Figure 3.14. Plot of the Dy–Cu exchange parameter as a function of d(Dy···Cu).

Although the 4f orbitals of Dy and Gd are different, the calculation results of the Gd–Cu complexes might be helpful. According to Kahn et al.,[37] they proposed the mechanism of ferromagnetic coupling by the overlap of empty 5d orbital of the Gd^{3+} ion and 3d orbital of unpaired electron of the Cu^{2+} ions. The overlap of the unpaired electron transferred to the 5d orbital brings about the parallel alignment of the 4f and 5d electrons in the Gd^{3+} ion by Hund's rule. On the other hand, orbital overlaps between the singly occupied molecular orbitals belonging

to Gd^{3+} and Cu^{2+} ions give rise to antiferromagnetic interaction. The exchange coupling value is determined by the total of the contribution of ferromagnetic and antiferromagnetic interactions. A few calculation works[34-36] support this logic. In the case of Dy^{3+}–Cu^{2+} systems, two 4f orbitals are doubly occupied while five remain singly occupied. The role of 4f (Dy^{3+}) – 3d (Cu^{2+}) overlaps may contribute to a ferromagnetic term as well as antiferromagnetic one. A short Dy···Cu distance does not always afford preference for antiferromagnetic interaction.

For the magneto-structure relation in the Dy–O···O–Cu "butterfly" compounds, the bent configuration seems to favor ferromagnetic interaction. There are ample examples of Dy–Cu heterometallic complexes having "cubane", "semicubane", and "fused cubane" skeletons. Actually ferromagnetic interactions have been reported in the Co_2Dy_2 and Ni_2Fe_2 compounds having a "defective dicubane" motif.[38] The Co–O–Dy and Ni–O–Dy bond angles range in (97.2±0.1) – (107.0±0.1) and (96.6±0.1) – (106.9±0.1)°, respectively.[38] The wide variation of geometries as well as variation of 3d ions and 4f ions will be a subject to future studies.

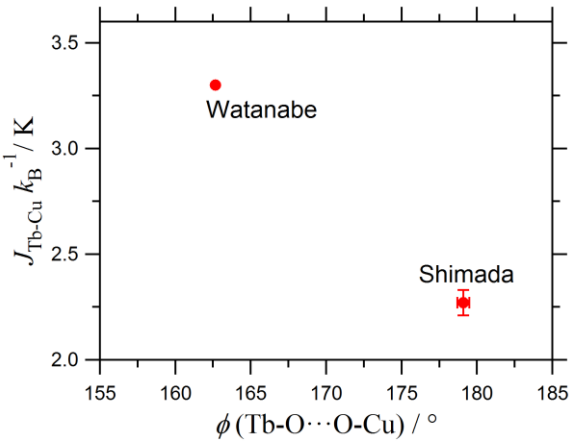

Figure 3.15. Plot of the Tb–Cu exchange parameters in two TbO_2Cu compounds as a function of ϕ(Tb–O···O–Cu). The data are taken from the references.[15,16]

The present work gives the first detailed investigation of magneto-structure relations based on the precise determination of exchange coupling in Ln–Cu compounds, where Ln is other than

Gd. Although the number of reported examples is very small, the author carried out preliminary examination on the $TbCu_2$ compounds.[15,16] Watanabe and co-workers reported $J_{Tb\text{-}Cu}$ in $[Cu^{II}(L^A)(C_3H_6O)Tb^{III}(NO_3)_3]$,[16] and Shimada and co-workers in $[Tb^{III}L^B{}_2(NO_3)_2\{Cu^{II}(CH_3OH)\}_2](NO_3)(CH_3OH)$[15] with analogous DyO_2Cu structures. The exchange coupling parameter $J_{Tb\text{-}Cu}$ is plotted against the "butterfly" angle (Figure 3.15). A similar trend can be seen; the bent "butterfly" structure favors strong ferromagnetic coupling.

3.6 Conclusion

Three novel Dy–Cu SMM have the structural diversity of hinge-like coordination flexibility, indicating large ferromagnetic exchange coupling. The followings were clarified. (1) New molecular structures can be obtained by the control of solvent. (2) The strong exchange couplings are caused by the double bridge structure. (3) HF-EPR is a unique method to determine the exchange coupling and the state of the rare earth ions, affording the $J_{Dy\text{-}Cu}$ values in 1.79±0.04 – 2.25±0.05 K for **4** – **6**. Before the author group's work, there have been only two reports on the precise determination of the $J_{Dy\text{-}Cu}$ parameters.[15,16] The present $J_{Dy\text{-}Cu}$ values are larger than those of the previous reports. (4) It was examined to relate the exchange coupling parameters with the structural parameters in three present and two additional compounds. The results showed relationships between bond angles and "butterfly" angles against the exchange couplings. The "butterfly" angle representing the DyO_2Cu skeleton is a simple but a useful parameter to predict the strength of exchange couplings.

The present work gives the first detailed investigation of magneto-structure relation based on the precise determination of exchange coupling in Dy–Cu compounds. Such relationship allows us to draw molecular design and improve the magnetic exchange coupling in various molecule-based magnets, including "cubane" and "semicubane" structures often found in SMMs. Moreover, doubly oxygen-bridged motifs are commonly found in metal oxides, so that the present

compounds might be regarded as minimum exchange-coupled models or prototypes for polymeric oxide-based magnets. Although the explanation has to wait for theoretical treatment, empirical magneto-structural relation will be applied to design 4f-3d-based magnetic materials. The method for the estimation of exchange coupling by means of HF-EPR is unique approach developed by the group to which the author belongs. The above examples indicate the generality of this method and will be applied to a wide variety of Ln–Cu heteronuclear systems. Establishing the relationship of the exchange couplings and structures will afford an important guide to improve performance of SMMs as well as other types of 4f-3d based magnets.

References

(1) S. Osa, T. Kido, N. Matsumoto, N. Re, A. Pochaba, J. Mrozinski, *J. Am. Chem. Soc.* **2004**, *126*, 420.

(2) (a) F. Mori, T. Nyui, T. Ishida, T. Nogami, K.-Y. Choi, H. Nojiri, *J. Am. Chem. Soc*. **2006**, *128*, 1440; (b) S. Ueki, T. Ishida, T. Nogami, K.-Y. Choi, H. Nojiri, *Chem. Phys. Lett.* **2007**, *440*, 263.

(3) F. Pointillart, K. Bernot, R. Sessoli, D. Gatteschi, *Chem. Eur. J.* **2007**, *13*, 1602.

(4) N. Ishikawa, M. Sugita, T. Ishikawa, S.-y. Koshihara, Y. Kaizu, *J. Am. Chem. Soc.* **2003**, *125*, 8694.

(5) (a) J. D. Reinhart, J. R. Long, *Chem. Sci.* **2011**, *2*, 2078; (b) D. N. Woodruff, W. R. E. P. Winpenny, R. A. Layfield, *Chem. Rev.* **2013**, *113*, 5110; (c) R. Sessoli, A. K. Powell, *Coord. Chem. Rev.* **2009**, *253*, 2328; (d) M. Andruh, J. P. Costes, C. Diaz, S. Gao, *Inorg. Chem.* **2009**, *48*, 3342; (e) P. H. Lin, T. J. Burchell, L. Ungur, L. F. Chibotaru, W. Wernsdorfer, M. Murugesu, *Angew. Chem.*, *Int. Ed.* **2009**, *48*, 9489; (f) J. D. Rinehart, M. Fang, W. J. Evans, J. R. Long, *Nature Chem.* **2011**, *3*, 538; (g) H. L. C. Feltham, S. Brooker, *Coord. Chem. Rev.* **2014**, *276*, 1; (h) P. Zhang, L. Zhang, C. Wang, S. F. Xue, S. Y. Lin, J. K. Tang, *J. Am. Chem. Soc.* **2014**, *136*, 4484.

(6) (a) S. Yamauchi, T. Fujinami, N. Matsumoto, N. Mochida, T. Ishida, Y. Sunatsuki, M. Watanabe, M. Tsuchimoto, C. Coletti, N. Re, *Inorg. Chem.* **2014**, *53*, 5961; (b) M. Towatari, K. Nishi, T. Fujinami, N. Matsumoto, Y. Sunatsuki, M. Kojima, N. Mochida, T. Ishida, N. Re, J. Mrozinski, *Inorg. Chem.* **2013**, *52*, 6160.

(7) (a) A. Bencini, C. Benelli, A. Caneschi, R. I. Carlin, A. Dei, D. Gatteschi, *J. Am. Chem. Soc.* **1985**, *107*, 8128; (b) N. Matsumoto, M. Sakamoto, H. Tamaki, H. Okawa, S. Kida, *Chem. Lett.* **1990**, *19*, 853; (c) O. Guillow, P. Bergerat, O. Kahn, E. Bakalbassis, K. Boubekeur, P. Batail, M. Guillot, *Inorg. Chem.* **1992**, *31*, 110.

(8) M. Andruh, I. Ramade, E. Codjovi, O. Guillou, O. Kahn, J. C. Trombe, *J. Am. Chem. Soc.* **1993**, *115*, 1822.

(9) (a) J.-P. Costes, F. Dahan, A. Dupuis, *Inorg. Chem.* **2000**, *39*, 5994; (b) J.-P. Costes, F. Dahan, A. Dupuis, J.-P. Laurent, *Inorg. Chem.* **2000**, *39*, 169; (c) J.-P. Costes, F. Dahan, A. Dupuis, J.-P. Laurent, *Chem. Eur. J.* **1998**, *4*, 1616.

(10) (a) T. Kido, Y. Ikuta, Y. Sunatsuki, Y. Ogawa, N. Matsumoto, N. Re, *Inorg. Chem.* **2003**, *42*, 398; (b) M. Evangelisti, M. L. Kahn, J. Bartolome, L. J. de Jongh, C. Meyers, J. Leandri, Y. Leroyer, C. Mathoniere, *Phys. Rev. B* **2003**, *68*, 184405.

(11) J.-P. Costes, F. Dahan, A. Dupuis, *Inorg. Chem.* **2000**, *39*, 165.

(12) I. Ramade, O. Kahn, Y. Jeannin, F. Robert, *Inorg. Chem.* **1997**, *36*, 930.

(13) M. Ryazanov, V. Nikiforov, F. Lloret, M. Julve, N. Kuzmina, A. Gleizes, *Inorg. Chem.* **2002**, *41*, 1816.

(14) (a) A. Okazawa, T. Nogami, H. Nojiri, T. Ishida, *Chem. Mater.* **2008**, *20*, 3110; (b) M. L. Baker, T. Tanaka, R. Murakami, S. Ohira-Kawamura, K. Nakajima, T. Ishida, H. Nojiri, *Inorg. Chem.* **2015**, *54*, 5732.

(15) T. Shimada, A. Okazawa, N. Kojima, S. Yoshii, H. Nojiri, T. Ishida, *Inorg. Chem.* **2011**, *50*, 10555.

(16) T. Ishida, R. Watanabe, K. Fujiwara, A. Okazawa, N. Kojima, G. Tanaka, S. Yoshii, H, Nojiri, *Dalton Trans.* **2012**, *41*, 13609.

(17) (a) S. Ueki, A. Okazawa, T. Ishida, T. Nogami, H. Nojiri, *Polyhedron* **2007**, *26*, 1970; (b) A. Okazawa, T. Nogami, H. Nojiri, T. Ishida, *Inorg. Chem.* **2008**, *47*, 9763; (c) A. Okazawa, T. Nogami, H. Nojiri, T. Ishida, *Inorg. Chem.* **2009**, *48*, 3292; (d) A. Okazawa, R. Watanabe, H. Nojiri, T. Nogami, T. Ishida, *Polyhedron* **2009**, *28*, 1808; (e) A. Okazawa, R. Watanabe, M. Nezu, T. Shimada, S. Yoshii, H. Nojiri, T. Ishida, *Chem. Lett.* **2010**, *39*, 1331; (f) A. Okazawa, K. Fujiwara, R. Watanabe, N. Kojima, S. Yoshii, H. Nojiri, T. Ishida, *Polyhedron*

2011, *30*, 3121; (g) R. Watanabe, K. Fujiwara, A. Okazawa, G. Tanaka, S. Yoshii, H. Nojiri, T. Ishida, *Chem. Commun.* **2011**, *47*, 2110; (h) K. Fujiwara, A. Okazawa, G. Tanaka, S. Yoshii, H. Nojiri, T. Ishida, *Chem. Phys. Lett*. **2012**, *530*, 49; (i) A. Okazawa, T. Shimada, N. Kojima, S. Yoshii, H. Nojiri, T. Ishida, *Inorg. Chem.* **2013**, *52*, 13351.

(18) T. Kajiwara, M. Nakano, S. Takaishi, M. Yamashita, *Inorg. Chem.* **2008**, *47*, 8604.

(19) (a) K. Liu, W. Shi, P. Cheng, *Coord. Chem. Rev.* **2015**, *289–290*, 74; (b) L. Rosado Piquer, E. C. Sañudo, *Dalton Trans.* **2015**, *44*, 8771.

(20) (a) S. Ghosh, Y. Ida, T. Ishida, A. Ghosh, *Cryst. Growth Des.* **2014**, *14*, 2588; (b) A. Bencini, C. Benelli, A. Caneschi, R. L. Carlin, A. Dei, D. Gatteschi, *J. Am. Chem. Soc.* **1985**, *107*, 8128; (c) D. W. Harrison, J.-C. G. Bünzli, *Inorg. Chim. Acta* **1985**, *109*, 185; (d) A. Bencini, C. Benelli, A. Caneschi, A. Dei, D. Gatteschi, *Inorg. Chem.* **1986**, *25*, 572; (e) S. Ghosh, S. Biswas, A. Bauza, M. Barcelo-Oliver, A. Frontera, A. Ghosh, *Inorg. Chem.* **2013**, *52*, 7508.

(21) Y. Ida, S. Ghosh, A. Ghosh, H. Nojiri, T. Ishida, *Inorg. Chem.* **2015**, *54*, 9543.

(22) (a) L. K. Das, S.-W. Park, S. J. Cho, A. Ghosh, *Dalton Trans.* **2012**, *41*, 11009; (b) S. Ghosh, G. Aromí, P. Gamez, A. Ghosh, *Eur. J. Inorg. Chem.* **2014**, *2014*, 3341; (c) A. Hazari, L. K. Das, A. Bauzá, A. Frontera, A. Ghosh, *Dalton Trans.* **2014**, *43*, 8007; (d) A. Hazari, L. K. Das, R. M. Kadam, A. Bauzá, A. Frontera, A. Ghosh, *Dalton Trans.* **2015**, *44*, 3862; (e) L. K. Das, C. J. Gómez-García, A. Ghosh, *Dalton Trans.* **2015**, *44*, 1292.

(23) A. Ruiz-Martínez, S. Alvarez, *Chem. Eur. J.* **2009**, *15*, 7470.

(24) (a) V. Tudor,V. Kravtsov, M. Julve, F. Lloret, Y. A. Simonov, J. Lipkowski, V. Buculei, M. Andruh, *Polyhedron* **2001**, *20*, 3033; (b) V. Bellini, G. Lorusso, A. Candini, W. Wernsdorfer, T. B. Faust, G. A. Timco, R. E. P. Winpenny, M. Affronte, *Phys. Rev. Lett.* **2011**, *106*, 227205; (c) I. Castro, J. Sletten, M. L. Calatayud, M. JuIve, J. Cano, F. Lloret, A. Caneschi, *Inorg. Chem.* **1995**, *34*, 4903.

(25) M. L. Kahn, C. Mathoniere, O. Kahn, *Inorg. Chem.* **1999**, *38*, 3692.

(26) (a) R. Sessoli, H.-L. Tsai, A. R. Schake, S. Wang, J. B. Vincent, K. Folting, D. Gatteschi, G. Christou, D. N. Hendrickson, *J. Am. Chem. Soc.* **1993**, *115*, 1804; (b) D. Gatteschi, R. Sessoli, J. Villain, *Molecular Nanomagnets*; Oxford University Press: New York, **2006**.

(27) J. Bartolomé, G. Filoti, V. Kuncser, G. Schinteie, V. Mereacre, C. E. Anson, A. K. Powell, D. Prodius, C. Turta, *Phys Rev. B* **2009**, *80*, 014430.

(28) K. S. Cole, H. R. Cole, *J. Chem. Phys.* **1941**, *9*, 341.

(29) (a) C. Ritchie, M. Speldrich, R.-W. Gable, L. Sorace, P. Kögerler, C. Boskovic, *Inorg. Chem.* **2011**, *50*, 7004; (b) M. A. Al Damen, S. Cardona-Serra, J. M. Clemente-Juan, E. Coronado, A. Gaita-Ariño, C. Marti-Gastaldo, F. Luis, O. Montero, *Inorg. Chem.* **2009**, *48*, 3467.

(30) E. Lucaccini, L. Sorace, M. Perfetti, J.-P. Costes, R. Sessoli, *Chem. Commun.* **2014**, *50*, 1648.

(31) (a) R. D. Shannon, C. T. Prewitt, *Acta Crystallogr.*, *Sect. B* **1969**, *25*, 925; (b) R. D. Shannon, *Acta Crystallogr.*, *Sect. A* **1976**, *32*, 751.

(32) G. Mezei, C. M. Zaleski, V. L. Pecoraro, *Chem. Rev.* **2007**, 107, 4933.

(33) J. Cirera, E. Ruiz, *C. R. Chimie* **2008**, *11*, 1227.

(34) (a) G. Rajaraman, F. Totti, A. Bencini, A. Caneschi, R.Sessoli, D. Gatteschi, *Dalton Trans.* **2009**, 3153; (b) J. Paulovič, F. Cimpoesu, M. Ferbinteanu, K. Hirano, *J. Am. Chem. Soc.* **2004**, *126*, 3321.

(35) S. K. Singh, N. K. Tibrewal, G. Rajaraman, *Dalton Trans.* **2011**, *40*, 10897.

(36) S. K. Singh, G. Rajaraman, *Dalton Trans.* **2013**, *42*, 3623.

(37) M. Andruh, I. Ramade, E. Codjovi, O. Guillou, O. Kahn J. C. Trombe, *J. Am. Chem. Soc.* **1993**, *115*, 1822.

(38) (a) K. C. Mondal, G. E. Kostakis, Y. Lan, W. Wernsdorfer, C. E. Anson, A. K. Powell, *Inorg. Chem.* **2011**, *50*, 11604; (b) K. C. Mondal, A. Sundt, Y. Lan, G. E. Kostakis, O. Waldmann, L. Ungur, L. F. Chibotaru, C. E. Anson, A. K. Powell, *Angew. Chem.*, *Int. Ed.* **2012**, *51*,

7550.

4 Conclusion

4.1 Concluding Remarks

The SMM systems exhibit slow magnetization reorientation due to the relatively high energy barrier, Δ.[1] To enhance Δ, ground high-spin polynuclear complexes involving ferromagnetic couplings are supposed to be good candidates for SMM building blocks.[2] Another way to enhance Δ seems to be the use of strong magnetic anisotropy.[3] Heavy-rare-earth metal ion complexes are good candidates for this purpose. In the present thesis, both approaches have been realized by using 3d-homo- and 4f-3d-heterometallic systems. The trinuclear triangular nickel(II) complexes have been characterized to be ground S = 3 species (Chapter 2), and trinuclear bent Cu–Dy–Cu complexes have also been characterized to be high-spin at their ground states (Chapter 3).

The exchange coupling involved in homo- and heterometallic multinuclear complexes is one of the most important parameters to comprehend the magnetic properties. The knowledge of the exchange coupling mechanism would be very helpful to develop new bulk permanent magnets. Therefore the main portion of the present thesis was devoted to the precise and reliable determination of magnetic parameters including exchange couplings. Further, the author set the purposes of this thesis on the following items: (1) To design easily accessible molecules with uniaxial magnetic anisotropy. (2) To find out relationship between the exchange coupling parameter and structural parameters.

The conclusion of (1) is as follows. In the previous study,[4] the nickel(II) trinuclear compounds with an isosceles triangle shape was made. The compound gave rise to the non-uniaxial magnetic anisotropy. On the other hand, the present compounds investigated in this thesis possess an approximately equilateral triangle form. The author has designed and prepared a novel triangular compound $[Ni_3(tmen)_3(\mu_2\text{-}Cl)_3(\mu_3\text{-}OMe)(\mu_3\text{-}OH)](BPh_4)$. The synthesis was so simple and was proceeded in one step. The Ni_3 molecular portion showed an almost ideal

three-fold symmetry (Figures 2.2 and 2.3 in Chapter 2). The intramolecular coupling is ferromagnetic, which is mediated by the superexchange interaction. The exchange parameter J of **1** was precisely determined ($2J/k_B$ = 18.0±0.2 K). The uniaxial magnetic anisotropy was observed in the single-crystal magnetic measurements, and the ZFS parameter D was also derived ($D_{S=3}/k_B$ = −2.2±0.1 K). At low temperatures, the intermolecular antiferromagnetic interaction masked the magnetic behavior of the single-molecule magnet. However, the magnetic character of an independent cluster could be determined in the intermediate temperature because of the separation of the energy ranges among intracluster exchange coupling, ZFS, and intermolecular coupling.

One may wonder if there is any relationship between the molecular structure and magnetic anisotropy. From the comparison among the two $Ni_3Cl_3O_1Y_1^2$ clusters (Scheme 2.1) investigated here, it is noticed that the strong magnetic anisotropy is related to the smaller Ni–O–Ni angles. Namely, $D_{S=3}/k_B$ = −2.2±0.1 K was found in the complex with the Ni–O–Ni angle of 90±2° while $D_{S=3}/k_B$ = −1.6±0.2 K for the complex with 97±1° (compounds **1** and **2**, respectively, in Chapter 2). Proving this hypothesis by further examples would be interesting. The capping oxygen atoms may play an important role both in the superexchange coupling and in the magnetic anisotropy.

The author describes the conclusion of (2). Usually, it is difficult to evaluate the exchange coupling of Dy^{3+} compounds by means of conventional magnetic susceptibility and magnetization measurements. It is because of the strong anisotropy caused by the unquenched orbital moment contribution and of the complicated crystal field splitting. In the present thesis, the HF-EPR technique was utilized. The key point is that the resonance fields of 3d transition metal ions are biased by the exchange field from 4f ions. As described in Chapter 3, two trinuclear isomeric compounds and one polymeric compound were synthesized using a $Dy(OCu)_2$ chromophore. The exchange coupling parameters were found to be in the range of 1.79 – 2.25 K. The present result shows an advantage of doubly oxygen-bridged motifs to build strong ferromagnetic interactions between lanthanide and transition metal ions. In addition, the sizable activation energies for the

magnetization reversal were found at zero magnetic field. It shows that the present systems are SMMs.

Some magneto-structure trends have been found; for example the ferromagnetic exchange coupling is stronger when the Dy–O···O–Cu "butterfly" structure is more bent (Figure 3.13b in Chapter 3). A quantitative understanding would be possible for future progresses in quantum chemistry calculations. The established ways for the precise determination of the exchange parameters would contribute to developments of exchange-coupled 4f-3d heterometallic magnets.

4.2 Future Perspectives

As for the nickel(II) trinuclear compounds, intermolecular antiferromagnetic couplings were observed through the short halogen···halogen distances, and the most unexpected result is that $[Ni_3(tmen)_3(OH)Br_4]Br$ (compound **2**)[5] underwent the antiferromagnetic transition at 3.2 K (Figure 2.4 in Chapter 2). Namely, there are antiferromagnetic "super-superexchanges"[6] through the Ni–X···X–Ni paths (as opposed to the Ni–X–Ni superexchange paths). This mechanism mostly brings about antiferromagnetic interaction, but the intermolecular ferromagnetic coupling would attract much more attention to the materials researchers. Replacing halogen atoms and counter anions may be an option for this purpose. Further, μ_3-bridging groups such as "cap" would be allowed to vary under some conditions such as temperature and pressure. By the variation of "cap", the strength of magnetic anisotropy may be controlled.

The ligand tmen has been used in triangular compounds also with cobalt(II) and iron(II) ions.[5,7] The magnetic properties of the Fe derivative were investigated, and the intramolecular ferromagnetic coupling was found in the magnetic measurements in 90 – 300 K.[7] The magnetic properties of the cobalt derivative (Figure 4.1) have not yet been reported. Since a cobalt(II) ion has orbital angular momentum and magnetic anisotropy, the magnetic properties of the cobalt(II) triangles are of great interest for the development of novel SMMs.

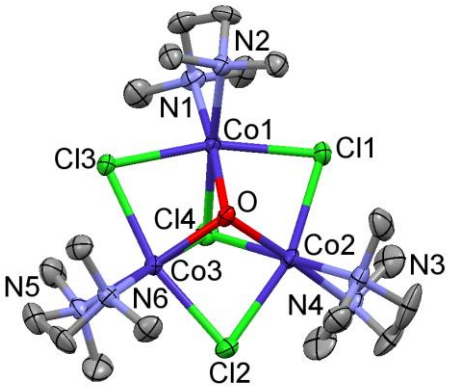

Figure 4.1. ORTEP of the trinuclear molecule of $[Co_3Cl_4(OH)(tmen)_3](BPh_4)\cdot 0.5[CoCl_2\text{-}(tmen)_2]$.[5]

For the magneto-structure relation in the Dy–O···O–Cu "butterfly" compounds, bent configuration seems to favor ferromagnetic interaction. There are ample examples of Dy–Cu heterometallic complexes having "cubane", "semicubane", and "fused cubane" skeletons. Actually ferromagnetic interactions have been reported in the Co_2Dy_2 and Ni_2Fe_2 compounds having a "defective dicubane" motif.[8] The Co–O–Dy and Ni–O–Dy bond angles range in (97.2±0.1) – (107.0±0.1) and (96.6±0.1) – (106.9±0.1)°, respectively.[8] The wide variation of geometries as well as variation of 3d ions and 4f ions will be a subject to future studies.

The present work gives the first detailed investigation of magneto-structure relations based on the precise determination of exchange coupling in Ln–Cu compounds, where Ln is other than Gd. Although the number of reported examples is very small, the author carried out preliminary analysis of the relation on the $TbCu_2$ compounds.[9] Watanabe and co-workers reported $J_{Tb\text{-}Cu}$ in $[Cu^{II}(L^A)(C_3H_6O)Tb^{III}(NO_3)_3]$,[9a] and Shimada and co-workers in $[Tb^{III}L^B{}_2(NO_3)_2\{Cu^{II}(CH_3OH)\}_2](NO_3)(CH_3OH)$[9b] with the analogous DyO_2Cu structures (for the abbreviation of L^A and L^B, see Chapter 3). The exchange coupling parameter $J_{Tb\text{-}Cu}$ is plotted against the "butterfly" angle (Figure 3.15 in Chapter 3). A similar trend can be seen; the bent "butterfly" structure favors strong ferromagnetic coupling. Figure 4.2 shows a preliminary 3D

plot combined with Figure 3.13b and 3.15 in Chapter 3. By collecting more samples, the 3D plot would reveal a more detailed magneto-structure relationship as well as a periodicity of the lanthanoid elements.

The method for the estimation of exchange coupling by means of HF-EPR is unique approach developed by the group to which the author belongs. The above examples indicate the generality of this method and will be applied to a wide variety of Ln–Cu heteronuclear systems. Establishing the relationship of the exchange couplings and structures will afford an important guide to improve performance of SMMs as well as other types of 4f-3d based magnets.

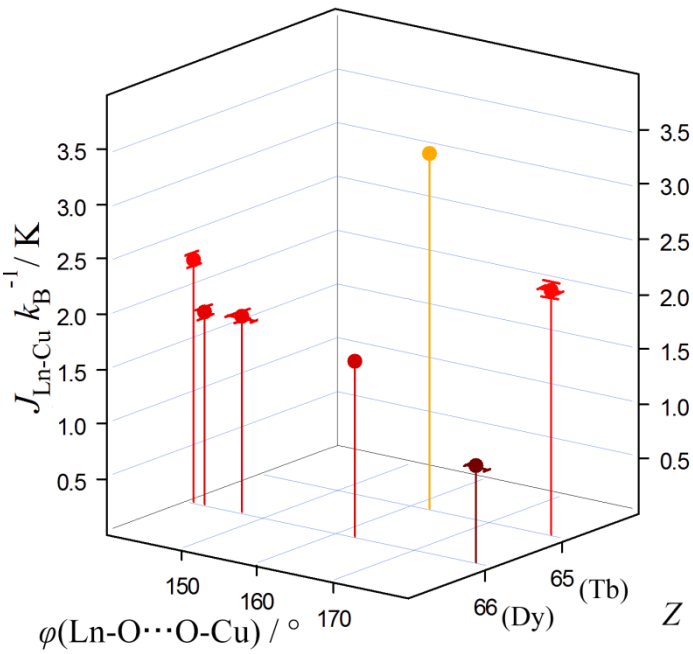

Figure 4.2. 3D plot of a possible relationship of the exchange coupling as a function of the "butterfly" angle and the atomic numbers.

References

(1) (a) D. Gatteschi, R. Sessoli, J. Villain, *Molecular Nanomagnets*, Oxford University Press, New York, **2006**; (b) D. Gatteschi, R. Sessoli, *Angew. Chem.*, *Int. Ed.* **2003**, *42*, 268; (c) *Single-Molecule Magnets and Related Phenomena*, ed. by R. Winpenny, Springer-Verlag Berlin, **2006**; (d) L. Bogani, W. Wersdorfer, *Nature Mat.* **2008**, *7*, 179.

(2) (a) P. D. W. Boyd, Q. Li, J. B. Vincent, K. Folting, H.-R. Chang, W. E. Streib, J. C. Huffman, G. Christou, D. N. Hendrickson, *J. Am. Chem. Soc.* **1988**, *110*, 8537; (b) A. Caneschi, D. Gatteschi, R. Sessoli, *J. Am. Chem. Soc.* **1991**, *113*, 5873; (c) R. Sessoli, H.-L. Tsai, A. R. Schake, S. Wang, J. B. Vincent, K. Folting, D. Gatteschi, G. Christou, D. N. Hendrickson, *J. Am. Chem. Soc*. **1993**, *115*, 1804; (d) A. L. Barra, A. Caneschi, A. Cornia, F. Fabrizi de Biani, D. Gatteschi, S. Sangregorio, R. Sessoli, L. Sorace, *J. Am. Chem. Soc.* **1999**, *121*, 5302; (e) S. L. Castro, Z. Sun, C. M. Grant, J. C. Bollinger, D. N. Hendrickson, G. Christou, *J. Am. Chem. Soc.* **1998**, *120*, 2365; (f) A. J. Tasiopoulos, A. Vinslava, W. Wernsdorfer, K. A. Abboud, G. Christou, *Angew. Chem.*, *Int. Ed.* **2004**, *43*, 2117; (g) M. Murugesu, M. Habrych, W. Wernsdorfer, K. A. Abboud, G. Christou, *J. Am. Chem. Soc.* **2004**, *126*, 4766.

(3) (a) N. Ishikawa, M. Sugita, T. Ishikawa, S.-y. Koshihara, Y. Kaizu, *J. Am. Chem. Soc.* **2003**, *125*, 8694; (b) J. D. Reinhart, J. R. Long, *Chem. Sci.* **2011**, *2*, 2078; (c) D. N. Woodruff, W. R. E. P. Winpenny, R. A. Layfield, *Chem. Rev.* **2013**, *113*, 5110; (d) R. Sessoli, A. K. Powell, *Coord. Chem. Rev.* **2009**, *253*, 2328; (e) M. Andruh, J. P. Costes, C. Diaz, S. Gao, *Inorg. Chem.* **2009**, *48*, 3342; (f) P. H. Lin, T. J. Burchell, L. Ungur, L. F. Chibotaru, W. Wernsdorfer, M. Murugesu, *Angew. Chem.*, *Int. Ed.* **2009**, *48*, 9489; (g) J. D. Rinehart, M. Fang, W. J. Evans, J. R. Long, *Nature Chem.* **2011**, *3*, 538; (h) H. L. C. Feltham, S. Brooker, *Coord. Chem. Rev.* **2014**, *276*, 1; (i) P. Zhang, L. Zhang, C. Wang, S. F. Xue, S. Y. Lin, J. K. Tang, *J. Am. Chem. Soc.* **2014**, *136*, 4484; (j) S. Yamauchi, T. Fujinami, N. Matsumoto, N. Mochida, T. Ishida, Y. Sunatsuki, M. Watanabe, M. Tsuchimoto, C. Coletti, N. Re, *Inorg.*

Chem. **2014**, *53*, 5961.

(4) R. Biswas, Y. Ida, M. L. Baker, S. Biswas, P. Kar, H. Nojiri, T. Ishida, A. Ghosh, *Chem. Eur. J.* **2013**, *19*, 3943.

(5) D. A. Handley, P. B. Hitchcock, G. J. Leigh, *Inorg. Chim. Acta* **2001**, *314*, 1.

(6) (a) M.-H. Whangbo, H.-J. Koo, D. Dai, *J. Solid State Chem.* **2003**, *176*, 417; (b) M.-H. Whangbo, H.-J. Koo, D. Dai, D. Jung, *Inorg. Chem.* **2003**, *42*, 3898; (c) R. D. Willett, B. Twamley, W. Montfrooij, G. E. Granroth, S. E. Nagler, D. W. Hall, J.-H. Park, B. C. Watson, M. W. Meisel, D. R. Talham, *Inorg. Chem.* **2006**, 45, 7689; (d) J. L. Manson, M. M. Conner, J. A. Schlueter, A. C. McConnell, H. I. Southerland, I. Malfant, T. Lancaster, S. J. Blundell, M. L. Brooks, F. L. Pratt, J. Singleton, R. D. McDonald, C. Lee, M.-H. Whangbo, *Chem. Mater.* **2008**, *20,* 7408; (e) J. A. Schlueter, H. Park, G. J. Halder, W. R. Armand, C. Dunmars, K. W. Chapman, J. L. Manson, J. Singleton, R. McDonald, A. Plonczak, J. Kang, C. Lee, M.-H. Whangbo, T. Lancaster, A. J. Steele, I. Franke, J. D. Wright, S. J. Blundell, F. L. Pratt, J. deGeorge, M. M. Turnbull, C. P. Landee, *Inorg. Chem.* **2012**, *51*, 2121.

(7) S. C. Davies, D. L.Hughes, G. J. Leigh, J. R. Sanders, J. S. de Souza, *J. Chem. Soc., Dalton Trans.* **1997**, 1981.

(8) (a) K. C. Mondal, G. E. Kostakis, Y. Lan, W. Wernsdorfer, C. E. Anson, A. K. Powell, *Inorg. Chem.* **2011**, *50*, 11604; (b) K. C. Mondal, A. Sundt, Y. Lan, G. E. Kostakis, O. Waldmann, L. Ungur, L. F. Chibotaru, C. E. Anson, A. K. Powell, *Angew. Chem.*, *Int. Ed.* **2012**, *51*, 7550.

(9) (a) T. Ishida, R. Watanabe, K. Fujiwara, A. Okazawa, N. Kojima, G. Tanaka, S. Yoshii, H. Nojiri, *Dalton Trans.* **2012**, *41*, 13609; (b) T. Shimada, A. Okazawa, N. Kojima, S. Yoshii, H. Nojiri, T. Ishida, *Inorg. Chem.* **2011**, *50*, 10555.

Acknowledgements

I am deeply grateful to Prof. Takayuki Ishida as my supervisor who gave me considerable encouragements and tremendous supports of inestimable value for my study. I thank Prof. Hiroyuki Nojiri, IMR, Tohoku Univ. for kind assistance in the measurements of HF-EPR and pulsed-field magnetization. He gave me constructive comments and sincere encouragements. I would also like to express my gratitude to Mr. Soumavo Ghosh and Prof. Ashutosh Ghosh, Univ. of Calcutta, India, who afforded me the three $DyCu_2$ compounds. Special thanks are also expressed to Prof. Keiko Miyamoto, Ochanomizu Univ. Tokyo, who thought me detailed information of the preparation procedure and provided me the nickel(II) trinuclear compounds.

Publication List

Contents of this thesis have been published in:

Chapter 2

(1) Yumi Ida, Hiroyuki Nojiri, and Takayuki Ishida
"Trigonal Bipyramid $Ni_3Cl_3O_2$ Cluster Showing the High-Spin S = 3 Ground State with Uniaxial Magnetic Anisotropy"
Bulletin of the Chemical Society of Japan, **Vol. 89**, pp. 226–236 (2016). BCSJ Award

Chapter 3

(2) Yumi Ida, Soumavo Ghosh, Ashutosh Ghosh, Hiroyuki Nojiri, and Takayuki Ishida
"Strong Ferromagnetic Exchange Interactions in Hinge-like $Dy(O_2Cu)_2$ Complexes Involving Double Oxygen Bridges"
Inorganic Chemistry, **Vol. 54**, pp. 9543–9555 (2015).

Other publication of the author:

(1) Paramita Kar, Rituparna Biswas, Michael G B Drew, Yumi Ida, Tkayuki Ishida, and Ashutosh Ghosh
"Structure and Magnetic Properties of an Unprecedented *syn-anti* μ-Nitrito-1κ*O*:2κ*O′* Bridged Mn(III)-Salen Complex and Its Isoelectronic and Isostructural Formate Analogue"
Dalton Transactions, **Vol. 40**, pp. 3295–3304 (2011).

(2) Paramita Kar, Rituparna Biswas, Yumi Ida, Tkayuki Ishida, and Ashutosh Ghosh
"A Unique Example of Structural Diversity Tuned by Apparently Innocent *o*-, *m*- and *p*-Nitro Substituents of Benzoate in Their Complexes of Mn(II) with 4,4'-Bipyridine: 1D Ladder, 2D Sheet and 3D Framework"
Crystal Growth and Design, **Vol. 11**, pp. 5305–5315 (2011).

(3) Paramita Kar, Yumi Ida, Tkayuki Ishida, and Ashutosh Ghosh
"Formation of Two Drastically Different MOFs Based on Mn(II)-Benzoate and Pyrazine with a Change in Seasonal Temperature: Structural Analysis and Magnetic Study"
CrystEngComm, **Vol. 15**, pp. 400–410 (2013).

(4) Rituparna Biswas, Yumi Ida, M. L. Baker, Saptarshi Biswas, Paramita Kar, Hiroyuki Nojiri,

Takayuki Ishida, and Ashutosh Ghosh
"A New Family of Trinuclear Nickel(II) Complexes as Single-Molecule Magnets"
Chemistry – A European Journal, **Vol. 19**, pp. 3943–3953 (2013).

(5) Soumavo Ghosh, Yumi Ida, Takayuki Ishida, and Ashutosh Ghosh
"Linker Stoichiometry-Controlled Stepwise Supramolecular Growth of a Flexible Cu_2Tb Single Molecule Magnet from Monomer to Dimer to 1D Chain"
Crystal Growth and Design, **Vol. 14**, pp. 2588–2598 (2014).

(6) Paramita Kar, Yumi Ida, Takuya Kanetomo, Michael G. B. Drew, Takayuki Ishida and Ashutosh Ghosh
"Synthesis of Mixed-Valence Hexanuclear Mn(II/III) Clusters from Its Mn(II) Precursor: Variations of Catecholase-like Activity and Magnetic Coupling"
Dalton Transactions, **Vol. 44**, pp. 9795–9804 (2015).